HOW DOES TERRAIN INFLUENCE THE UPSCALE CONVECTIVE GROWTH OF OROGRAPHIC DEEP MOIST CONVECTION?

BY

JAKE PATRICK MULHOLLAND

DISSERTATION

Submitted in partial fulfillment of the requirements
for the degree of Doctor of Philosophy in Atmospheric Sciences
in the Graduate College of the
University of Illinois at Urbana-Champaign, 2019

Urbana, Illinois

Doctoral Committee:

Professor Stephen W. Nesbitt, Chair
Professor Robert J. Trapp, Co-Chair
Professor Robert M. Rauber
Assistant Professor Deanna A. Hence

ABSTRACT

Satellite observations have revealed that some of the world's most intense deep convective storms occur near the Sierras de Córdoba, Argentina, South America. A ground-based radar climatology during two austral spring and summer seasons (2015–2017) revealed that most of the storms were multicellular and initiated most frequently during the early afternoon and late evening hours just east of the Sierras de Córdoba. The peak occurrence of these storms was between December-February. Storm environments in Argentina tend to be characterized by larger convective available potential energy and weaker low-level vertical wind shear compared to the United States. One of the more intriguing results is the relatively fast transition, and close proximity to terrain, from first storms to larger mesoscale convective systems compared with locations in the United States.

A canonical upscale convective growth case was simulated with the Weather Research and Forecasting model to understand the role of topography in this transition process. This case featured an orographic supercell that transitioned into a bowing mesoscale convective system over three-to-four hours. The simulation revealed enhanced low-level vertical wind shear along the eastern slopes of the Sierras de Córdoba that aided in the formation of a left moving supercell. Shortly thereafter, strong downdrafts and expansion of the cold pool resulted in a rapid transition to a bowing mesoscale convective system. Terrain height sensitivity experiments were conducted with only the control and higher terrain experiments resulting in a supercell-to-bowing mesoscale convective system transition. The control simulation, with the real terrain of the Sierras de Córdoba, resulted in the faster upscale convective growth owing to both terrain-driven environmental and storm-scale effects, such as variations to thermodynamic/kinematic profiles and terrain blocking of cold pools, respectively.

Inspired by the aforementioned ground-based radar climatology and in-depth numerical modeling upscale convective growth case study in north central Argentina, a set of different initial terrain height idealized numerical modeling experiments were conducted. These experiments were devised to determine the relative roles of both direct and indirect influences of terrain on upscale convective growth of a supercell in a model configuration similar to those observed near the Sierras de Córdoba in Argentina. The experimental results indicated that when the terrain was systematically raised, convection initiation occurred earlier, supercells were wider and more intense, and upscale convective growth generally occurred faster. A direct influence of terrain was blocking of cold pools leading to a deepening of the cold pools that drove surging outflow and more rapid upscale convective growth. Indirect influences of terrain included modifications to the surrounding thermodynamic and kinematic profiles, with terrain-enhancements to the vertical wind shear profile prompting wider updrafts in higher terrain supercells. These wider supercell updrafts were accompanied by greater vertical mass flux, wider and stronger downdrafts, and deeper cold pools, promoting more rapid upscale convective growth.

ACKNOWLEDGEMENTS

The author would like to thank Drs. Robert Trapp, Stephen Nesbitt, Jeffrey Frame, Robert Rauber, and Deanna Hence (University of Illinois at Urbana-Champaign; UIUC), Dr. John M. Peters (Naval Postgraduate School), Dr. Christopher J. Nowotarski (Texas A&M University; TAMU), Dr. Scott M. Steiger (State University of New York at Oswego), Dr. Hugh Morrison, Jim Wilson, and Rita Roberts (National Center for Atmospheric Research), Dr. Michael Coniglio (National Severe Storms Laboratory), Dr. Bruno Ribeiro (Centro de Previsão do Tempo e Estudos Climáticos), and Drs. Kristen L. Rasmussen and Susan van den Heever (Colorado State University) for thought-provoking and fruitful discussions, Tom Gowan (University of Utah) for use of his Python trajectory code (https://github.com/tomgowan/trajectories), and Dr. Brian Jewett, Chuan-Chieh Chang, Geoff Marion, Benjamin Vega-Westhoff, Tzu-shun Lin, Itinderjot Singh, Kevin Gray, Jun Zhang, Randy Chase, Sujan Pal, and Andrew Huang (UIUC) for computing assistance. Many thanks go to Dr. Bowen Pan (TAMU) and Janice Mulholland (my mom) for their extremely useful comments improving this dissertation. Special thanks go to the dedicated and hardworking UIUC Department of Atmospheric Sciences IT staff (David Wojtowicz and Kenneth Patten) and our wonderful secretaries (Tammy Warf and Joe Jeffries). A final thanks to all the anonymous reviewers who helped improve the entirety of the work herein. Computational resources were provided by the Computational and Information Systems Lab at the National Center for Atmospheric Research and UIUC's Keeling supercomputing cluster. Support for this research was made possible by National Science Foundation Grant AGS-1661799.

DEDICATION

This dissertation is dedicated to my loving family (Jan—"mommy", Frank—"daddy", Dillon—"elephant" and "D-brahhh", Buster, and Max), my beautiful and loving girlfriend, Bowen—"my queen, my buoyancy, my missing puzzle piece, and my only exception", my brother's family (Erikka and Calliope—"Callie"), all my Aunts (Roberta, Joleen), Uncles (Dan, Dave), etc., my best friends—Richard Sprancmanis—"JR", Michael Vuotto—"Mikey V", Chuan-Chieh Chang—"brahhh", Tzu-Chun Lin, Benjamin Vega-Westhoff, and Andrew Janiszeski, my "study buddies", Deanna Apps—"buddy" and Johana Lambert, my mentors—Drs. Scott Steiger, Robert Ballentine, Steven Skubis, Alfred Stamm, Jeffrey Frame, Robert Trapp, Stephen Nesbitt, Robert Rauber, John Peters, Hugh Morrison, all of my teachers and professors (too many to mention!), my past Tim Hortons bosses (and now friends) Steve and Sandra Hughes, and all of my life-long friends (also, too many to mention!), A loving thank you to the souls who live on even though they are not with us physically: Shadow, Bandit, Willy, Dr. Alfred Stamm. Thank you, God, for giving me this opportunity to pursue my passion for learning about Mother Nature, a dream of mine since I was six years old. Finally, I want to specifically thank my mom, aka—"my biggest fan", for instilling within me the passion for learning and for realizing that I can pursue anything that I put my mind to. If it weren't for your help on that first big project back in Mr. Macko's 6th grade science class on Wolves, and your willingness to help me break it down bit-by-bit, I would not be where I am at today. You taught me the proper ways to learn, something that resonates within me to this day...

"Remember, George: no man is a failure who has friends."

"Oh, the Places You'll Go!"

TABLE OF CONTENTS

CHAPTER 1: INTRODUCTION

1.1 Chapter 3: Introduction and Motivation

Satellite observations have revealed that some of the world's most intense thunderstorms occur across subtropical South America, and more specifically northern and central Argentina (Fig. 1.1; e.g., Zipser et al. 2006; Romatschke and Houze 2010; Cecil and Blankenship 2012; Houze et al. 2015). These thunderstorms typically develop near a secondary mountain range to the east of the Andes, called the Sierras de Córdoba (SDC), and have been associated with severe weather hazards in the form of damaging straight-line wind gusts, large hail, flash flooding, and tornadoes (derived from local media and newspaper reports; Rasmussen and Houze 2011; Rasmussen et al. 2014). The production of severe weather has been shown to be strongly dependent upon the mode of convection (discrete vs. multicellular; e.g., Dial et al. 2010), which is largely a factor of the vertical wind shear profile (e.g., Trapp 2013). Previous studies in the United States (USA), such as Smith et al. (2012), have revealed that most tornado and large hail reports originate from supercellular convection, whereas damaging straight-line wind gusts predominantly occur with larger mesoscale convective systems (MCSs; Zipser 1977). Similar studies have been largely absent across Argentina, however, as high spatiotemporal radar, surface, and upper-air observations are sparse and a standard severe weather reporting procedure has not yet been implemented operationally at the time of this writing. The aim of the first part of this dissertation is to utilize data from a recently installed ground-based radar to characterize common convective life cycles near the SDC and establish a baseline climatology of environments supportive of this robust deep moist convection (DMC).

From an ingredients-based approach developed over the central USA (e.g., Johns and Doswell 1992; Doswell et al. 1996; Johnson and Mapes 2001), studies have linked severe

thunderstorms to abundant lower-tropospheric moisture, steep mid-tropospheric lapse rates, and strong tropospheric vertical wind shear (hereafter: wind shear). The specific presence of tornadoes is particularly related to strong wind shear over the lowest 1 km of the atmosphere, and to lifting condensation levels (LCLs) below 1 km above ground level (AGL; e.g., Markowski et al. 2002; Thompson et al. 2003; Smith et al. 2012; Markowski and Richardson 2014). In subtropical South America, Brooks et al. (2003) and Rasmussen and Houze (2016) have shown that these ingredients are commonly present owing to the influence of midlatitude weather systems crossing the Andes Mountains, steep lapse rate midlevel air (elevated mixed layers; EMLs; Ribeiro and Bosart 2018), and abundant low-level moisture streaming poleward from the Amazon rainforest region in the South American Low-Level Jet (SALLJ; Vera et al. 2006) (Fig. 1.2). Convection initiation (CI) typically occurs over the SDC owing to enhanced low-level moisture convergence and anabatic upslope flows.

Previous studies of DMC across South America have predominantly used satellite data to elucidate details regarding storm structure and evolution (e.g., Nesbitt et al. 2006; Zipser et al. 2006; Rasmussen and Houze 2011; among others). Owing to the limitations of satellite data, specifically related to characterizing certain convective modes (e.g., supercells), along with the temporal evolution of the convection, this and other studies have been unable to understand the full convective mode spectrum and life cycle evolution in areas such as Argentina. Many of these limitations are mitigated with the installation of C-band, dual-polarization Doppler weather radars across Argentina to document convective-storm frequency, structure, and evolution in this region over multiple seasons. Until the present study, there have not been any systematic studies to examine convective modes, their life cycle, and their relationship to the ambient storm environments in this region, which motivates the work herein. As in prior studies, we identify

common convective modes using newly available radar data from the C-band Córdoba radar (RMA1) during the austral spring and summers of 2015–2017. A subjective storm classification scheme is used to identify prominent convective modes, including storm upscale convective growth into larger MCSs. To quantify differences between the radar and satellite perspectives provided by the aforementioned prior works, life cycle statistics are compared to longer-term storm life cycle analyses using Tropical Rainfall Measuring Mission (TRMM) Precipitation Radar (PR) data from September 1998–February 2014 over a similar domain. Finally, ERA-Interim reanalysis composites are constructed for the RMA1-identified convective modes to further understand environments supportive of the observed convection.

1.2 Chapters 4 and 5: Introduction and Motivation

Upscale convective growth (UCG), the transition from isolated DMC into MCSs, is an important atmospheric process to understand owing to the severe weather hazards that are associated with different convective modes. Isolated convective modes, such as supercells, are more apt to produce large hail and tornadoes whereas MCSs are more apt to result in a damaging wind and flooding threat (e.g., Johns and Doswell 1992; Trapp et al. 2005; Dial et al. 2010; Smith et al. 2012). In particular, this transition time may be especially dangerous due to overlapping severe weather hazards (e.g., Nielsen et al. 2015). Recommended safety protocol for tornadoes (seeking lower ground) versus flooding (seeking higher ground) is drastically different and portraying the risks of these overlapping severe weather hazards to the public is an ongoing challenge for forecasters, especially since numerical models typically struggle to capture this transition (e.g., Done et al. 2004; Hawblitzel et al. 2007; Weisman et al. 2013; Schumacher et al. 2013). Furthermore, MCSs are known for their ability to produce copious amounts of rainfall (e.g., Laing and Fritsch 1997). The latent heat that is released owing to condensation and freezing may

impact mesoscale-to-synoptic scale weather patterns on spatiotemporal scales larger/longer than the individual MCS itself (e.g., Keyser and Johnson 1984).

There are many pathways of UCG, including, but not limited to: (1) the interaction of multiple convective cold pools (e.g., Bluestein and Weisman 2000; Coniglio et al. 2010; Fu and Guo 2012), (2) the transition from a single, dominant storm, such as a supercell, into an MCS (e.g., Moller et al. 1990; Finley et al. 2001; Klimowski et al. 2004), or (3) the growth of DMC into an MCS along a low-level baroclinic and/or moisture gradient (e.g., Dial et al. 2010; Coniglio et al. 2010). The focus of the work herein is on the supercell-to-MCS transition owing to the propensity for this particular UCG pathway to be most associated with the aforementioned overlapping severe weather hazards (Fig. 1.3; e.g., Nielsen et al. 2015). The transition from a supercell to an MCS is signified as a change in the dominant forcing mechanism for new/continued updraft formation (Fig. 1.4). In supercells, new/continued updraft formation predominately occurs via lifting owing to vertical perturbation pressure gradient forces stemming from vertically-oriented rotation, inducing (sometime vigorous) low-level ascent (Fig. 1.4a). In MCSs, however, the predominant formation of new/continued updraft growth owes to mechanical lifting along a cold pool's leading edge (colloquially known as "gust fronts" or "outflow boundaries") (Fig. 1.4b). The supercell-to-MCS transition typically occurs when a supercell's cold pool becomes deep and strong enough to outpace and undercut the mesocyclone, resulting in the aforementioned dynamical change of DMC low-level lifting (e.g., Finley et al. 2001).

Studies of UCG have been relatively sparse and mostly conducted across the central USA. A recent study from Argentina, South America, used ground-based radar data to build a two-year convective storm mode and morphology climatology (Mulholland et al. 2018; also see Chapter 3). The climatology revealed that UCG tended to occur closer to the high terrain (of the SDC in

Argentina) and faster than in the USA (e.g., Coniglio et al. 2010). Neither of these studies addressed the specific reasons for the spatiotemporal distributions of UCG events in relation to terrain. Outside of a few limited studies that analyzed the growth of MCSs near terrain (e.g., Tripoli and Cotton 1989a,b; Rasmussen and Houze 2014), relatively little research on how topography influences UCG has been conducted.

Terrain can have both direct and indirect influences on UCG. An example of a direct influence is one in which convective cold pools located near terrain are effectively blocked along mountain slopes, causing an accumulation or deepening of negatively-buoyant air (e.g., Xu et al. 2012; Phadtare 2018; Mulholland et al. 2019), potentially affecting cold pool characteristics such as depth, shape, and propagation speed (Fig. 1.5). A resultant near-surface nonhydrostatic high pressure perturbation would foster a radially-outward-pointing horizontal pressure gradient force. Surging outflow along and away from the terrain might then result, which would serve as the impetus for secondary CI along the outflow boundary, ultimately leading to faster UCG as compared to flatter surfaces. An in-depth analysis of this potential process near terrain has yet to be conducted.

Indirect influences of terrain include modifications to the mesoscale and synoptic-scale environment due to flow blocking and channeling, resulting in changes to wind shear and convective available potential energy (CAPE), which may then impact UCG. A detailed case study of an UCG event in Argentina using the Weather Research and Forecasting (WRF) model showed that when the terrain of the SDC was systematically raised (lowered), the wind shear increased (decreased) and CAPE decreased (increased), which ultimately lead to a faster (slower) UCG rate (Mulholland et al. 2019; also see Chapter 4). Owing to the real-data modeling framework implemented, this particular study was unable to cleanly separate the relative roles of direct versus

indirect influences of terrain on UCG. This motivates the use herein of an idealized modeling framework, which more readily allows for such a separation (see Chapter 5).

One possible indirect influence of terrain is alterations to the wind shear profile. Wind shear has long been demonstrated to influence the organization of DMC, including supercells and MCSs (e.g., Weisman and Klemp 1982). Low-level wind shear (e.g., 0–3 km) has oft been cited as an important factor for the organization and longevity of MCSs (e.g., Rotunno et al. 1988). Other authors have also stressed the importance of upper-level wind shear (e.g., 3–10 km) in the maintenance of MCSs (e.g., Coniglio et al. 2006). Relatively little attention, however, has been focused on the wind shear characteristics that promote the transition between isolated convective modes and MCSs, especially near terrain. Coniglio et al. (2010) showed that rapidly developing MCSs typically form in environments with stronger (weaker) low-level (upper-level) wind shear as compared with slowly developing MCSs. The authors speculated that the weaker deep-layer wind shear prompted less favorable conditions for supercells whereas the increased low-level wind shear was favorable for both enhanced gust front lifting and warm air advection. These potential physical explanations, however, were never explored in detail. Furthermore, it is unclear whether these wind shear characteristics were a consequence of, rather than a causal factor in the development of MCSs as studies have shown significant MCS-induced modifications on the near-storm environment (e.g., Fritsch and Maddox 1981; Keyser and Johnson 1984; Perkey and Maddox 1985; Wolf and Johnson 1995a,b; Stensrud 1996; Stechman et al. 2016).

Some influences of deep-layer shear on DMC may, on the other hand, increase the likelihood of UCG. Trapp et al. (2017), Warren et al. (2017), Dennis and Kumjian (2017), Marion and Trapp (2019), and Peters et al. (2019b) universally showed that supercell updrafts in environments with increasing magnitudes of deep-layer shear were increasingly wider and

produced more precipitation than storms in environments with weaker deep-layer shear. Marion and Trapp (2019) specifically found a linkage between wider supercell updrafts, wider downdrafts, and thus, deeper cold pools in environments with stronger wind shear. Their results showed that wider supercell updrafts resulted in a larger horizontal area over which precipitation formed within the rising air current. The greater horizontal area over which precipitation formed within the wider updrafts was physically linked to wider downdrafts that developed owing to hydrometeor loading and microphysical diabatic cooling. Furthermore, the magnitude of downdraft mass flux was well correlated with the depth of cold pools via a mass continuity argument. These dependencies suggest that increasing magnitudes of deep-layer shear may actually enhance cold pool production and increase the probability of UCG of supercells, which contradicts the results of Coniglio et al. (2010). This may be due to the fact that the Coniglio et al. (2010) climatology considered any pathway of UCG (not just supercell-to-MCS transitions), whereas the aforementioned studies focused on a single dominant supercell. Furthermore, hydrometeor advection, and subsequent latent cooling regions that drive convective and mesoscale downdrafts and resultant cold pools, likely vary with changes in the wind shear profile (e.g., Peters et al. 2017).

Another possible indirect influence of terrain is alterations to the thermodynamic profile, which include variations in CAPE/convective inhibition (CIN) (e.g., Parker 2002). In general, larger magnitudes of CAPE result in stronger updraft accelerations, all else being equal. Previous authors have shown that larger CAPE and thicker mixed-layer depths resulted in wider, more intense updrafts and downdrafts (e.g., Kirkpatrick et al. 2009; Marion and Trapp 2019). Wider updrafts are more resilient to entrainment-driven dilution, which allows them to retain more of their cloud-core buoyancy, further enhancing vertical accelerations (e.g., Peters et al. 2019b). The connection between updrafts, downdrafts, and by virtue, cold pools, are a continuum that is

ultimately linked to the UCG process. Furthermore, tropospheric perturbations in moisture variables owing to terrain, such as relative humidity (RH) fluctuations, may affect entrainment rates, evaporation/sublimation efficiency, and CIN magnitudes, which then may affect storm morphology (e.g., Markowski and Dotzek 2011).

Studies specifically addressing both direct and indirect influences of terrain on the UCG process are lacking. Most studies have either analyzed CI processes over heated terrain (e.g., Kirshbaum and Wang 2014; Soderholm et al. 2014; and references therein) or how mature supercells (e.g., Markowski and Dotzek 2011) or MCSs (e.g., Frame and Markowski 2006) are affected by crossing over terrain. An idealized modeling study of mature right moving supercells moving over 2- and 3-D terrain by Markowski and Dotzek (2011) found that changes in the environment (wind shear, CAPE) owing to terrain exerted a greater influence on storm morphology than internal storm changes (cold pools). More specifically, they cite that alterations in RH and CIN owing to terrain had the largest effect on storm morphology. Alternatively, another idealized modeling study by Soderholm et al. (2014) found that environmental wind profile changes due to terrain exhibited more influence on convective morphology than environmental thermodynamic changes due to terrain. These results suggest that terrain modifications to the environment (indirect influence) have more influence on storm morphology than internal storm process changes owing to terrain (direct influence). These particular studies, however, either addressed CI and early convective growth or mature supercells/MCSs that crossed terrain features and not the full spectrum of CI–supercell formation–UCG over and downwind of terrain. This dissertation specifically addresses this gap in our understanding of the roles that terrain plays in the UCG of orographic DMC, specifically orographic supercell-to-MCS transitions near the

unique terrain of the SDC. Below are the main science questions adapted from Mulholland et al. (2019) that are addressed in this dissertation:

(1) Does DMC initiated over terrain grow upscale faster or more readily than DMC initiated over flatter, more homogenous surfaces?

(2) What are the relative roles of direct (e.g., terrain blocking of cold pools) and indirect (e.g., terrain-induced variations in wind shear/CAPE) effects on UCG?

(3) Is there an "optimal" terrain height that leads to the most rapid UCG by virtue of altering effectiveness of terrain blocking and/or relevant environmental parameters (e.g., depth of sheared layer, mixed-layer depth)?

1.3 Figures

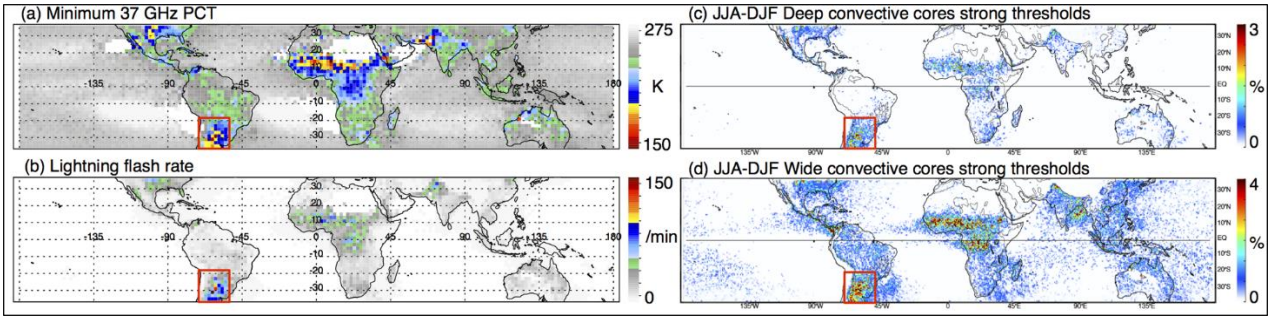

Figure 1.1: TRMM satellite retrievals of: (a) minimum 37 GHz PCT (K), (b) lightning flash rate (min^{-1}), (c) June-July-August (JJA)—Boreal summer or December-January-February (DJF)—Austral summer deep convective cores (see text for details) strong thresholds (%), and (d) JJA—Boreal summer or DJF—Austral summer wide convective cores (see text for details) strong thresholds (%). Panels (a) and (b) are adapted from Zipser et al. (2006) and panels (c) and (d) are adapted from Houze et al. (2015). The red box in all panels across north central Argentina, South America, represents the focus region for the results presented in this dissertation.

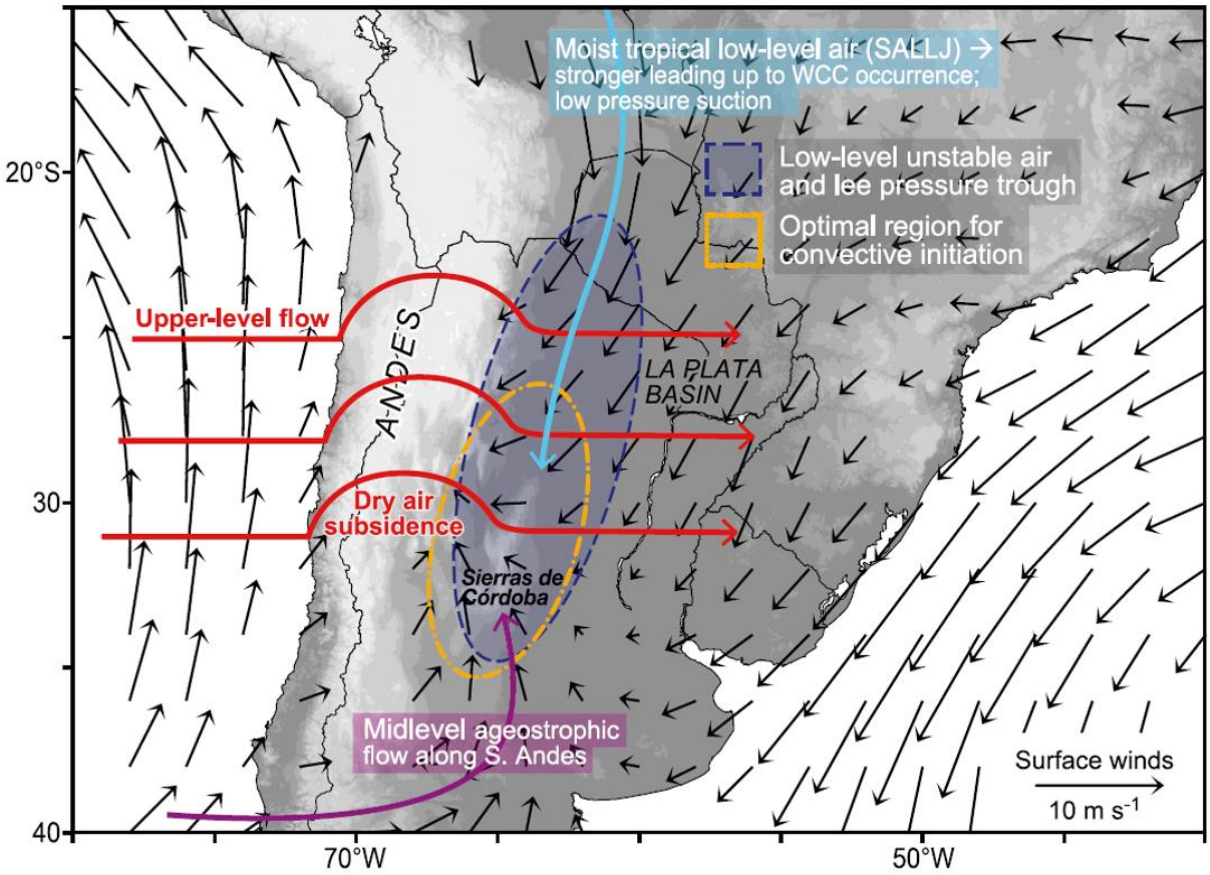

Figure 1.2: Conceptual diagram of the ingredients for deep moist convection initiation in subtropical South America. Black arrows represent near-surface (10 m) winds (m s^{-1}), the light blue arrow represents the South American low-level jet (SALLJ), the purple arrow represents the midlevel ageostrophic flow, the red arrows represent the upper-level flow with subsidence in the lee of the Andes Mountains, the blue dashed oval represents the lee pressure trough region where convective available potential energy resides, and the orange dot-dashed oval is the region most favorable for frequent deep moist convection initiation. Figure adapted from Rasmussen and Houze (2016).

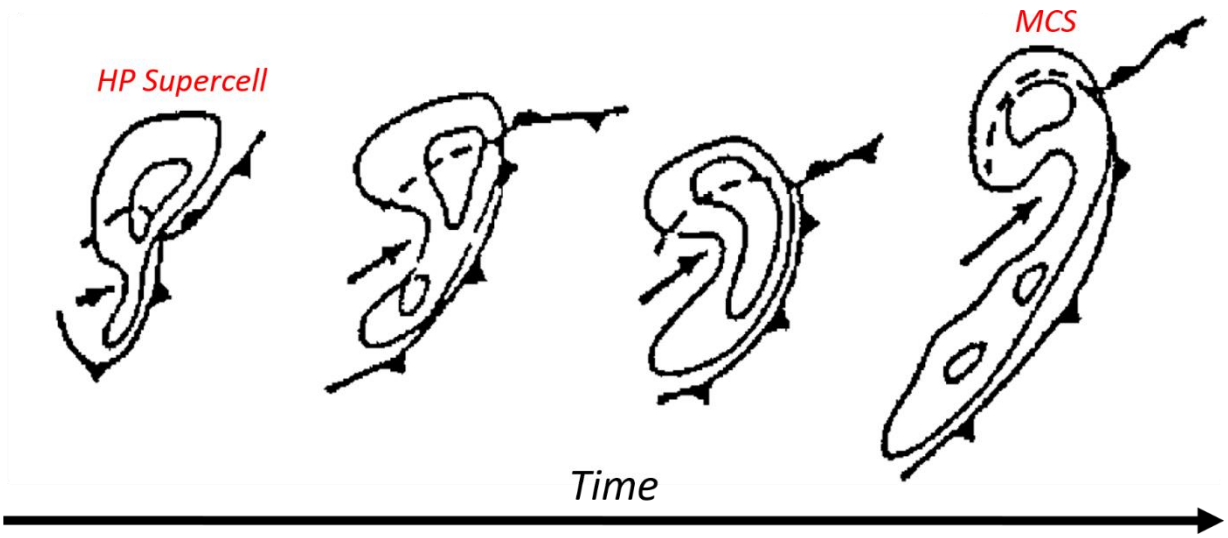

Figure 1.3: Conceptual diagram of a high precipitation (HP) supercell-to-Mesoscale convective system (MCS) transition. Thick black lines represent near-surface reflectivity and approximate near-surface gust front locations are indicated with standard notation. Adapted from Finley et al. (2001) and originally from Moller et al. (1990).

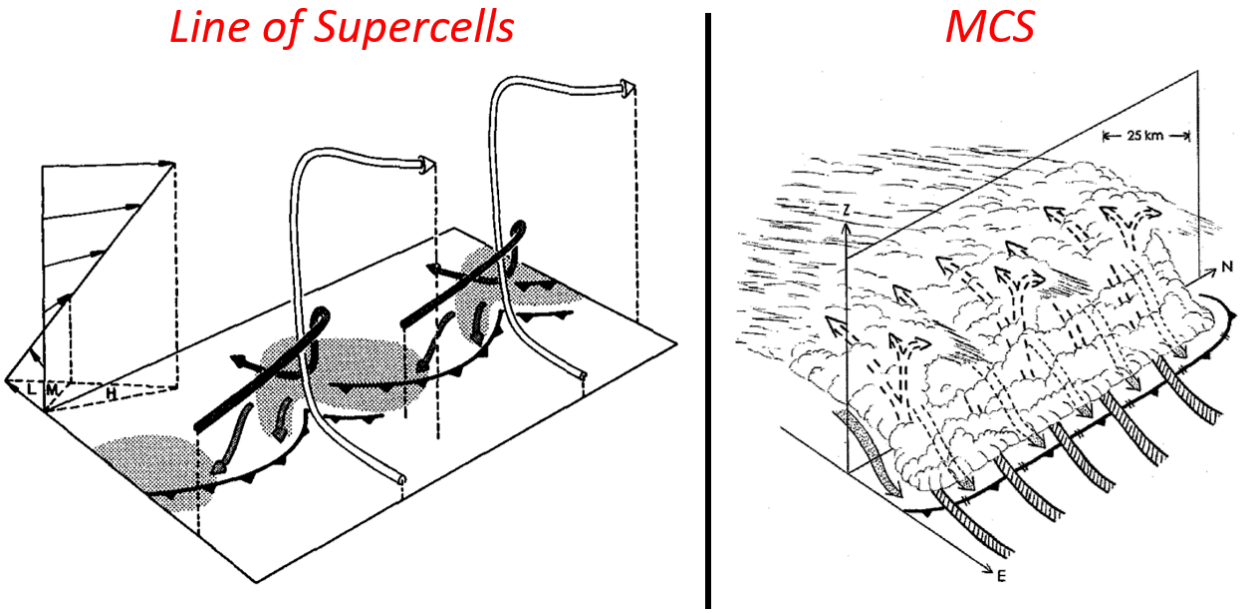

Figure 1.4: Conceptual diagram of a line of supercells (left panel) and a mesoscale convective system (MCS; right panel). In the left panel, light gray shading represents the near-surface rainfall pattern, arrows represent the flow in/around the supercells at various altitudes, and the approximate location of near-surface gust fronts are indicated in standard notation. In the right panel, as in the left panel, but now light gray shading represents cloudy regions. Left panel adapted from Rotunno et al. (1988) and originally from Lilly (1979). Right panel adapted from James et al. (2005).

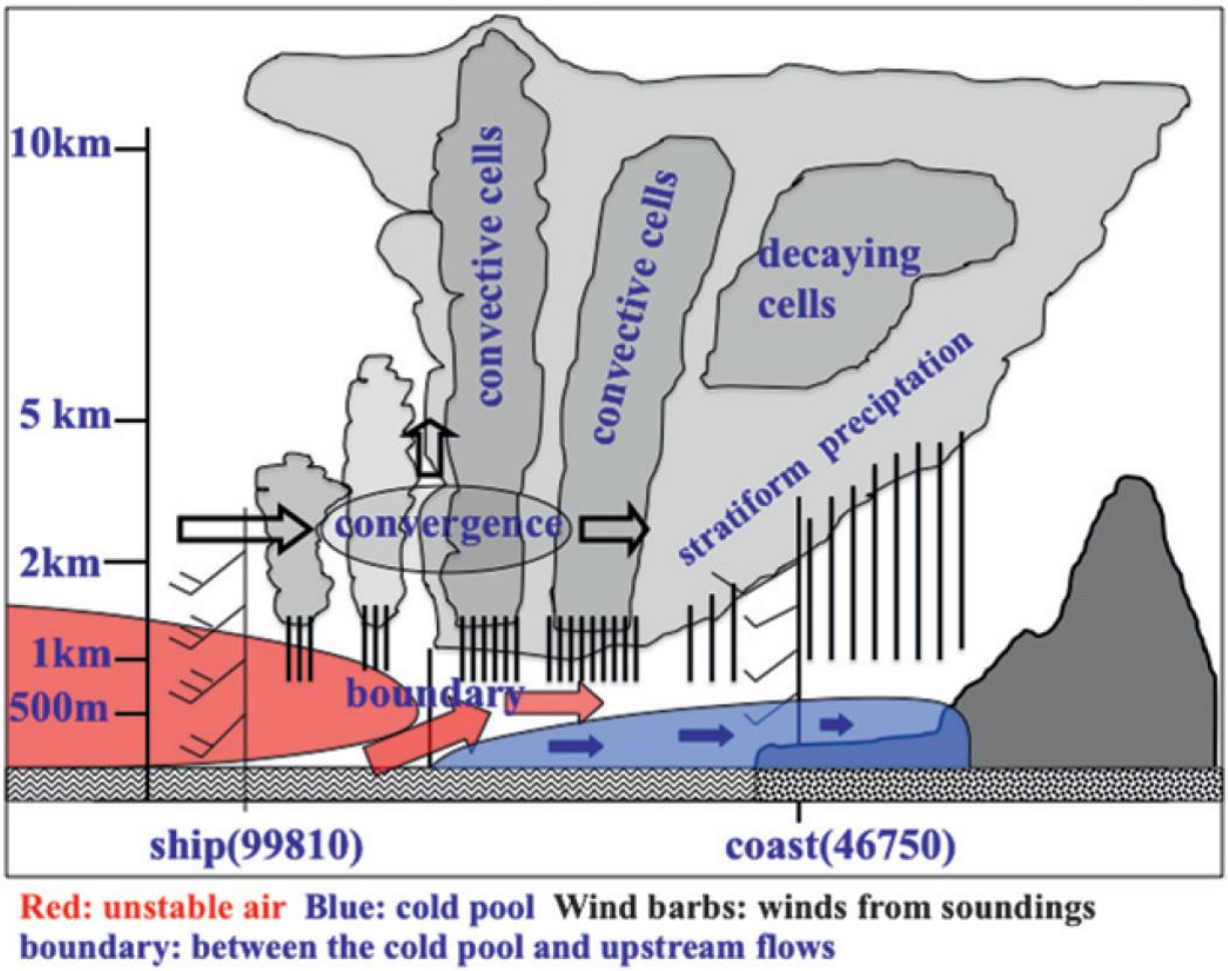

Figure 1.5: Conceptual diagram of convective cold pool blocking by terrain. Cloudy regions are indicated by gray shading, red shading and arrows represent unstable air, blue shading and arrows represent cold pool air, black arrows represent low-to-Midlevel flow, horizontal winds at various altitudes are plotted using standard notation, and rainy regions are indicated by vertical black lines with heavier rain regions located where vertical black lines are more closely spaced. Representative heights are indicated along the left side of the figure. Noteworthy regions are labeled on the figure in blue text.

CHAPTER 2: DATA AND METHODS

Part I: Chapter 3

2.1 Description of the Córdoba C-Band Radar System

RMA1 is a C-band (5.4 cm wavelength), dual-polarization Doppler weather radar that was installed in 2015 and is part of a new operational C-band network in Argentina. This radar system was designed and manufactured by INVAP-South America and is operated by the National System of Meteorological Radars (SINARAME; in Spanish) for the Servico Meteorólogico Nacional of Argentina. RMA1 records data at a range spacing of 480 m, a maximum range of 480 km, and has a beamwidth of 0.98˚ (Table 2.1). RMA1 is a simultaneous transmit and receive dual-polarization radar (Table 2.1); however, within this study, dual-polarization data were not used except for quality control (co-polar correlation coefficient). RMA1 underwent upgrades during the month of November 2016, and thus, many events were likely missed during this time period as the radar was not operating (see Table 3.1).

RMA1 occasionally suffers from radio interference owing to its location within the large city of Córdoba, resulting in erroneous radar echoes (i.e., radial "spikes"). A simple quality control filter was used in this analysis to remove most non meteorological echoes. Radar reflectivity and Doppler radial velocity data were masked out for this analysis if the reflectivity factor was <10 dBZ or co-polar correlation coefficient (ρ_{HV}) was <0.7. Additionally, C-band radars are known to be subject to attenuation, differential attenuation, non-Rayleigh scattering, and backscatter differential phase effects when scanning regions of heavy rain/hail (Fabry 2015; Rauber and Nesbitt 2018); however, for the purposes of this study, these data were not corrected for these effects as non-corrected data were deemed adequate for convective cell tracking and mode classification.

2.2 Córdoba Radar Storm Tracking and Classification

Numerous studies have documented convective modes based upon a unique set of criteria. Most studies have utilized ground-based radar reflectivity signatures as a means of defining convective mode (e.g., Bluestein and Jain 1985; Houze et al. 1990; Klimowski et al. 2004; Trapp et al. 2005; Gallus et al. 2008; Schumann and Roebber 2010; Smith et al. 2012), and thus, a similar procedure has been implemented here.

Convective mode was separated into four categories: 1) multicell-unorganized (MUN), 2) multicell-organized (MCS), 3) discrete-non-supercell (DNS), and 4) discrete-supercell (DSC). These categories were subjectively determined over a radar tracking analysis domain that was centered near the RMA1 site (31.44˚S, 64.19˚W; Fig. 2.1) and spanned 30˚ to 33˚S and 62.5˚ to 66˚W (approximately 300 x 350 km in size).

With 0.5˚ radar reflectivity factor and Doppler radial velocity fields generated using the Python ARM Radar Toolkit (Py-ART; Helmus and Collis 2016), the aforementioned convective mode categories were further restricted by the following criteria (see Figs. 2.2 and 2.3):

1) The multicell-unorganized (MUN) events had to display cells that were ≤25 km from one another with reflectivity ≥30 dBZ.

2) The multicell-organized (MCS) events had to display a region of *contiguous* reflectivity ≥30 dBZ over a horizontal distance of ≥50 km and contained at least one ≥50 dBZ reflectivity core.

3) The discrete-non-supercell (DNS) events had to display non/weakly-rotating cells that were >25 km apart from one another with reflectivity ≥30 dBZ.

4) The discrete-supercell (DSC) events had to display clear rotation (assessed using 0.5˚ radial velocity data) for ≥15 minutes with reflectivity ≥30 dBZ and were typically associated with reflectivity hook echoes, especially closer to the radar (c.f. Fig. 2.3a).

Each of these convective modes were based upon the *dominant* mode throughout the event (e.g., after Gallus et al. 2008). The dominant convective mode was defined as the mode that lasted the longest, or displayed the highest degree of organization (e.g., Schumann and Roebber 2010), throughout an event. Convective cells that were difficult to bin into one of the four above categories were either grouped into the MUN or DNS categories depending on their presence as a time-fraction of the overall convective mode of an event. An "event" was defined as the time interval from CI to system demise, or the time interval over which convection (i.e., reflectivity ≥30 dBZ) entered and exited the domain; CI was defined as the first appearance of a ≥30 dBZ echo (at the 0.5˚ scan angle) over at least five radar gates. If two (or more) different instances of CI occurred on the same day, these were partitioned into two separate events. Events that featured storms that moved into the lateral boundaries of the tracking domain, or lacked radar data at the time of CI, were binned into a separate category. Additionally, of all the total events recorded, any instances of UCG into an MCS (e.g., through a presumed amalgamation of cold pools) from either MUN, DNS, or DSC convective modes was noted (independent of the dominant convective mode characterization). In the context of this chapter of the dissertation, UCG was defined the instant when the length of the *contiguous* ≥30 dBZ radar echo spanned at least 50 km horizontally with ≥50 dBZ embedded cores.

2.3. TRMM Precipitation Radar Storm Identification and Classification

TRMM PR satellite data version 7 (V7; TRMM data accessed from http://trmm.atmos.washington.edu/) were used in this study to compare with the RMA1 analyses,

with the caveat being that the TRMM PR analyses are "snapshots" in time while the ground-based radar provides a temporal characterization of the convection. TRMM PR data have coarse horizontal, but relatively fine vertical resolution of 4–5 km and 250 m, respectively, with an average horizontal swath width of ~220 km and 250 km before and after 7 August 2001, respectively (Kummerow et al. 1998). Events were identified between September 1998–February 2014 over the same tracking domain as the RMA1-identified storms (green box in Fig. 2.1) and were binned into the months of September, October, and November (SON; austral spring), or, December, January, and February (DJF; austral summer). These events were categorized by convective mode in a similar fashion as the RMA1 events; however, owing to the inability of the TRMM PR to deduce rotation within convection, DSC and DNS events (which were defined during the RMA1 tracking) were combined into a single category, "discrete" storms, for the subsequent set of TRMM PR analyses. Rasmussen and Houze (2011) demonstrate that the TRMM PR satellite can discern multicell systems quite well and thus, the MCS and MUN categories remain partitioned for both the TRMM PR and RMA1 tracking. Furthermore, these satellite-identified events were separated into wide convective core (WCC; areal extent of 40 dBZ echo >1000 km^2) and deep convective core (DCC; height of 40 dBZ echo >10 km) categories based upon the classification scheme outlined by Houze et al. (2007). Example events, including vertical cross-sections, of the three convective mode categories defined for the TRMM PR analyses are depicted in Fig. 2.4.

2.4. ERA-Interim Reanalysis Composites

ERA-Interim reanalysis data (Dee et al. 2011) were utilized to characterize the ambient, synoptic-scale environment for convective modes identified from the RMA1 data. ERA-Interim is a global (atmospheric) reanalysis dataset produced by the European Centre for Medium-Range

Weather Forecasts (ECMWF). ERA-Interim reanalysis includes 3 h surface data, 6 h upper-air data, and utilizes four-dimensional variational data assimilation techniques. The horizontal grid spacing is 0.7˚ (approximately 80 km) with 37 vertical model levels (P_{top} = 1 hPa); pressure-level interpolated data were used for this analysis.

Reanalysis data were used to construct composites of synoptic-scale fields such as: 250 hPa height/wind, 850 hPa moisture/wind, mixed-layer CAPE (MLCAPE; averaged over the lowest 100 hPa), mixed-layer CIN (MLCIN; averaged over the lowest 100 hPa), deep-layer and low-level wind shear (calculated as a bulk wind difference between 0–6, 0–3, and 0–1 km AGL), storm-relative helicity (SRH; Davies-Jones 1984; 0–3 and 0–1 km AGL), and others, across the north central Argentine region for the four dominant convective mode categories defined for the RMA1 tracking. Additionally, violin box plots were constructed from the ERA-Interim reanalysis dataset for relevant severe weather indices averaged over the RMA1 tracking domain centered on the RMA1 site utilizing the Sounding and Hodograph Analysis Program in Python (SHARPpy; Blumberg et al. 2017). The reanalysis surface data (2 m air temperature, 10 m winds) were inserted using surface pressure in the pressure level data before constructing model soundings at each grid point.

Part II: Chapter 4

2.5 Observational Data

Radar reflectivity factor and Doppler radial velocity data obtained from RMA1 were used to characterize the convective morphology of this event and otherwise evaluate the accuracy of numerical model simulations described in the following sections. Additional details pertaining to the Córdoba radar specifications can be found in Table 2.1. The 1200 UTC 29 November 2017 upper-air sounding from the Ingeniero Aeronáutico Ambrosio L.V. Taravella International Airport

in Córdoba (World Meteorological Organization site code: 87344) was also compared with numerical model output to verify the control simulation (hereinafter: CTRL-0).

2.6 Numerical Model

The Weather Research and Forecasting (WRF-ARW; version 3.9.1; e.g., Skamarock and Klemp 2008) model was used to simulate the 29 November 2017 event. The innermost grid for the CTRL-0 experiment had a horizontal grid spacing of 333 m (d03; 1117 x 1306 grid points) and was nested within grids with 1 km (d02; 751 x 700 grid points) and 3 km (d01; 952 x 601 grid points) grid spacings, respectively (Fig. 2.5). The outermost 3 km domain was initialized from the 0000 UTC 29 November 2017 National Centers for Environmental Prediction 0.25° Global Forecast System model with lateral boundary updates every 3 h and was integrated forward 30 h until 0600 UTC 30 November 2017 with output saved every 1 h. The 1 km domain was introduced at 1200 UTC and was integrated forward 18 h until 0600 UTC 30 November 2017 with output saved every 5 min (every 1 min for 30 min parcel trajectory analyses). The 333 m domain was implemented just prior to CI (1500 UTC) and was integrated forward for 6 h until 2100 UTC 29 November 2017 with output saved every 1 min. The model simulation had a vertically-stretched grid with 60 vertical levels using a terrain-following σ-coordinate. The model top was at 20 hPa (~20 km AGL) with a 5 km deep absorbing layer to mitigate reflection of vertically-propagating gravity/sound waves off the model top. A full listing of the model configuration and parameterization schemes can be found in Table 2.2.

2.7 Terrain Experiments

To further explore the effects of the SDC on CI, supercell formation, and UCG, four additional WRF experiments were conducted in which the terrain of the SDC was systematically varied. Any terrain features within the SDC with an elevation ≥1000 m were altered for the 3 km

domain and interpolated to the 1 km domain. The terrain was systematically varied following, $h = mh' + b$, where h denotes the altered terrain, h' denotes the original terrain, $m = (f * 2000 - 1000) / (2000 - 1000)$, and $b = 1000 - (m * 1000)$. The five values of f that were used included 0.60, 0.75, 1.00, 1.25, and 1.40, to represent terrain variations of -40% (LOW-40), -25% (LOW-25), 0% (CTRL-0), +25% (HIGH-25), and +40% (HIGH-40), respectively. The HIGH-40 experiment required the use of a greater vertical sound wave propagation coefficient (0.5 instead of the default 0.1) in order to avoid artificial waves from entering the numerical solution. Comparisons between simulations with varying vertical sound wave propagation coefficients displayed negligible differences for pertinent atmospheric fields. All model parameterization schemes used in these simulations were the same as with the CTRL-0 simulation (see Table 2.2). An example vertical cross-section through the central SDC for each of the five terrain experiments is depicted in Fig. 2.6. Maximum terrain height varied from ~3495 m in the HIGH-40 experiment to ~1000 m in the LOW-40 experiment (Fig. 2.6).

As will be shown in the Chapter 3, the CTRL-0 simulation on the 1 km domain closely matched the convective morphology, convective mode, and salient features of the 333 m CTRL-0 simulation, thus, these four terrain experiments were only conducted on the 3 km and 1 km domains. It is acknowledged that at these grid spacings, convective drafts are not fully resolved (e.g., Bryan et al. 2003).

2.8 Definitions

Similar to the methods outlined in Mulholland et al. (2018) and section 2.2, CI was defined for the RMA1 radar data as the first appearance of a ≥30 dBZ echo that covered at least five radar gates at the ~1° scan angle. Similarly, in the WRF simulations, CI was defined as the time when the lowest model-level simulated Rayleigh-regime radar reflectivity was ≥30 dBZ. The supercell

stage for the Córdoba radar data was subjectively determined by examining ~1° radar reflectivity for evidence of a hook-echo that was accompanied by rotation (using Doppler radial velocity data) through higher elevations of the storm lasting ≥30 min. In the WRF simulation, the peak supercell stage was defined as the time that the simulated storm obtained a minimum value of 2–5 km AGL updraft helicity ($UH = \int_{z = 2\ km}^{z = 5\ km} (w \cdot \zeta)\, dz$; where w = vertical velocity [m s^{-1}] and ζ = vertical vorticity [s^{-1}]); Kain et al. 2008; defined as negative for the Southern Hemisphere). UCG was determined from the RMA1 radar data at the time that the length-to-width aspect ratio of the storm (contiguous ~1° radar reflectivity ≥30 dBZ with ≥50 dBZ embedded cores) met, or exceeded, 3:1. In the WRF simulation, UCG was defined at the time that the length-to-width aspect ratio of the simulated storm (contiguous ≥30 dBZ lowest model level reflectivity with ≥50 dBZ embedded cores) met, or exceeded, 3:1.

Cold pools were defined using thermal buoyancy, $B = g\,(\frac{\theta_v - \overline{\theta_v}}{\overline{\theta_v}})$, where g is gravity (m s^{-2}), θ_v is virtual potential temperature (K) and $\overline{\theta_v}$ is the horizontally-averaged virtual potential temperature (K). For each experiment, $\overline{\theta_v}$ was determined from a pre-CI (1500 UTC used for all experiments) θ_v that was then was calculated and spatially-averaged at each model vertical level within a 200 x 200 km domain (for 1 km simulations) and a 133 x 200 km (for the 333 m CTRL-0 simulation) centered on the (peak) simulated supercell location. The vertical depth and horizontal extent of the cold pool were characterized by regions containing $B \leq$ -0.1 m s^{-2}.

Part III: Chapter 5

2.9 Numerical Modeling Setup

To test the aforementioned hypotheses, a series of idealized numerical model simulations were conducted using Cloud Model 1 (CM1; Bryan and Fritsch 2002) version 19.7. CM1 is a fully compressible, nonhydrostatic numerical model. The CM1 simulations conducted with a uniform

horizontal grid spacing of 500 m and a uniform vertical grid spacing of 250 m over a domain with dimensions 324 x 504 x 20 km (648 x 1008 x 80 grid points). Test simulations conducted with a uniform horizontal grid spacing of 250 m and a uniform vertical grid spacing 125 m, and a vertical dimension of 24 km, showed little difference in convective evolution, thus supporting the use of a relatively coarser resolution and shallower domain. The lower boundary condition was semi-slip with the surface exchange coefficient for momentum (C_D) based on Fairall et al. (2003) at low-to-Mid wind speeds, and Donelan (2004) at higher wind speeds (default option in CM1), while the (constant) surface exchange coefficient for enthalpy (C_E) was based on the specified land-use index. The top boundary condition was rigid and free slip. A Rayleigh damping layer (coefficient = 3.33 x 10^{-3} s^{-1}) was applied above 15 km to mitigate the influence of vertically-propagating gravity/sound waves off the model top.

To study the effects of terrain on the UCG of DMC, artificial terrain was implemented in the simulations. The terrain was specified as an oval-shaped mountain that was stretched in the north-south direction to mimic the approximate shape and areal extent of the SDC. The terrain height (Z_s) was modified from the function presented in Döernbrack et al. (2005) and was specified as:

$$Z_s(x,y) = h * [\left(1 + \left(\frac{x}{a}\right)^2 \right)^{-1.5}] \text{ , (1)}$$

where h = halfwidth (2.5 km), a = 10 km, and

$$X = \sqrt{(x + \gamma\, x_{max})^2 + \beta[\,(\alpha\, y + \varphi\, y_{max})^2\,]} \text{ , (2)}$$

where γ = x-position center of terrain (0.65), φ = y-position center of terrain (0.10), β = factor to stretch entire terrain in north-south direction (0.15), α = factor to only stretch maximum terrain height in north-south direction (0.40), x_{max} = 648 (grid points), and y_{max} = 1008 (grid

points). An example plan view of the terrain configuration and west-to-east oriented vertical cross-sections through the terrain peaks for these variable settings is depicted in Fig. 2.7.

Radiation and surface fluxes of heat, moisture, and momentum were included to allow for the development of realistic flows in proximity to the heated artificial terrain. Longwave and shortwave radiation was parameterized using the RRTMG scheme (Iacono et al. 2008) that was derived from the WRF model. The initialization of the radiation scheme included the following specifications: 1200 UTC 25 January 2019 at -31.30°S and -64.21°W (time and location of where the input sounding was located). The radiation scheme was updated every 5 min. All horizontal lateral boundaries were periodic to allow for the diurnal evolution of the initial thermodynamic and wind profiles within the domain. Surface fluxes of heat, moisture, and momentum were parameterized using the Monin-Obukhov similarity theory surface layer model (Grell et al. 1994). The surface fluxes were dependent on the user-specified land use category, which in this study was "irrigated cropland" with a soil moisture availability of 0.5 (as in Nowotarski et al. 2014). A simulation with a land use category with lower soil moisture availability was also conducted ("mixed shrubland/cropland"; soil moisture availability = 0.15). This simulation was disregarded, however, owing to the inherently larger Bowen ratio. This simulation resulted in convective cold pools that were mixed out quickly owing to large surface sensible heat fluxes and did not result in UCG. Due to the coupled atmospheric radiation–land-surface models used in these experiments, grid translation (i.e., uniform wind subtracted from base state winds) was not possible, thus necessitating the relatively large domain size and coarser horizontal and vertical grid spacings. The two moment Morrison microphysics package (Morrison et al. 2009) was used in all simulations with hail as the prognostic rimed ice hydrometeor species. The simulations were integrated for 8 h with model output saved every 5 min. A large time step of 3 s was used to

maintain stability owing to frequent occurrences of maximum upward vertical velocities of ≥80 m s^{-1}. Coriolis acceleration was turned on for a test simulation (latitude = 31.30°N and f = 7.58 x 10^{-5} s^{-1}). The results from this additional simulation (not shown) were qualitatively similar to the simulation with Coriolis acceleration turned off, and thus, the rest of the simulations neglected Coriolis acceleration. A summary of the CM1 configuration is located in Table 2.3.

The input thermodynamic profile for the CM1 simulations was derived from an observed sounding from the Ingeniero Aeronáutico Ambrosio L.V. Taravella International Airport in Córdoba, Argentina, during the *Clouds, Aerosols, and Complex Terrain Interactions* (CACTI; https://www.arm.gov/research/campaigns/amf2018cacti) field campaign (World Meteorological Organization site code: 87344), at 1200 UTC 25 January 2019 (Fig. 2.8a). This particular day featured an orographic supercell that rapidly transitioned into an MCS (Fig. 2.9), similar to the case study presented in Mulholland et al. (2019), Chapter 4 and climatological UCG events documented in Mulholland et al. (2018), Chapter 3. The sounding was characterized by a nocturnal near-surface inversion layer with a surface dewpoint temperature of ~26°C and mixing ratio ~23 g kg^{-1}. CAPE and CIN for an air parcel with properties averaged over the lowest 100 hPa (most unstable parcel) were ~2900 J kg^{-1} (~4552 J kg^{-1}) and ~ -175 J kg^{-1} (~ -117 J kg^{-1}), respectively. The LCL was ~1030 m, level of free convection (LFC) ~2690 m, and equilibrium level (EL) ~15000 m. The input wind profile was based on the analytic quarter circle wind hodograph from Weisman and Klemp (1982) (Fig. 2.8b). The wind hodograph slowly veered with increasing height from southerly to westerly and strengthened over the lowest 2 km AGL, stayed westerly and linearly increased in speed between 2–6 km AGL, and stayed westerly at a constant speed of 20 m s^{-1} above 6 km AGL. The initial near-surface wind was approximately calm and did not contain any upslope component. The input wind hodograph grossly captured the salient features

accompanying orographic supercell-to-MCS UCG events in north central Argentina, i.e., strengthening low-level winds that paralleled the north-south terrain of the SDC, sharp veering of winds with increasing height near the terrain peak, and a gradual increase in the magnitude of westerly winds with increasing height (e.g., see Fig. 15 from Mulholland et al. 2018; also see Fig. 3.11). To remain consistent with a large portion of the established severe convective storms literature, all simulations were based around a Northern Hemisphere-centric framework, i.e., a "right moving" supercell (main focus of paper) was one that deviated to the right of the mean wind/shear and rotated cyclonically (to avoid any confusion with the aforementioned Southern Hemisphere studies).

DMC in the simulations initiated owing to the inclusion of radiation and surface fluxes, which quickly lead to upslope flows and subsequent low-level convergence, ascent, and erosion of ambient CIN. This alleviated the need for a "warm bubble" (e.g., Loftus et al. 2008). To quickly generate realistic turbulence in the simulations, random potential temperature perturbations, with a maximum amplitude of |0.5 K|, were introduced uniformly across the domain below 1 km height AGL in the initial conditions (e.g., Nowotarski et al. 2014; Peters et al. 2019a).

2.10 List of Experiments

To address the main science questions, a series of experiments were devised with different initial terrain height peaks of: 500 m, 1500 m, 2000 m, 2500 m (Control; CTRL), 3000 m, 3500 m, and 4500 m (slightly larger range of terrain heights than used in Mulholland et al. 2019; also see section 2.7). The 2500 m-CTRL simulation best mimicked the approximate height of the SDC. The inclusion of the 2000 m and 3000 m simulations were in order to reveal if there was any "tipping point" for UCG due to more subtle terrain peak changes.

Additionally, a simulation with no terrain (hereinafter FLAT) was conducted across a similar domain as the aforementioned terrain experiments, except longer in the west-to-east direction (504 x 504 x 20 km; 1008 x 1008 x 80 grid points). The FLAT simulation was initialized with a sounding extracted from the inflow region of developing cumulus congestus clouds over the terrain peak in the 4500 m terrain experiment 2.5 h into the simulation (e.g., Figs. 2.10a,b). The sounding and corresponding wind hodograph depicted terrain modifications to the mesoscale environment (indirect influence), such as increased upslope flow and resultant increased vertical wind shear (e.g., Fig. 2.10c). DMC was initiated with a warm bubble due to the omission of radiation, surface fluxes, and friction. The warm bubble had the following characteristics: 10 km horizontal radius, 1.5 km vertical radius, center located 1.5 km AGL, +2 K center maximum potential temperature perturbation, and centered horizontally in the southwest corner of the domain (approximately at the same location as CI in the 4500 m experiment). All other settings for the FLAT experiment were the same as the aforementioned terrain experiments (see Table 2.3). The FLAT experiment was conducted in order to isolate the role of indirect terrain influences on the mesoscale environment affecting UCG while removing the role of direct terrain influences on UCG, such as blocking of cold pools.

2.11 Definitions

A set of criteria were created to objectively compare results from the aforementioned terrain experiments (adapted from Mulholland et al. 2019; also see section 2.8). CI was defined at the time that a ≥40 dBZ radar echo (any size) was located at the lowest model level (e.g., 250 m) and persisted ≥40 dBZ for the duration of the simulation. Peak supercell time was defined at the time where the 5-point running mean 2–5 km AGL UH magnitude reached a maximum value. UCG was defined at the time that the length of the contiguous lowest model-level reflectivity ≥35

dBZ (with ≥50 dBZ cores) was ≥100 km in one horizontal direction with a length-to-width aspect ratio of >2:1 (similar to Houze 1993). UCG analyses were also restricted to a single supercell (specifically, the "right mover") transitioning into an MCS and not the merger of convective cells to form an MCS. Cold pools in the simulations were quantified by calculating the potential temperature perturbation from a spatially averaged potential temperature (updated each time step at every height level) over a 50 x 50 km domain centered in the southeast corner of the full domain. The near-surface -3 K perturbation potential temperature contour was used to characterize the areal and vertical extent of the cold pools (e.g., Marion and Trapp 2019). This domain was located ~50 km away from the lateral boundaries on its southern and eastern sides. This domain reasonably represented the relatively undisturbed (and flat) background environment at each time step.

2.12 Tables and Figures

Type	C-band S.E. radar system (λ = 5.4 cm)
Frequency	5.6 GHz
Peak transmitted power	350 kW
Pulse duration	2 μs
Pulse repetition time	2000 μs
Range spacing	0.48 km
Maximum range	480 km
Beam width	0.98˚
Polarization mode	Simultaneous transmit and receive
Recorded variables	Z, Z_{DR}, ρ_{HV}, V_R, Spectral width, Total differential phase, Time series

Table 2.1: Córdoba radar specifications.

	Specification	Reference (if necessary)
Horizontal grid spacing	3 km; 1 km; 333 m	
Vertical model levels	60	
PBL scheme	YSU	Hong et al. (2006)
Microphysics	Thompson 7-class	Thompson et al. (2008)
Radiation	RRTMG	Iacono et al. (2008)
Land surface model	5-layer thermal diffusion	Dudhia (1996)
Cumulus scheme	None	
Feedback between nests	On	

Table 2.2: Summary of WRF Model Specifications.

Attribute	*Value / setting*	*Notes*
Fully compressible	yes	
Horizontal grid spacing	500 m	
Vertical grid spacing	250 m	
Vertical coordinate	height (m)	
Number of x, y, z grid points	648 x 1008 x 80	
Top (bottom) LBC	free slip (semi-slip)	
North and south LBC	periodic	
East and west LBC	periodic	
Microphysics	Morrison two moment	Morrison et al. (2009)
Diffusion	6th order	
Subgrid turbulence	TKE	
Rayleigh damping	yes	
Dissipative heating	yes	
2nd and 6th order diff. coef.	75 and .04	
Longwave radiation	RRTMG scheme	Iacono et al. (2008)
Shortwave radiation	RRTMG scheme	Iacono et al. (2008)
Surface layer	Monin-Obukhov	Grell et al. (1994)
Land use index	Irrigated cropland	Soil moisture availability = 0.5
Coriolis acceleration	off	
Boundary layer physics	none	
Cumulus parameterization	none	

Table 2.3: Summary of the CM1 configuration.

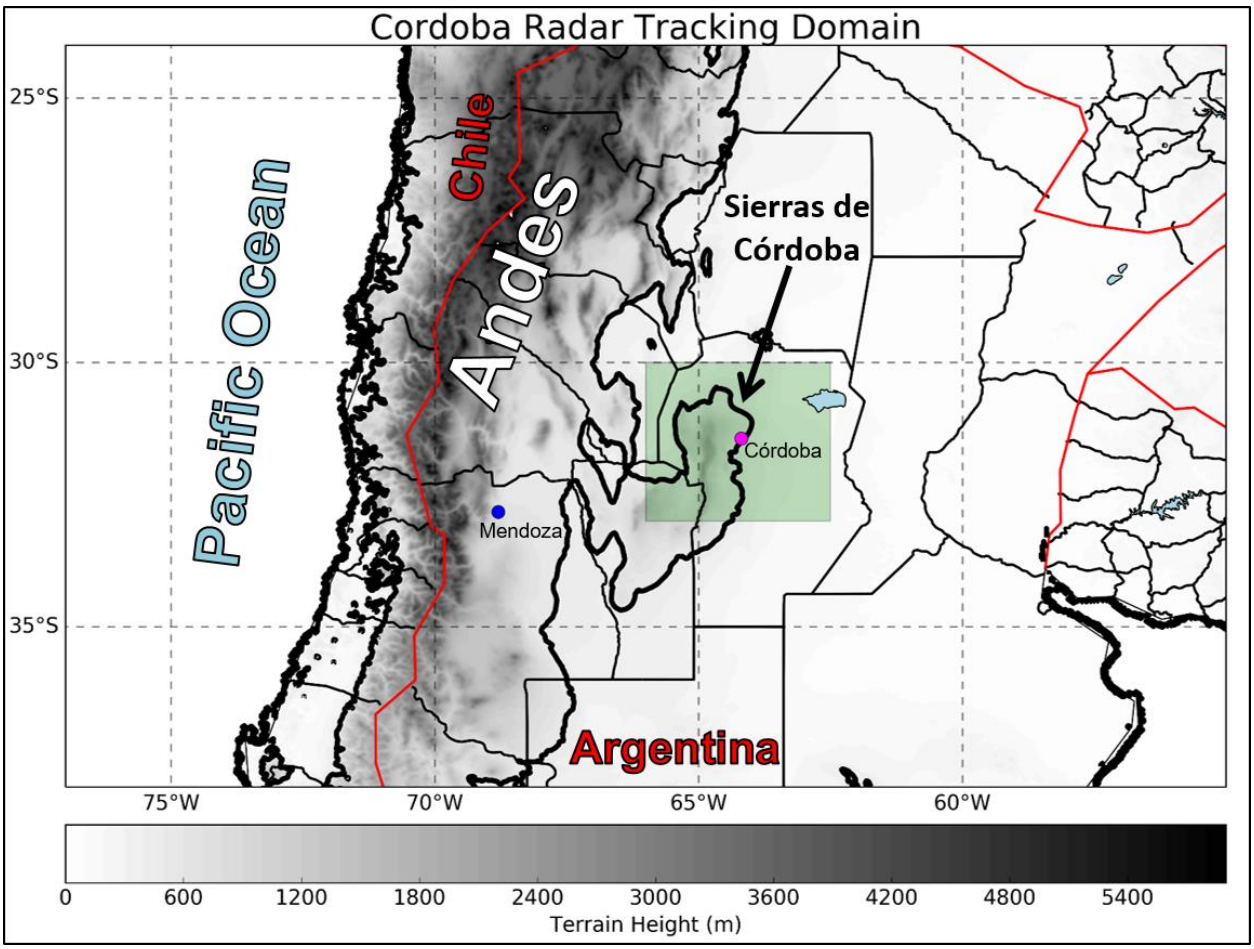

Figure 2.1: Córdoba radar tracking domain (30˚ to 33˚S and 62.5˚ to 66˚W; green box), terrain height (shaded in grey; m), national borders (red line), and the 500 m elevation contour (thick black line).

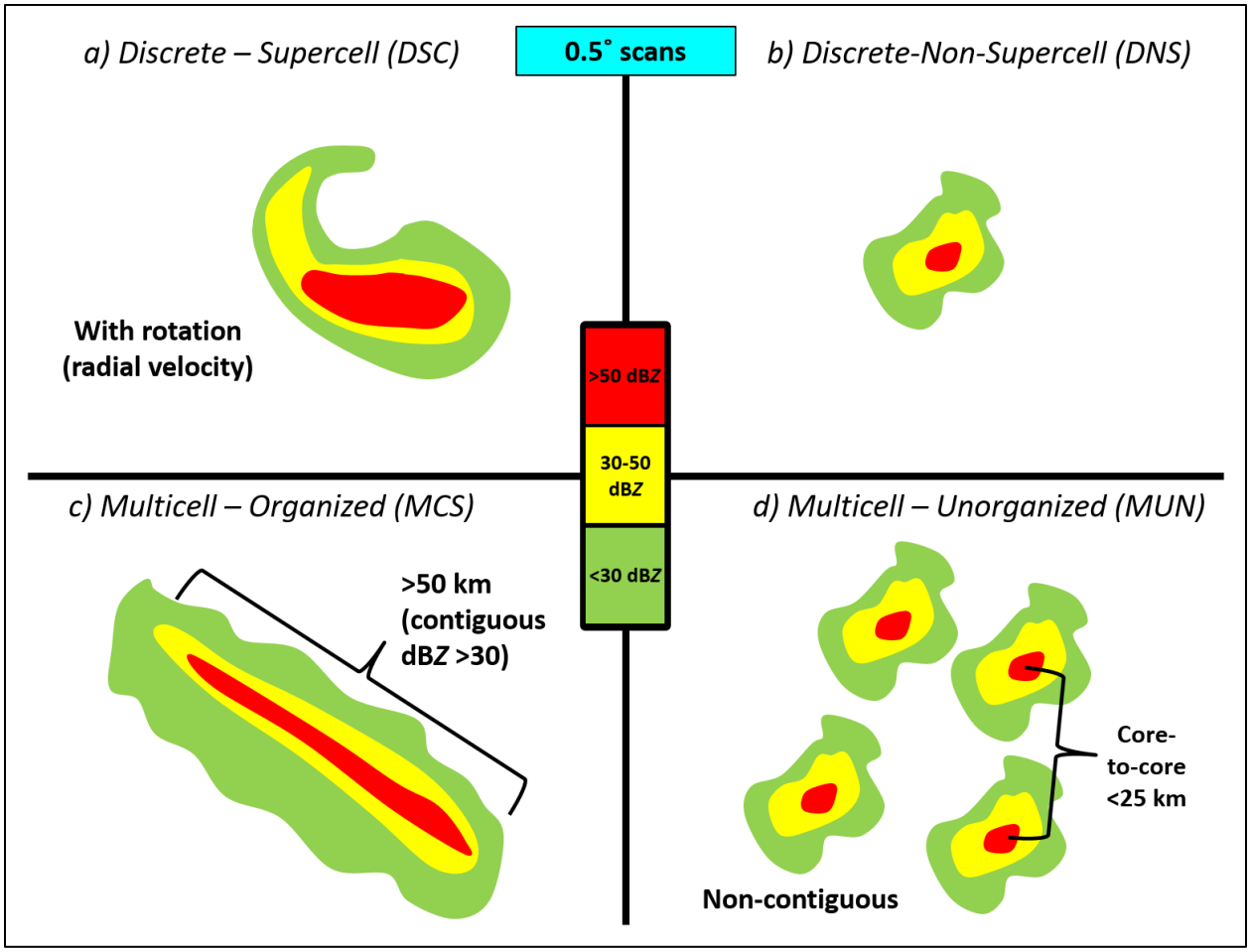

Figure 2.2: Idealized schematic of the four convective modes that were defined for the Córdoba radar tracking: a) discrete-supercell (DSC), b) discrete-non-supercell (DNS), c) multicell-organized (MCS), and d) multicell-unorganized (MUN). The shading corresponds to base radar reflectivity (dBZ).

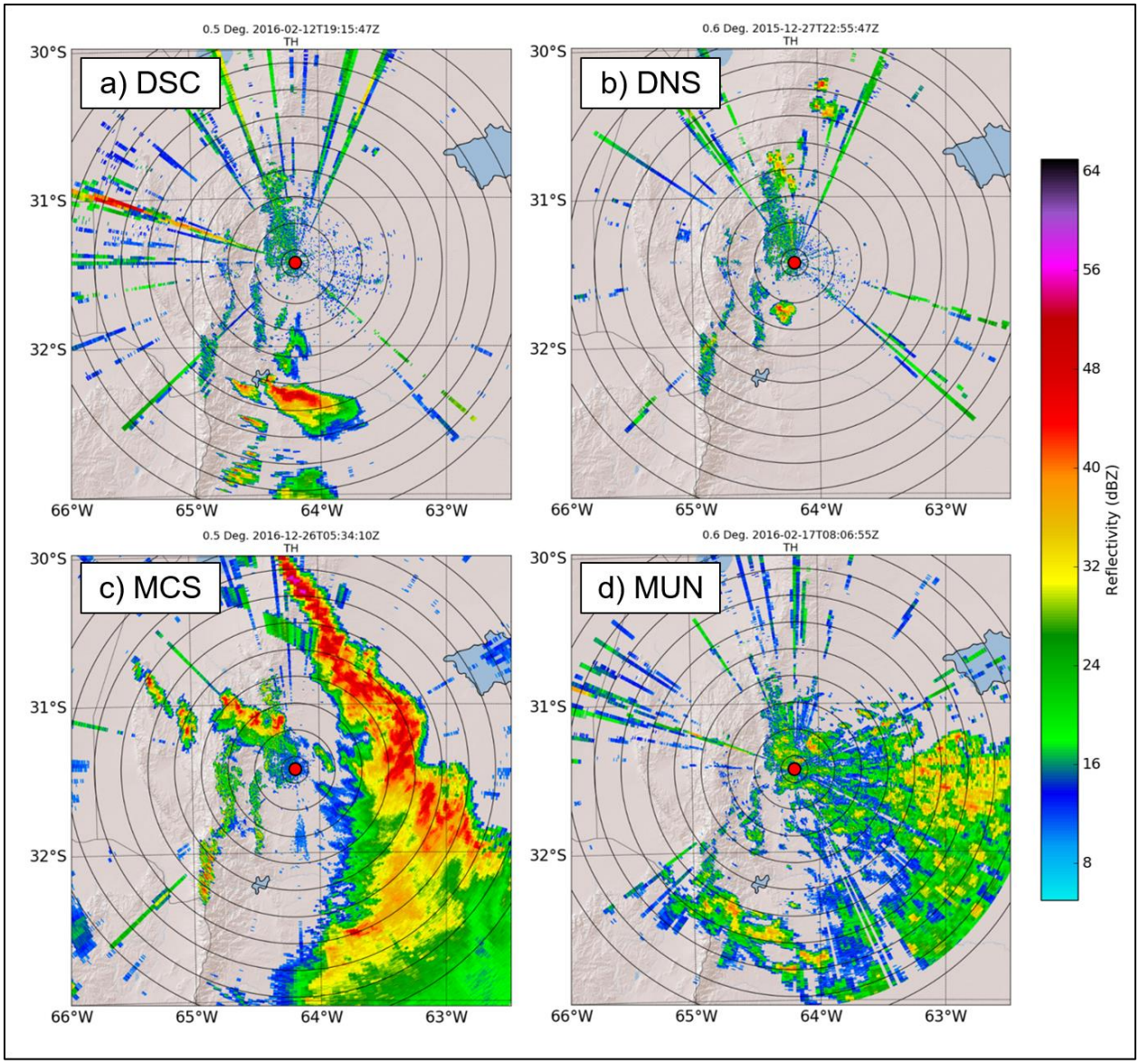

Figure 2.3: Example events of the four convective modes that were defined for the Córdoba radar tracking: a) DSC (1915 UTC 12 February 2016), b) DNS (2255 UTC 27 December 2015), c) MCS (0534 UTC 12 December 2016), and d) MUN (0806 UTC 17 February 2016). The shading denotes 0.5˚ radar reflectivity (dBZ), the red dot denotes the location of the Córdoba radar, and the range rings are spaced every 20 km, with the first range ring from the radar at 10 km.

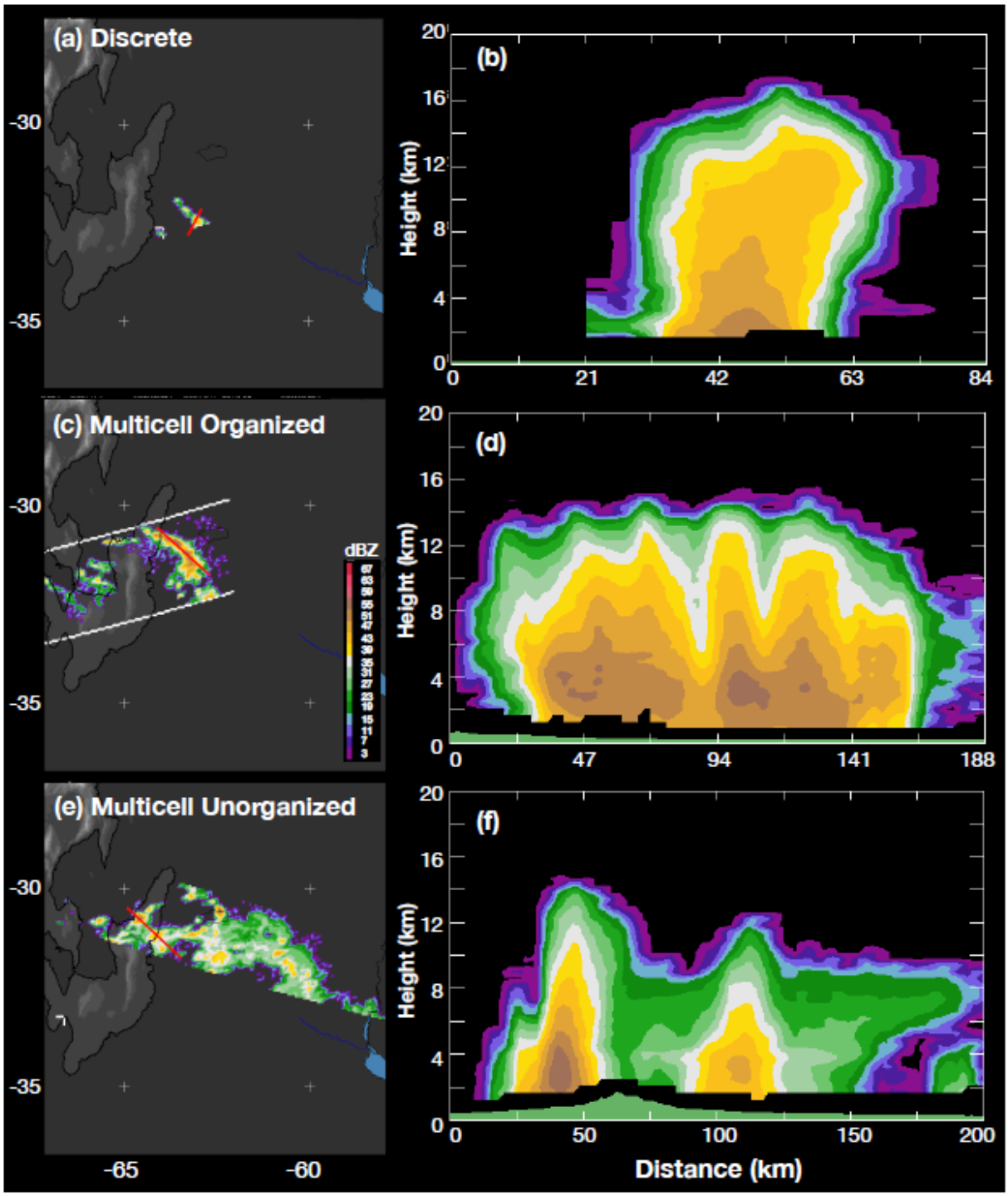

Figure 2.4: Example events identified by the TRMM PR of the (a-b) Discrete (2026 UTC 22 October 1998), (c-d) Multicell Organized (0321 UTC 12 December 2001), and (e-f) Multicell Unorganized (0418 UTC 15 November 1998) convective modes. Panels (b), (d), and (f) show vertical cross-sections taken along the red line in panels (a), (c), and (e), respectively. The radar reflectivity (dBZ) values in all panels are the same.

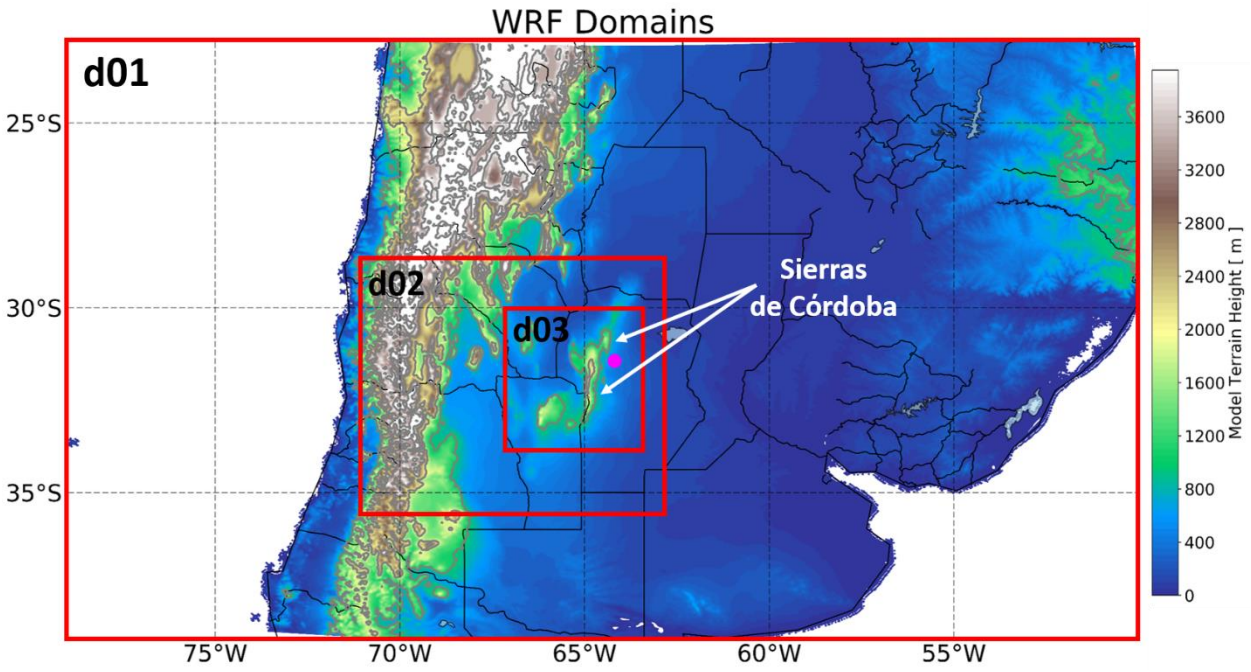

Figure 2.5: The three WRF domains (red boxes) used for simulations: 3 km grid spacing (d01), 1 km grid spacing (d02), and 333 m grid spacing (d03). Terrain height is shaded (m) and contoured in grey (every 500 m). The magenta dot is Córdoba, Argentina.

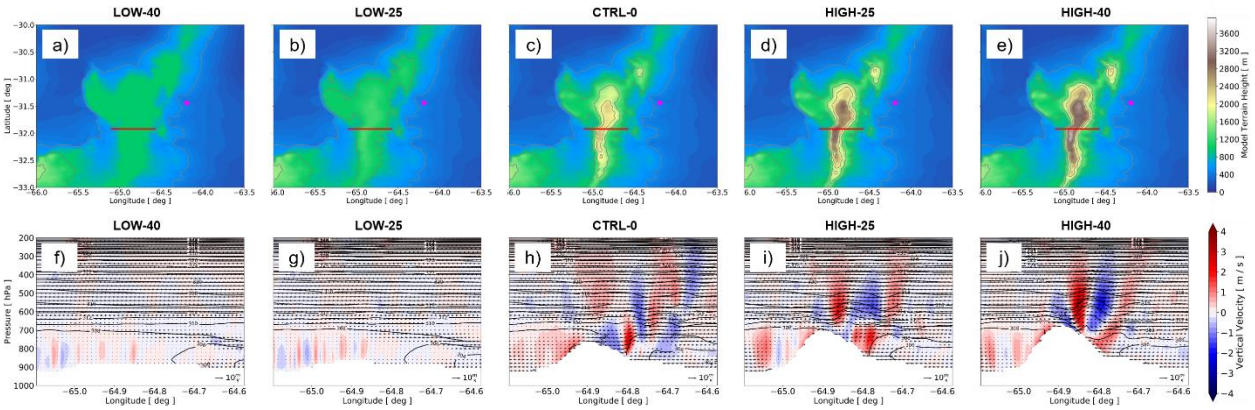

Figure 2.6: 1 km WRF terrain height experiments: (top row) plan views of terrain height (shaded; m) and contoured in grey (every 500 m), city of Córdoba (magenta dot), and the location of the west-to-east oriented vertical cross sections (red lines) shown in the bottom row. (bottom row) vertical cross sections of vertical velocity (shaded; m s^{-1}), in-plane winds (vectors; m s^{-1}), and potential temperature (black contours every 2 K) at 1500 UTC 29 November 2017. (a, f) LOW-40, (b, g) LOW-25, (c, h) CTRL-0, (d, i) HIGH-25, and (e, j) HIGH-40 experiments.

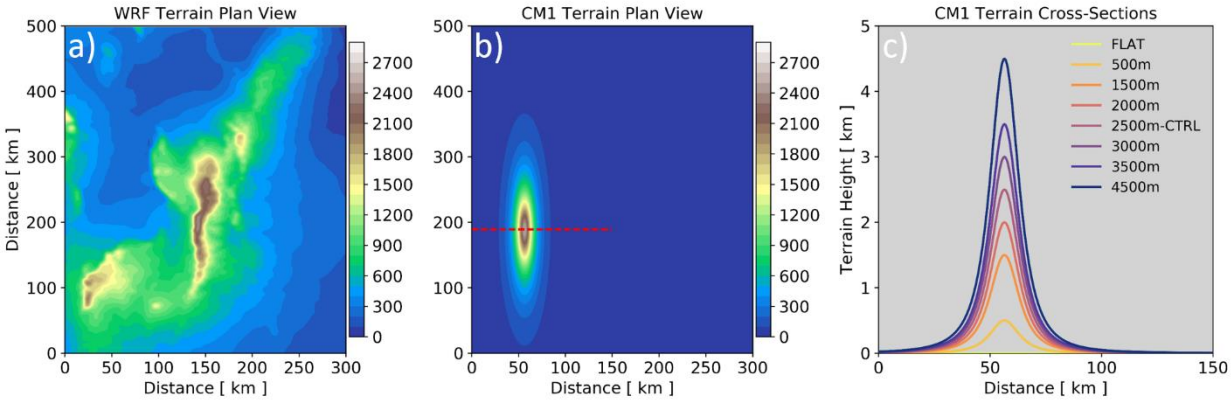

Figure 2.7: (a) Plan view of terrain height (m) from a 1 km WRF simulation (adapted from Mulholland et al. 2019), (b) plan view of terrain height (m) from the 2500m-CTRL CM1 simulation and line along which the west-to-east oriented vertical cross section of terrain is shown in panel (c) (red dashed line), and (c) west-to-east oriented vertical cross sections of terrain height taken through the peak of the terrain for each experiment [km; see red dashed line in panel (b)].

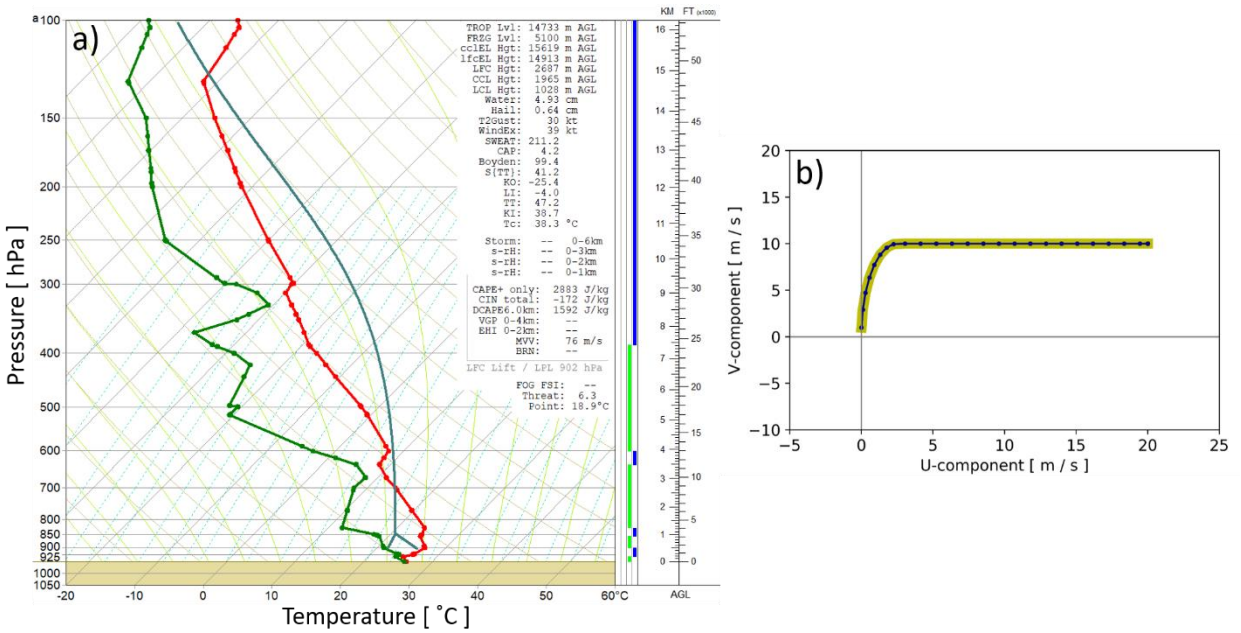

Figure 2.8: Initial background state of the CM1 simulations. (a) 1200 UTC 25 January 2019 Ingeniero Aeronáutico Ambrosio L.V. Taravella International Airport in Córdoba, Argentina, sounding. The red line is the air temperature (˚C), the green line is the dewpoint temperature (˚C), and the smooth dark blue line is the vertical path of a parcel lifted from near the surface having the mean properties of the lowest 100 hPa and (b) modified quarter-circle wind hodograph (from Weisman and Klemp 1982) with the *u*-component of the wind on the *x*-axis (m s^{-1}) and the *v*-component of the wind on the *y*-axis (m s^{-1}). For reference, the 0–6 km AGL bulk wind difference is ~20 m s^{-1}.

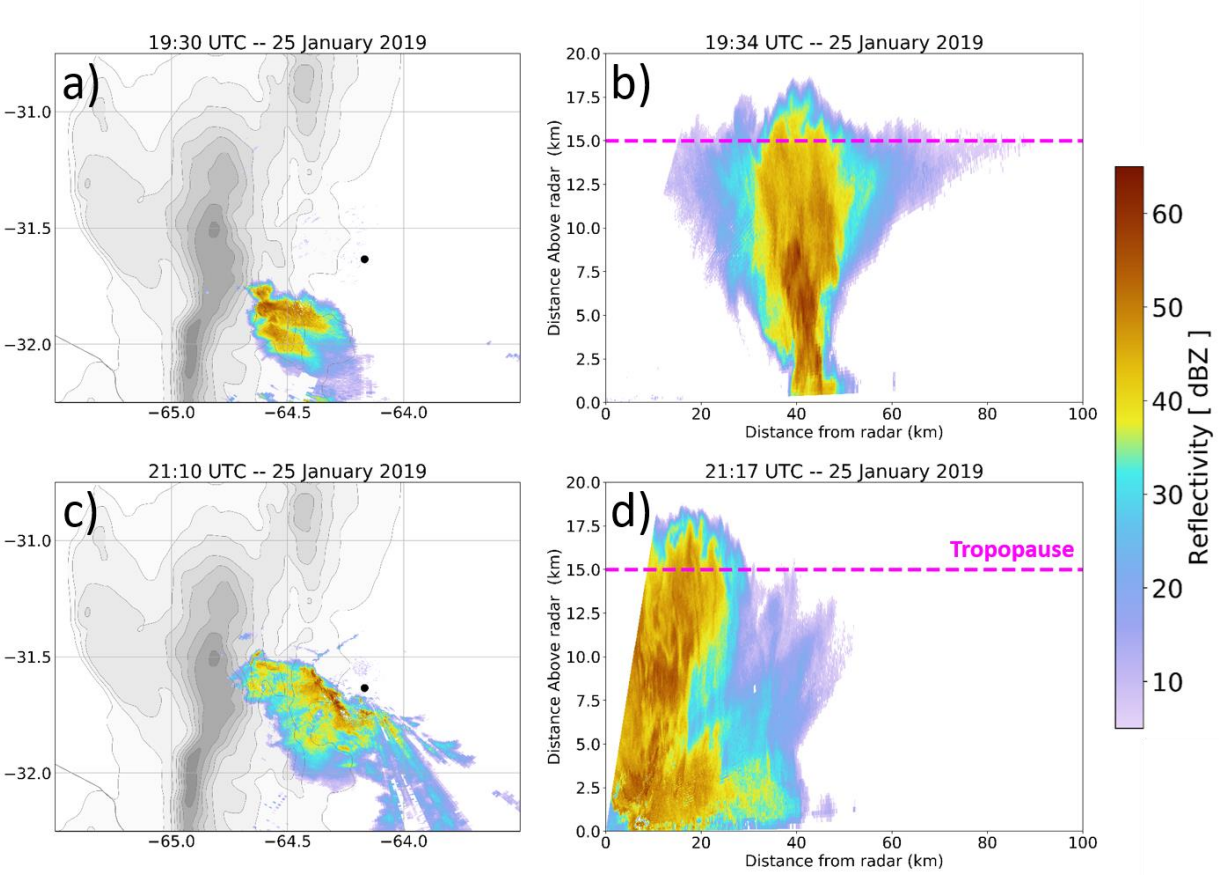

Figure 2.9: Colorado State University C-band radar data. (a) 19:30 UTC 25 January 2019 0.8˚ plan position indicator scan of radar reflectivity (dBZ) and terrain height (shaded and contoured in gray), (b) 19:34 UTC 25 January 2019 205˚ range height indicator scan of radar reflectivity (dBZ), (c) 21:10 UTC 25 January 2019 1.5˚ plan position indicator scan of radar reflectivity (dBZ) and terrain height (shaded and contoured in gray), and (d) 21:17 UTC 25 January 2019 282.5˚ range height indicator scan of radar reflectivity (dBZ). The approximate tropopause location (based upon observed sounding shown in Fig. 2.8a) is marked by the horizontal dashed magenta line in panels (b) and (d).

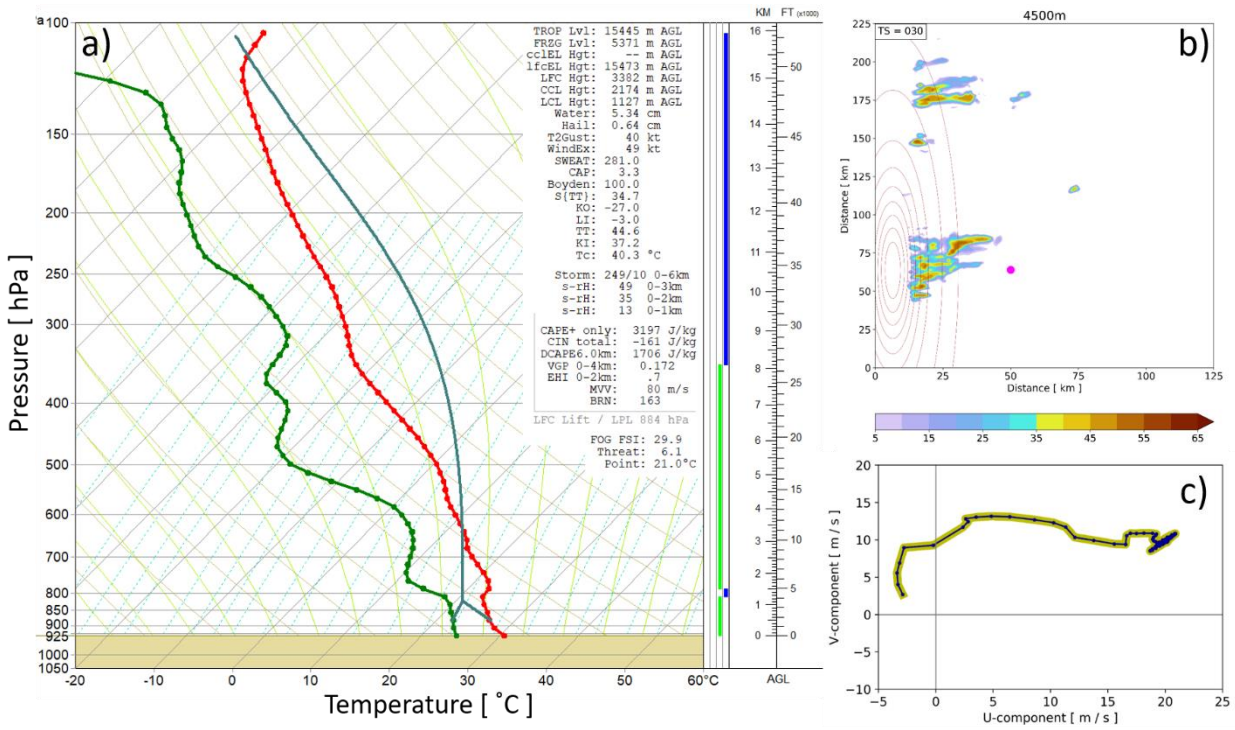

Figure 2.10: (a) Sounding from 2.5 h into the 4500 m terrain experiment. The red line is the air temperature (˚C), the green line is the dewpoint temperature (˚C), and the smooth dark blue line is the vertical path of a parcel lifted from near the surface having the mean properties of the lowest 100 hPa, (b) horizontal plan view of near-surface reflectivity (shaded; dBZ), terrain height (contoured in brown; m), and the location of the model sounding shown in panel (a) (magenta dot) 2.5 h into the 4500 m terrain experiment, and (c) wind hodograph with the *u*-component of the wind on the *x*-axis (m s^{-1}) and the *v*-component of the wind on the *y*-axis (m s^{-1}).

CHAPTER 3: CONVECTIVE STORM LIFE CYCLE AND ENVIRONMENTS NEAR THE SIERRAS DE CÓRDOBA, ARGENTINA

3.1 Córdoba Radar Storm Tracking Statistics

A total of 183 storm events were identified between May 2015–May 2017 documenting different convective modes and subsequent UCG (if applicable). All 183 events were grouped by (any) convective mode present during the event, dominant convective mode throughout the event, CI location/time (within the domain), and time between CI and UCG (if any). In terms of dominant convective mode, 66 (36%) of the events were characterized as MUN, 57 (31%) as MCS, 41 (22%) as DNS, and 19 (11%) as DSC. This distribution in convective mode, with ~67% multicell events and ~33% discrete events, is similar to studies of convection across the central USA (e.g., Schumann and Roebber 2010).

Of the 183 events, 113 had radar data available at the time of CI and additionally had CI within the tracking domain. Most CI events tend to cluster over the steepest gradient in terrain of the SDC, near the city of Villa Yacanto (Fig. 3.1). There is also a secondary peak in CI to the north-northwest of Córdoba. CI additionally occurs over the lower elevations to the east of the SDC, but this is relatively less frequent compared with the number of CI events over the SDC.

All of the CI events were partitioned by their dominant convective mode throughout the lifetime of the event and traced backward to CI location. MCS (Fig. 3.2a) and DSC (Fig. 3.2c) events tend to have CI locations that are near the city of Villa Yacanto, while DSC CI events are clustered over the higher terrain. The DNS events (Fig. 3.2d) almost exclusively initiate over the SDC, whereas the MUN events (Fig. 3.2b) display two main CI centroids, with one maximum near and southwest of Villa Yacanto and a secondary maximum along the northern tip of the SDC (near

30.75˚S, 64.25˚W). Additional MUN events have CI well to the east of Córdoba, across the lower elevations (Fig. 3.2b).

There is a distinct bimodal structure in the temporal distribution of CI, with the first peak in CI occurring between ~1400–1900 UTC (1100–1600 local time) and the second peak occurring between ~2300–0600 UTC (2000–0300 local time; Fig. 3.3). There is a minimum in CI that occurs during the early dawn (0700–1300 UTC; 0400–1000 local time) and the mid-afternoon hours (2000–2300 UTC; 1700–2000 local time). This bimodal structure in CI time in this region has been identified in previous studies of South American MCS events (e.g., Salio et al. 2007; their Fig. 3.3, bottom left panel). The first peak in CI is likely a result of diurnal heating of the SDC and resultant anabatic upslope flows, which subsequently converge on the ridgeline. The secondary peak is more challenging to understand and has not received much study to date, but we hypothesize that a nocturnal acceleration of the SALLJ (e.g., Bonner et al. 1968; Repinaldo et al. 2015) results in enhanced low-level moisture convergence near the unique terrain of the SDC, thus fostering CI there. Furthermore, nocturnal slope flows interacting with the SALLJ could be another potential catalyst for additional CI to occur.

The annual distribution of all 183 events for RMA1 and 372 events for the TRMM PR (also see Section 3b) is depicted in Fig. 3.4, with the number of events from the RMA1 dataset normalized in the following way:

$$(total\ number\ of\ days\ in\ month - days\ with\ available\ radar\ data) * (total\ number\ of\ storm\ counts\ in\ that\ particular\ month).$$

This normalization method was used to account for periods that RMA1 was not operating (see Table 3.1). The austral winter months of May–September were characterized by the fewest number of events, with a large increase in events between October–February (austral spring into summer).

The maximum number of RMA1-identified events (~36) occurred in February (some days have multiple events) whereas the maximum number of TRMM PR-identified events (~95) occurred in November. This RMA1 distribution matches well with the analyses of TRMM PR-identified storms from Rasmussen and Houze (2011; their Fig. 5a for the SDC region) and the TRMM PR storm counts for this study (Section 3.2). MCS events had two peaks, with one in November (9 events) and another in January (14 events; Fig. 3.5). DNS events had an increase in number between October (1 event) and January/February (10 events; Fig. 3.5). The MUN events had a fairly uniform distribution, with a three month peak of 10 events between December–February (Fig. 3.5). Similar to the MCS events, DSC events had two main peaks. The first peak was in November (4 events), whereas the second peak was in February (6 events; Fig. 3.5). Overall, there was a tendency for more discrete convective modes earlier in the austral spring season (October–December) and more multicellular convective modes later in the austral summer season (March–April; Fig. 3.5). This shift from discrete to multicellular convective modes agrees with the average positioning of the large-scale jet stream pattern, with a poleward shift in the jet stream observed during the transition from spring into summer (not shown) and resultant weaker wind shear for more organized convective modes (e.g., supercells).

Of the 113 CI events, 31 (~27%) displayed distinctive UCG into an MCS. The three most prominent pathways for UCG was a transition from MUN-to-MCS (13 of the 31 events; ~42%), DNS-to-MCS (10 of the 31 events; ~32%), and DSC-to-MCS (8 of the 31 events; ~26%). This distribution in UCG by initial/dominant storm mode is similar to the study by Klimowski et al. (2004) in the USA (their Fig. 3). In contrast to the length of events (Fig. 3.6; left violin box plot), the distribution of time from CI to UCG was relatively short (~25% of total “length of event” distribution). This implies a rapid transition from CI to MCS over a fairly short duration of time

(typically less than 3 hours), which is important owing to the overlapping, and eventual transition in severe weather hazards between isolated and multicellular convective modes (e.g., Nielsen et al. 2015).

This implied rapid transition from CI to MCS is further supported by the spatial distribution of CI events and UCG locations depicted in Fig. 3.7. UCG locations were defined as the centroid of the developing MCS when the system first met the aforementioned MCS criteria outlined in Section 2.2 UCG events were characterized by initial cell development across the SDC, and then a rapid transition to MCS just downwind (east) of the terrain (near 32.25˚S, 64.50˚W). The distance between the approximate centroid of CI locations to UCG locations was ~25–50 km, which is *much less* than in the central USA (compared with Fig. 2 from Coniglio et al. 2010). One hypothesis is that as orographic cells over the higher terrain move off to the east, they encounter an environment that is more supportive of rapid UCG. Another hypothesis is that deep convective storms continually develop over the SDC in association with prior cells that move east, off the terrain. This process of backbuilding convection has been highlighted before in this region via TRMM PR data (e.g., Rasmussen et al. 2014) and is noted in some of the UCG events identified using RMA1.

3.2 Comparison with the TRMM PR

To complement the RMA1 tracking results presented above, TRMM-PR-observed convective systems were identified in the same radar-tracking domain previously mentioned during the warm season (September–February) 1998–2014 time period. A total of 372 events were identified: 242 MCS (~65%), 76 discrete (~20%), and 54 MUN (~15%). These events were partitioned into deep convective cores (DCCs; height of 40 dBZ echo >10 km) and wide convective cores (WCCs; areal extent of 40 dBZ echo >1000 km^2) as well. These two categories were further

separated between two time periods: September, October, and November (SON; austral spring) and December, January, and February (DJF; austral summer). A total of 145 (~39%) events were identified during the SON period and 227 (~61%) events were identified during the DJF period (Table 3.2), which had a similar seasonal case partitioning compared with the RMA1 results (Fig. 3.4; SON = ~29% and DJF = ~71%).

The distribution of discrete versus multicellular convective modes between RMA1 data and TRMM PR data are in good quantitative agreement. The results from RMA1 data depicted 60 discrete events (DSC and DNS combined; ~33%) and 123 multicell events (MCS and MUN combined; ~67%) whereas TRMM PR data depicted 76 discrete events (~20%) and 296 multicell events (MCS and MUN combined; ~80%). Owing to the relatively coarse horizontal resolution of the TRMM PR (~4–5 km), the discrete convective modes may be undersampled/spatially smoothed out, resulting in more multicell categorization in TRMM PR data than exists in reality (e.g., Heymsfield et al. 2000). Additionally, the TRMM PR tracking method removes the events that do not qualify as DCC or WCC and thus, there are many more events that were not counted here that might explain this lower percentage of discrete storms. This discrepancy between RMA1 and TRMM PR data might also be true for the categorization between MUN and MCS events, with the MCS category dominating the TRMM PR statistics, whereas the MUN events are more prevalent in the RMA1 statistics. The TRMM PR algorithm for the WCC category requires that storms have a 40 dBZ echo >1000 km^2, potentially resulting in some missed MUN events. The length requirement for MCS events of the ≥30 dBZ echo (≥50 km) likely explains the higher counts of MCS events within the TRMM PR statistics, owing to the coarser horizontal resolution compared with RMA1. Overall, DCCs tend to be associated more with discrete and MCS convective modes during the austral spring months (148 out of 169 total events; ~88%), with a

transition to more MCS DCCs during the austral summer months. WCCs tend to almost exclusively be associated with multicellular convective modes (189 out of 203 total events; ~93%), which is not surprising given the spatial requirements to be considered a WCC previously mentioned.

3.3 Synoptic-Scale Composite Analyses

Storm environments supportive of the different ground-based, RMA1-identified convective modes were constructed via 0.7˚ ERA-Interim reanalysis data. Since ERA-Interim reanalysis data are only available at four times a day (00, 06, 12, and 18 UTC), the time closest (before or after) to CI was chosen to most accurately represent the near-storm environment. Only the 113 CI events, which include 42 MUN events, 33 DNS events, 25 MCS events, and 13 DSC events, were used to generate the following composites.

Both multicell categories (MCS and MUN) tend to be associated with strong flow aloft (>40 kt) with the core of the jet stream displaced to the southeast of the region for MCS events, potentially favoring synoptic-scale ascent (i.e., located within left entrance region of jet streak). MUN events are characterized by a northwesterly flow pattern aloft across the tracking domain (Fig. 3.8b), whereas MCS events display a more westerly component across the tracking domain (Fig. 3.8a). MUN events also tend to have a slightly more amplified upper-level trough off the west coast of South America, potentially resulting in greater quasi-geostrophic (Q-G) forcing for synoptic-scale ascent or supporting frontal intrusions in some events, favoring more widespread CI. The largest differences in the upper-level patterns exist between DSC (Fig. 3.8c) and DNS (Fig. 3.8d) events. DSC events tend to be associated with strong flow aloft just upstream of the tracking domain (>50 kt) and a highly-amplified upper-level trough to the southwest of central Chile. The core of the jet stream tends to be located just off the west coast of South America for

DSC events, with the highest jet speeds impinging on the Andes Cordillera and the terminus of the jet streak over the SDC. This upper-level pattern favors lee troughing (e.g., Lichtenstein 1980; Seluchi et al. 2003; Saulo et al. 2004; Saulo et al. 2007; Rasmussen and Houze 2016) and subsequent (possible) formation of a LLJ owing to the indirect transverse ageostrophic secondary circulation at the terminus of the jet streak (e.g., Uccellini 1980). DNS events are characterized by the weakest flow aloft of all convective modes and subsequent weakest (implied) upper-level wind shear.

All convective modes are associated with lee troughing and resultant northerly low-level flow, serving to transport moisture poleward from the Amazon rainforest region. The multicell categories tend to display a more pronounced LLJ signature that penetrates farther poleward than the discrete categories (compare Figs. 3.9a, b with Figs. 3.9c, d). This results in more focused low-level moisture convergence near the SDC (not shown). The DSC events tend to have the greatest low-level moisture content near the Córdoba region, with mean 850 hPa specific humidity values of ~12–14 g kg^{-1}, and the strongest mean low-level wind speeds (>10 kt) within the tracking domain (Fig. 3.9c). The DNS events tend to have the weakest mean low-level flow and the lowest mean 850 hPa specific humidity values near the SDC (Fig. 3.9d). In comparison with the limited observations of the SALLJ, the ERA-Interim composites presented here generally depict a weaker LLJ (Fig. 3.9; compared with results from Vera et al. 2006). Underestimation of the SALLJ may be due to the compositing procedure of a relatively large number of events per convective mode category.

3.4 Environmental Parameters

Over the radar-tracking domain, DSC events tend to have the greatest mean MLCAPE (~1000–2000 J kg^{-1}) and mean 0–6 km AGL wind shear (~30–35 kt) of all the convective modes

(Fig. 3.10c). This is consistent with Figs. 3.8c and 3.9c, which depict the strongest flow aloft and greatest low-level moisture content for DSC events. DSC events also display the greatest magnitudes of mean MLCAPE and mean wind shear to the east of the SDC. The MUN events display the weakest mean MLCAPE, generally under ~750 J kg^{-1} (Fig. 3.10b). MCS events are similar to DSC events in their thermodynamic and kinematic environments, with average MLCAPE and wind shear magnitudes of ~1000–1500 J kg^{-1} and 30–35 kt, respectively (Fig. 3.10a). The local maximum in MLCAPE in the northwest corner of the 7˚ x 7˚ domain in both MCS and DSC composites likely owes to the greater low-level moisture evident in Figs. 3.9a, c. DNS events are characterized by MLCAPE magnitudes ~750–1250 J kg^{-1} and wind shear magnitudes ~25–30 kt, which is weaker than the other convective modes (Fig. 3.10d). All four convective modes display similar MLCIN magnitudes, with a local minimum over the SDC, while MCS events (Fig. 3.10a) exhibit the strongest magnitudes of MLCIN to the north of the SDC.

Composite mean wind hodographs (constructed at a model grid point closest to Córdoba) for all convective modes are characterized by a veering of the wind shear vector throughout the lower troposphere, indicative of low-level warm air/moisture advection (Fig. 3.11). These wind hodographs are similar to those constructed for the TRMM PR-identified storms presented in Rasmussen and Houze (2011) and in EML events identified by Ribeiro and Bosart (2018). DSC events display the greatest low-level hodograph curvature, whereas DNS events show the least amount; 0–3 km SRH magnitudes are greater for DSC events as compared to DNS events as a result (~ -70 m^2 s^{-2} versus ~ -49 m^2 s^{-2}). MCS and MUN events display similar low-level hodographs; however, MUN events are characterized by a more northwest flow component aloft, in agreement with the upper-level pattern depicted in Fig. 3.8b. Similar west/northwest upper-level flow magnitudes (>40 kt), and subsequent deep-layer wind shear magnitudes, are apparent for each

of the convective modes with MCS environments characterized by the largest magnitudes of mean 0–6 km AGL wind shear (~36 kt) and DNS environments the least (~30 kt).

ERA-Interim reanalysis composite violin box plots were constructed by averaging quantities over a domain centered on the RMA1 site. MLCAPE magnitudes tend to be greatest for DSC events, with a median value ~1500 J kg^{-1} (Fig. 3.12a), similar to the results from Thompson et al. (2012) for supercell environments in the USA. Some DSC events, however, formed in environments with maximum MLCAPE magnitudes of >3500 J kg^{-1} (most-unstable CAPE >6000 J kg^{-1}; not shown), likely supportive of the TRMM PR-identified DCCs (some 40 dBZ echo tops reaching >14 km AGL). MCS and DNS events have similar median MLCAPE magnitudes ~700 J kg^{-1}, whereas MUN events have the lowest MLCAPE magnitudes, with a median value ~300 J kg^{-1}. MLCIN magnitudes amongst the four convective modes tend to be similar across events, with an average median value ~ -80 J kg^{-1} (Fig. 3.12b). These magnitudes of MLCIN tend to be greater than their USA counterparts for supercell and MCS environments analyzed by Thompson et al. (2012; their Fig. 7) and fairly similar (within ~20 J kg^{-1}) to those associated with prominent EMLs across South America reported by Ribeiro and Bosart (2018; their Fig. 15b).

Mixed-layer LCL (MLLCL; averaged over the lowest 100 hPa) heights for the four convective modes are depicted in Fig. 12c. MUN events tend to have the lowest MLLCL heights, with a median value ~1000 m. MCS, DSC, and DNS events have similar median values of MLLCL heights, with an average ~1300 m. The DSC events have similar MLLCL heights as the USA analyzed supercell storms; however, MCS events display slightly higher MLLCL heights in the South American analyzed storms (compared with Fig. 6 from Thompson et al. 2012). The higher average MLLCL heights in these MCS environments may be supportive of more subcloud evaporation, potentially fostering more rapid UCG via cold pool amalgamation.

Deep-layer wind shear (0–6 km AGL) magnitudes among the four convective modes are similar, with median values ranging from ~30–40 kt (Fig. 3.12d). These median values of wind shear tend to be weaker than in USA storm environments, specifically for MCS and DSC events (e.g., Thompson et al. 2012). 0–3 km SRH magnitudes among the four convective modes are fairly similar, with a median value ~ -65 $m^2 s^{-2}$ (Fig. 3.12e). MCS and MUN environments tend to have the largest 0–3 km SRH magnitudes (~ -300 to -250 $m^2 s^{-2}$), likely owing to the stronger SALLJ in these events (e.g., Fig. 3.9a). DSC events have maximum SRH magnitudes of ~ -150 $m^2 s^{-2}$. DNS and MUN events display large spread of SRH, with values ranging from ~ -300 $m^2 s^{-2}$ to 30 $m^2 s^{-2}$. The magnitudes of 0–1 km SRH (specifically for MCS and DSC events) tend to be much lower than their USA counterparts (Fig. 3.12f; e.g., Thompson et al. 2012), which might assist in the explanation of the observed rapid UCG of orographic convection into MCSs for some events. Incipient convective outflows may be unable to stay restricted to their parent storm in these weaker low-level flow/shear environments, fostering more rapid UCG than the USA observed storms (see Figs. 3.6 and 3.7).

3.5 Summary and Conclusions

Satellite observations have revealed that some of the world's most intense convective storms on Earth occur in northern and central Argentina, South America, typically displaying deep and wide convective cores, and are associated with the full range of severe weather hazards. Past studies have characterized the frequency and three-dimensional characteristics of these convective storms using TRMM PR data; however, these data were unable to discern the temporal evolution of convection and distinguish supercell from non-supercell storms. A newly-installed C-band, dual-polarization Doppler weather radar located in the city of Córdoba has allowed for characterization of common convective modes across a region surrounding the northern SDC.

A total of 183 events were identified between May 2015–May 2017, with nearly two-thirds of these events characterized as multicell convective storms. Most convection initiates preferentially in two parts of the SDC (on the high central terrain and the northern tip) and subsequently tracks eastward. There are two distinct peaks of CI time, with one in the late morning-early afternoon hours (1100–1600 local time) and another around sunset (2000–0300 local time). The annual cycle reveals that the most active months for deep convective storms near the SDC are between November–February, or during the transition from austral spring into summer. Discrete convective modes tend to be favored earlier in the austral spring season, whereas multicellular convective modes are skewed toward later in the spring season and into the summer season.

The overall characterization of convection into multicellular (MCS and MUN combined) vs. discrete (DSC and DNS combined) convective modes between RMA1 data and TRMM PR data are fairly consistent (within 10–15% occurrence fraction of each other). Both radars reveal that most events are binned into the multicell categories (≥67%), whereas a smaller fraction of events are binned into the discrete category (≤33%). Both RMA1 data and TRMM PR data reveal that most events occur between December–February (≥69%; austral summer) with less between September–November (≤31%; austral spring).

Of the 113 events that had CI within the domain and had radar data available at the time of CI, 31 (~27%) displayed distinctive UCG into an MCS. UCG tends to occur relatively fast compared with the central USA, usually within the first three hours following CI, and occurs relatively close and to the east of the steepest gradient in terrain in the central SDC. High-resolution numerical modeling presented in Chapters 4 and 5 investigates the mechanisms for this relatively fast transition from first storms to MCSs as this process has sensible weather impacts, such as severe weather hazard type.

ERA-Interim reanalysis composites were constructed for the different convective modes identified by the Córdoba radar. All convective modes are typically associated with strong upper-level westerly flow, with DSC events exhibiting the strongest upstream flow fields. The largest amplitude (upstream) upper-level trough tends to occur during MUN events, where removal of any capping inversion is hypothesized to lead to widespread CI. The low-level environments among the four different modes are generally similar, despite DSC events displaying more moisture than the other convective modes, and are characterized by lee-side troughing, owing to the westerly flow aloft over the Andes Cordillera, and subsequent poleward intrusions of warm/moist air from the Amazon rainforest region. Low-level winds and moisture content tend to be greatest in DSC environments whereas the strongest (upstream) low-level jet feature is associated with MCS and MUN environments.

Composites of MLCAPE and deep-layer wind shear reveal that DSC events are comprised of large magnitudes of both severe weather parameters, over a widespread west-to-east region near the SDC. Compared with USA environments supportive of MCSs and DSCs, Argentina storm environments generally display larger magnitudes of MLCAPE and MLCIN, weaker low-level wind shear/SRH, and higher MLLCL heights. The generally weaker low-level wind shear and higher MLLCL heights constituting these environments may be possible factors in the observed fast transition from first storms to MCSs previously described. One caveat of this analysis, beyond inherent resolution issues and biases in any reanalysis product, is the ability of the ERA-Interim reanalysis to resolve the impacts of complex terrain near the SDC on flow and thermodynamic fields related to deep convective life cycle, which can only be ameliorated by additional observations. Data from the *Remote Sensing of Electrification, Lightning, and Mesoscale/microscale Processes with Adaptive Ground Observations* (RELAMPAGO) field

campaign (1 November–18 December 2018; https://publish.illinois.edu/relampago/), should be used in the future to address hypotheses posed herein. This field campaign documented intense convective storms via a multitude of observing platforms, including, but not limited to: three mobile Doppler-on-Wheels radars (Wurman et al. 1997), fixed radar sites, the Department of Energy Atmospheric Radiation Measurement Climate Research Facility Gulfstream-I aircraft (Schmid et al. 2014), mobile and fixed rawinsondes, mobile mesonets and pods, among others. These data will undoubtedly enhance our understanding of the processes regulating some of the world's most intense deep convective storms near the unique terrain of the SDC.

3.6 Tables and Figures

Month	Year	Number of Days	Number of 0.5˚ Scans
May	2015	22	3456
June	2015	26	4437
July	2015	26	3801
August	2015	28	5100
September	2015	28	3954
October	2015	30	2939
November	2015	28	5477
December	2015	27	2886
January	2016	25	3793
February	2016	23	3811
March	2016	30	3885
April	2016	28	3497
May	2016	25	4603
June	2016	0	0
July	2016	0	0
August	2016	0	0
September	2016	0	0
October	2016	28	1738
November	2016	19	1509
December	2016	26	12012
January	2017	28	10446
February	2017	27	10027
March	2017	30	7948
April	2017	29	8561
May	2017	30	8975

Table 3.1: RMA1 number of days and 0.5˚ scans by month.

Convective Mode	*DCC (spring)*	*WCC (spring)*	*DCC (summer)*	*WCC (summer)*	**Total**
Discrete	29	6	33	8	**76**
Multicell-Unorganized (MUN)	13	14	8	19	**54**
Multicell-Organized (MCS)	29	54	57	102	**242**
Total	**71**	**74**	**98**	**129**	**372**

Table 3.2: Counts of TRMM PR-identified storms by convective mode, DCC vs. WCC, and time of year (austral spring or summer).

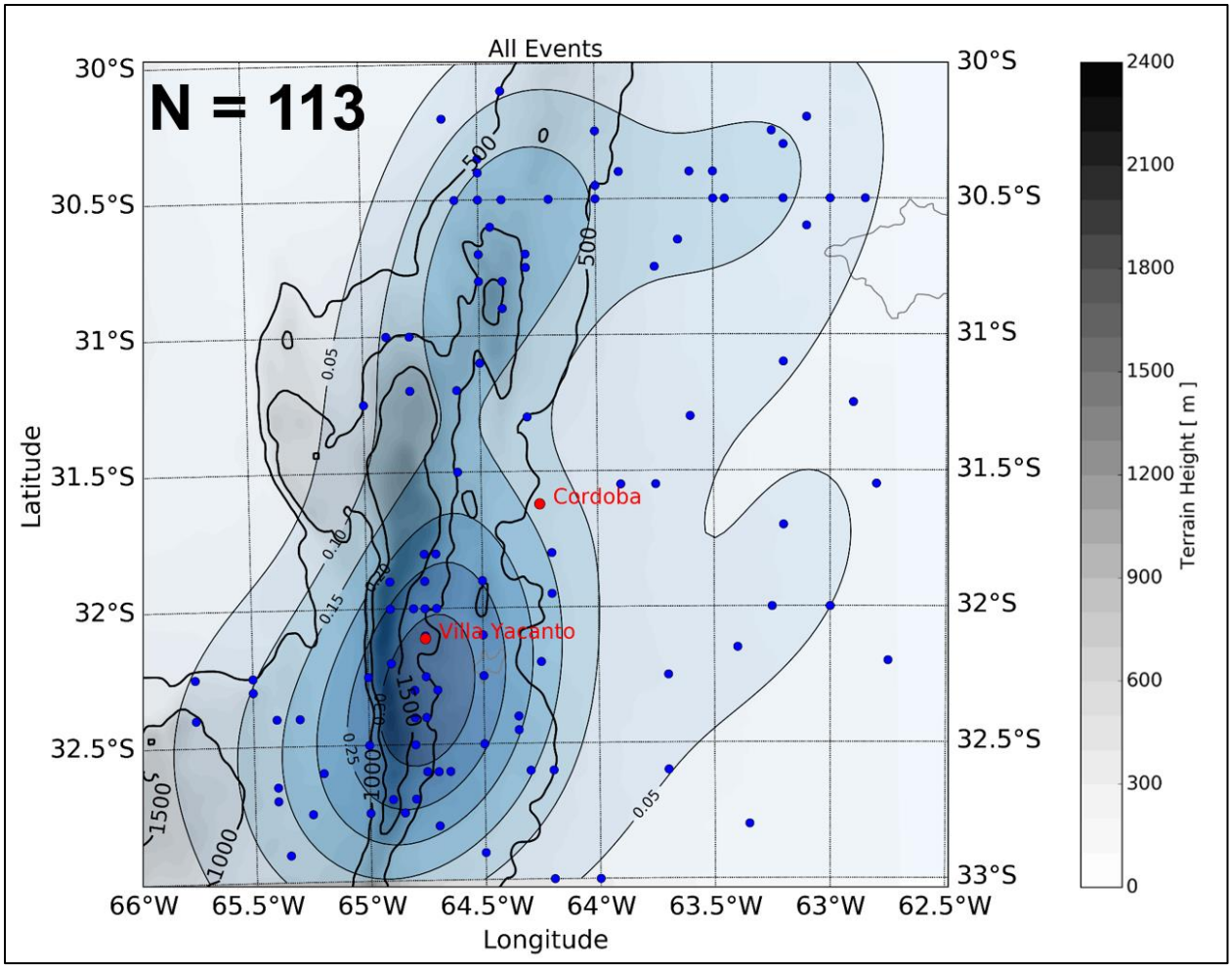

Figure 3.1: Spatial distribution of all 113 CI locations (blue dots) and a kernel density estimation (KDE; using Scott's Rule; Scott 1992) of these locations (blue shades). KDE contours are thin black lines every 0.05, starting at 0.05. The cities of Córdoba and Villa Yacanto are labeled in red. Terrain contours of 500, 1000, and 1500 m are outlined in thick black lines and terrain height is shaded in grey (m).

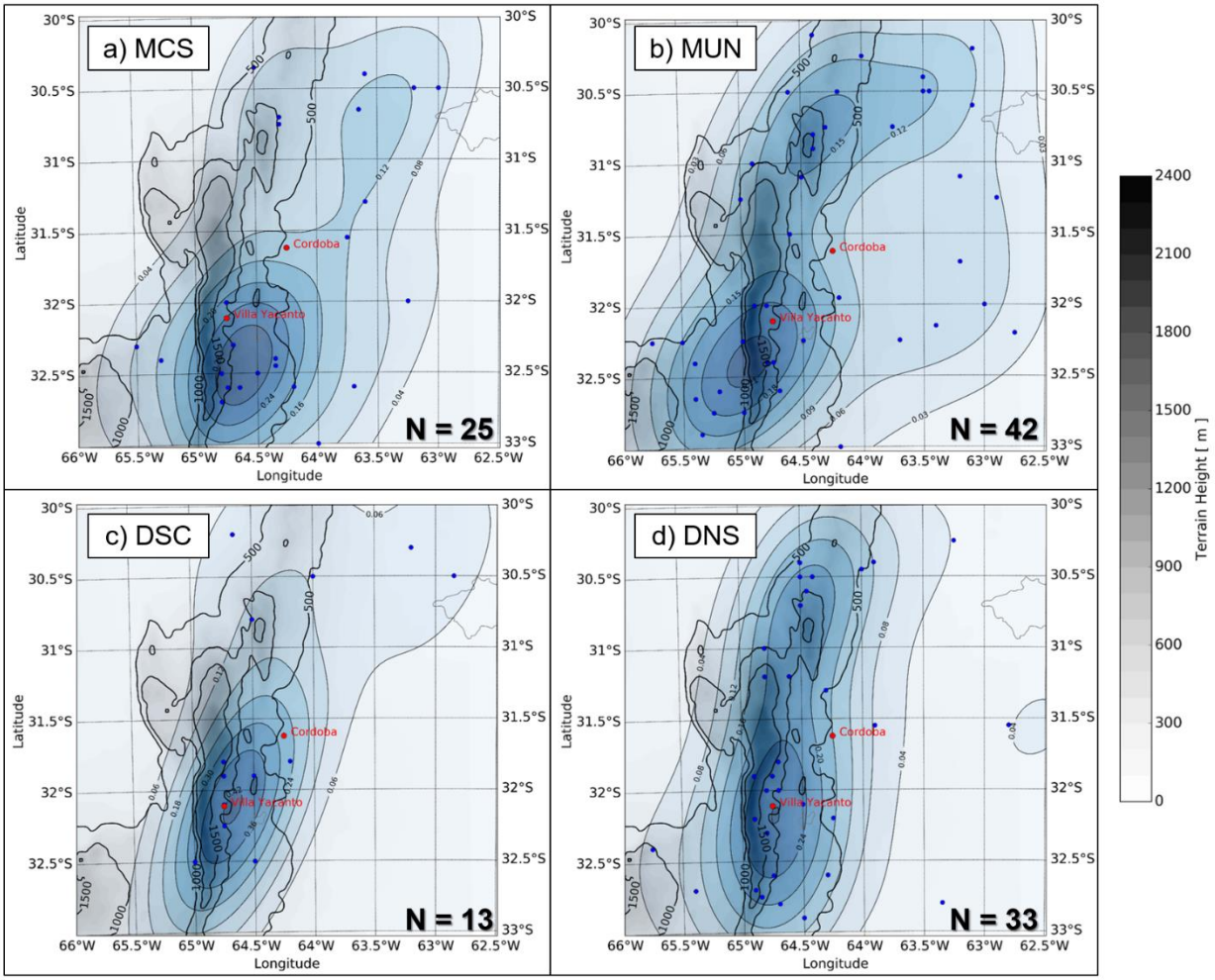

Figure 3.2: As in Fig. 3.1, but by dominant convective mode: a) MCS, b) MUN, c) DSC, and d) DNS.

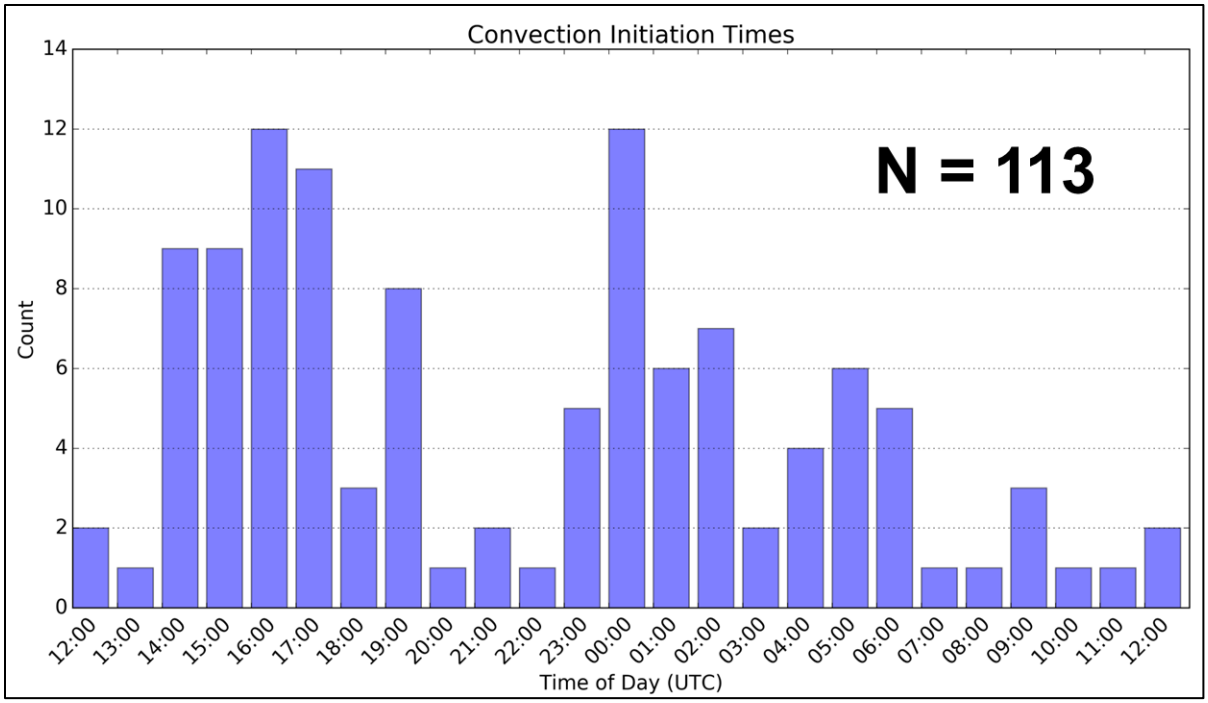

Figure 3.3: Temporal distribution of CI times (UTC) for all convective modes.

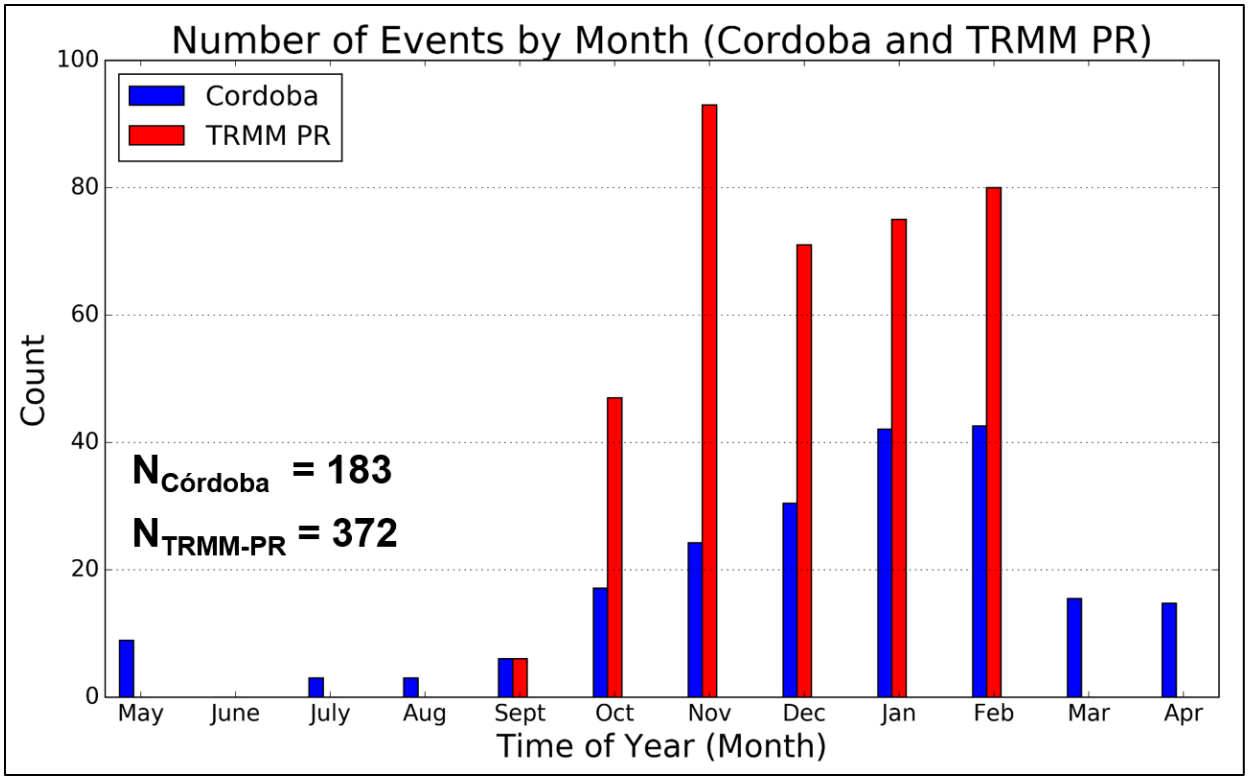

Figure 3.4: Annual distribution of the number of events per month over the full two year tracking period for Córdoba radar data, normalized by the number of days with available radar data per month (see text for details), and TRMM PR data

.

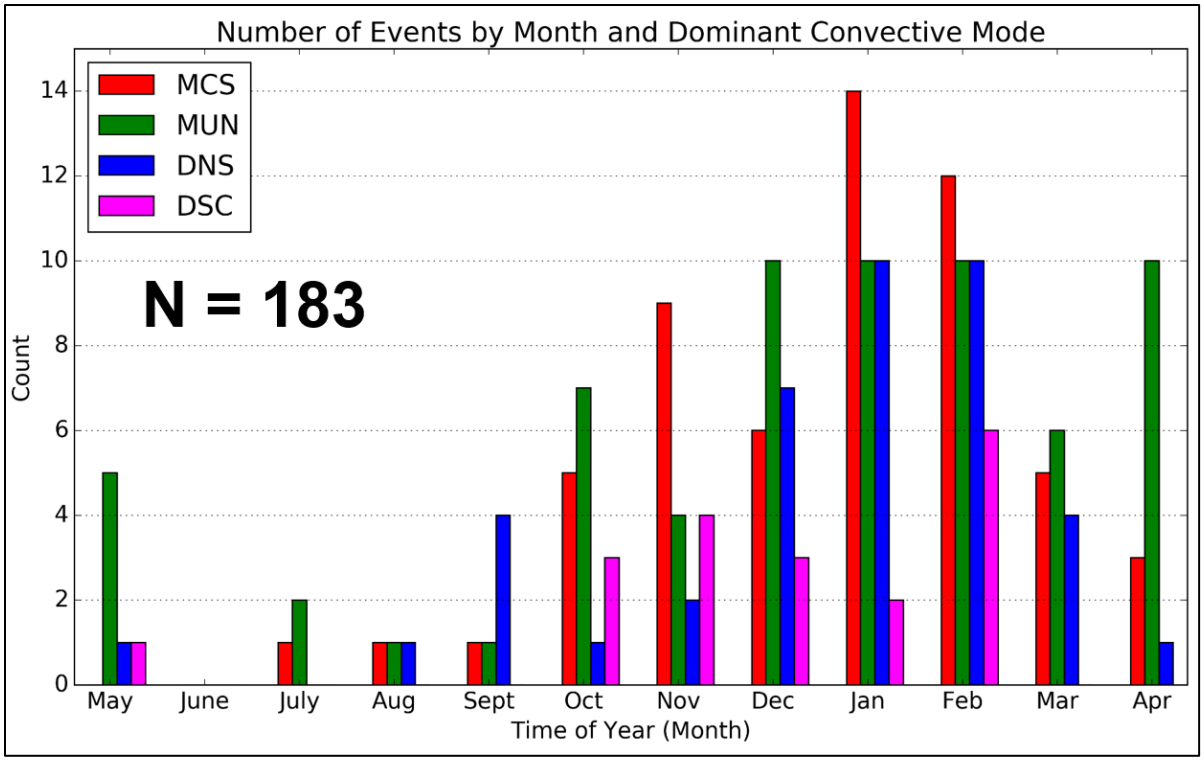

Figure 3.5: As in Fig. 3.4, but by dominant convective mode: MCS, MUN, DNS, and DSC.

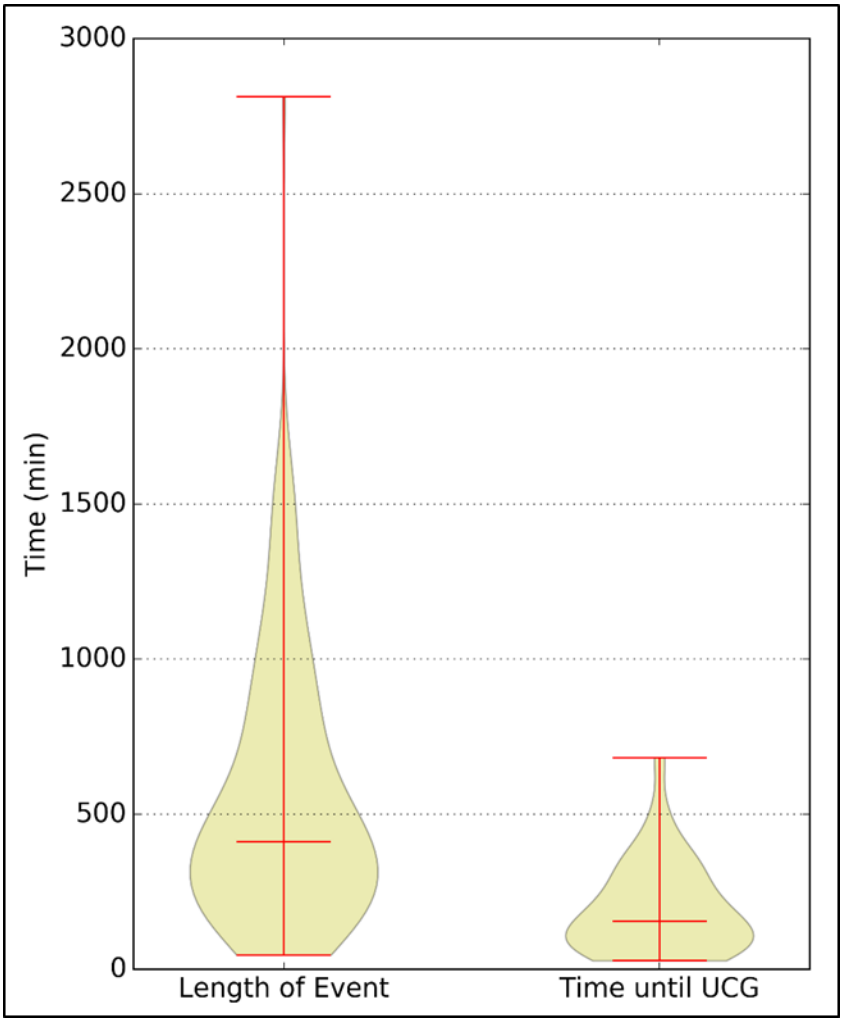

Figure 3.6: Violin box plots of length of event and time from CI until upscale convective growth (UCG; both in minutes).

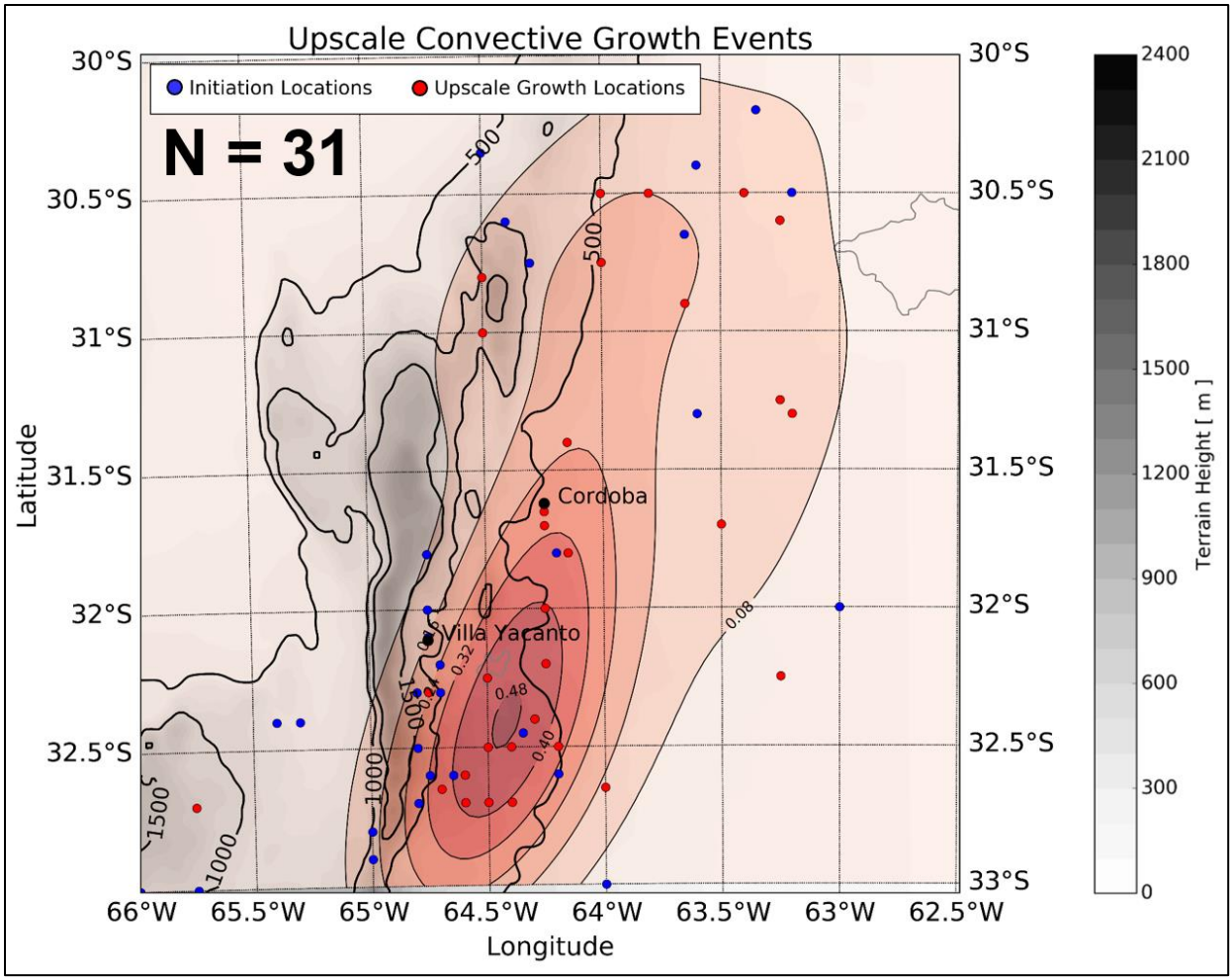

Figure 3.7: Spatial distribution of all CI locations (blue dots) and upscale convective growth locations (red dots). A kernel density estimation (KDE; using Scott's Rule; Scott 1992) of the upscale convective growth locations is denoted by red shades. The cities of Córdoba and Villa Yacanto are labeled in black. Terrain contours of 500, 1000, and 1500 m are outlined in thick black lines and terrain height is shaded in grey (m).

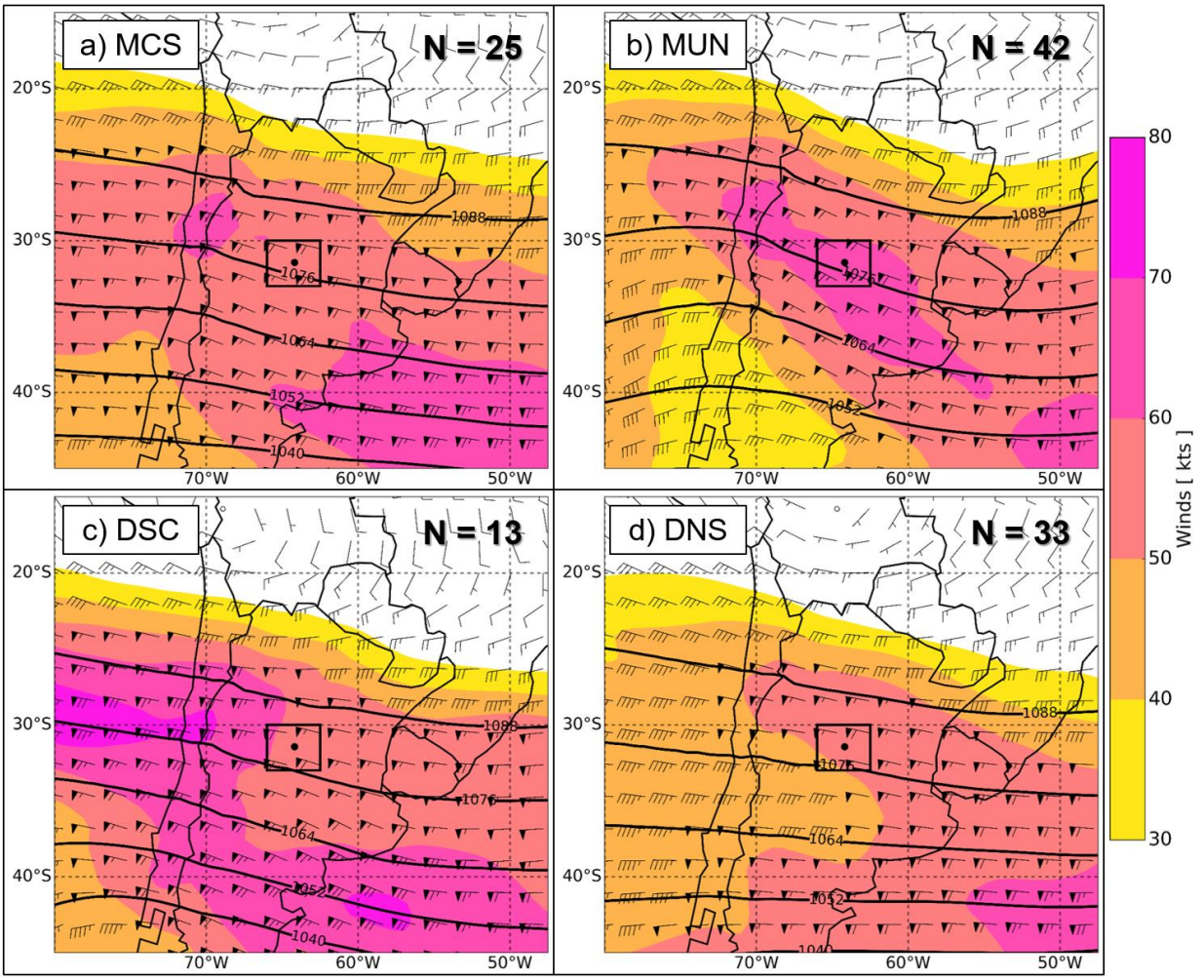

Figure 3.8: ERA-Interim composite mean 250 hPa wind speed (shaded; kt), geopotential height (contoured in black every 12 dam), and wind barbs (half barb = 5 kt; full barb = 10 kt; pennant = 50 kt) for: a) MCS, b) MUN, c) DSC, and d) DNS convective modes. The black square located in the center of each panel is the Córdoba radar tracking domain and the black dot is the city of Córdoba.

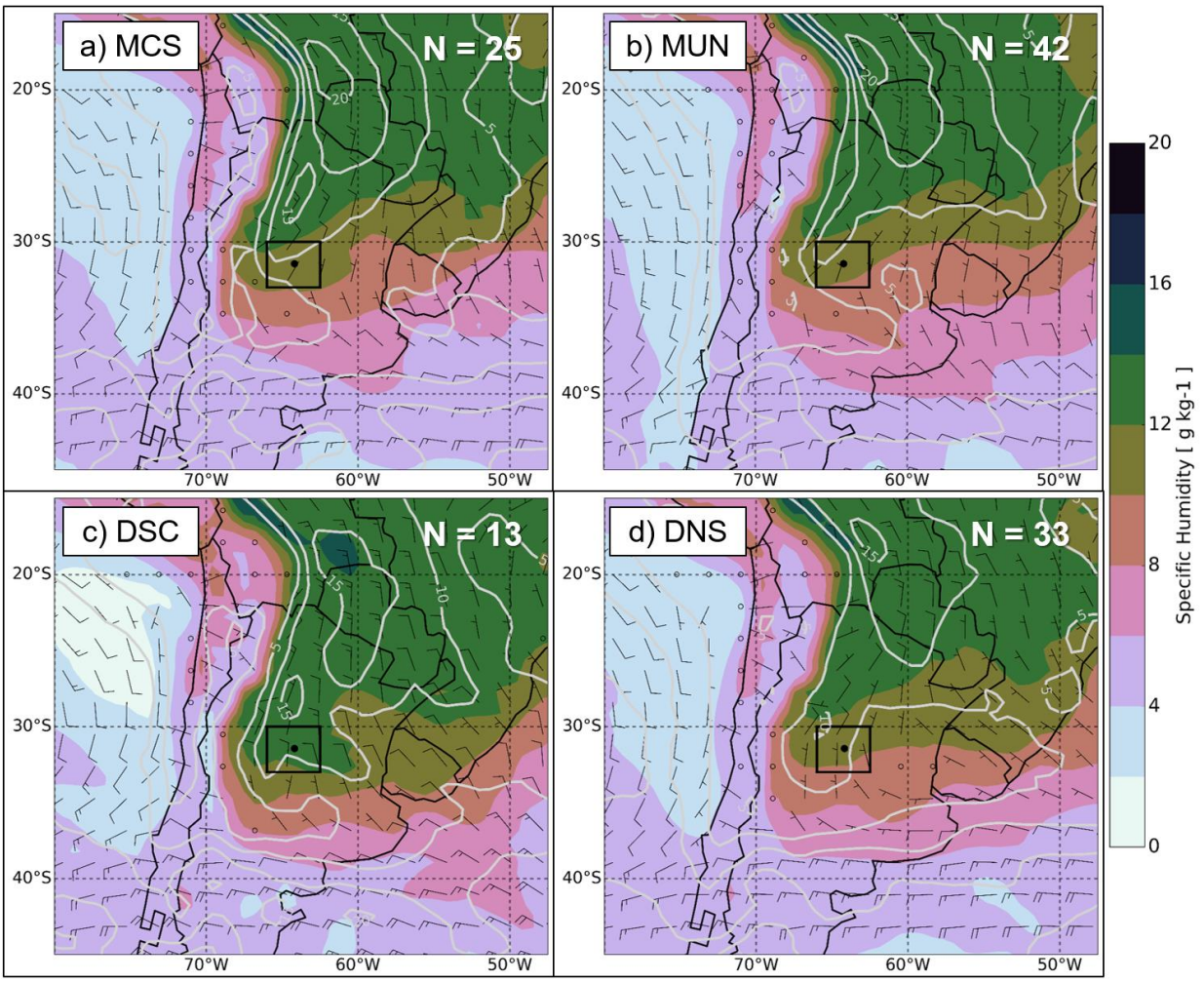

Figure 3.9: Same as in Fig. 3.8, but for 850 hPa specific humidity (shaded; g kg^{-1}), isotachs (grey contours every 5 kt), and wind barbs (half barb = 5 kt; full barb = 10 kt; pennant = 50 kt).

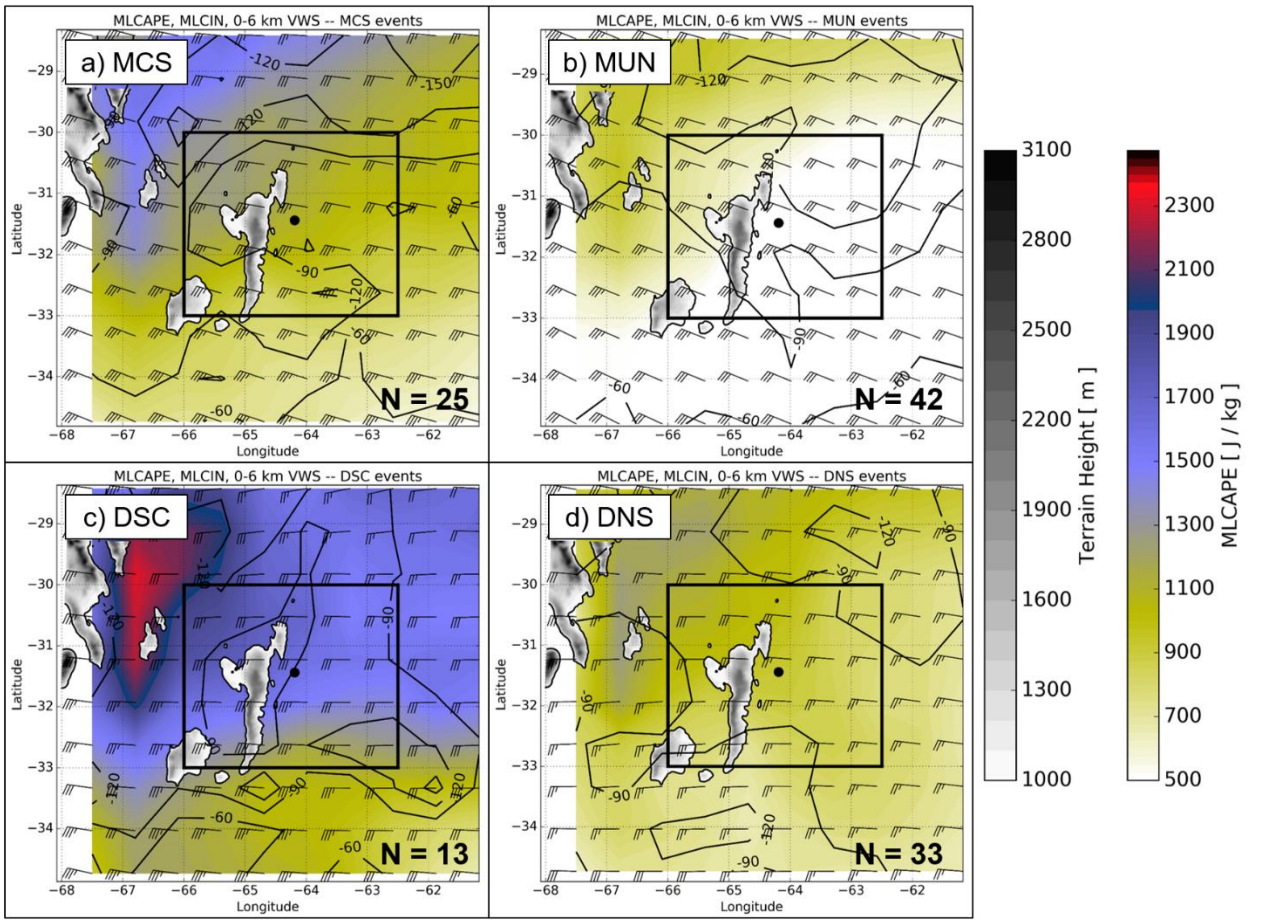

Figure 3.10: ERA-Interim composite mean mixed-layer convective available potential energy (shaded; J kg^{-1}), terrain height (shaded in grey; m), mixed-layer convective inhibition (contoured in black every 30 J kg^{-1}), and 0–6 km AGL vertical wind shear (barbs; half barb = 5 kt; full barb = 10 kt; pennant = 50 kt) for: a) MCS, b) MUN, c) DSC, and d) DNS convective modes. Elevation above 1000 m is shaded in grey and the square black box located in the center of each panel is the Córdoba radar tracking domain.

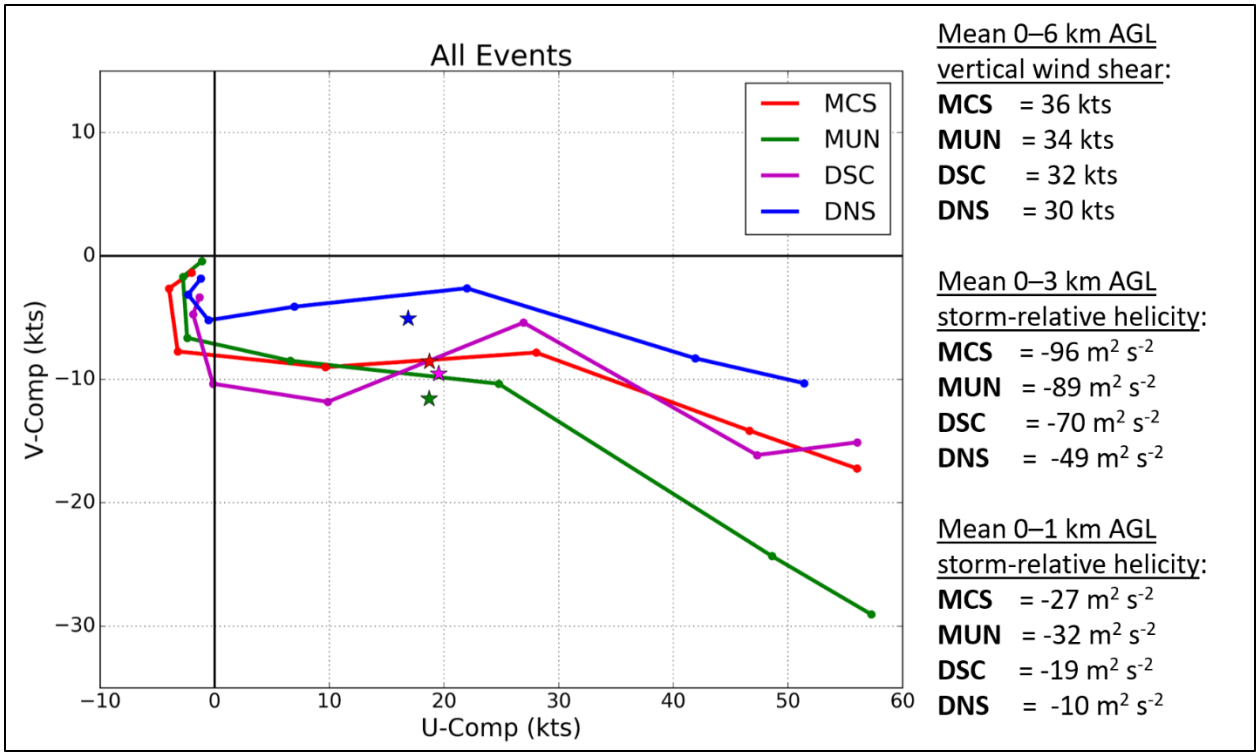

Figure 3.11: ERA-Interim composite mean wind hodographs for: MCS, MUN, DNS, and DSC convective modes. The *x*-axis is the *u*-component of the wind (kt) and the *y*-axis is the *v*-component of the wind (kt). Dots represent the following pressure levels: 1000, 925, 850, 700, 500, 300, and 250 hPa. Average storm motions, calculated using the mean wind between 1000–250 hPa, are labeled with stars. On the right: 0–6 km AGL mean wind shear (top; kt), 0–3 km AGL storm-relative helicity (middle; m^2 s^{-2}), and 0–1 km AGL storm-relative helicity (bottom; m^2 s^{-2}) magnitudes for the four different dominant convective modes.

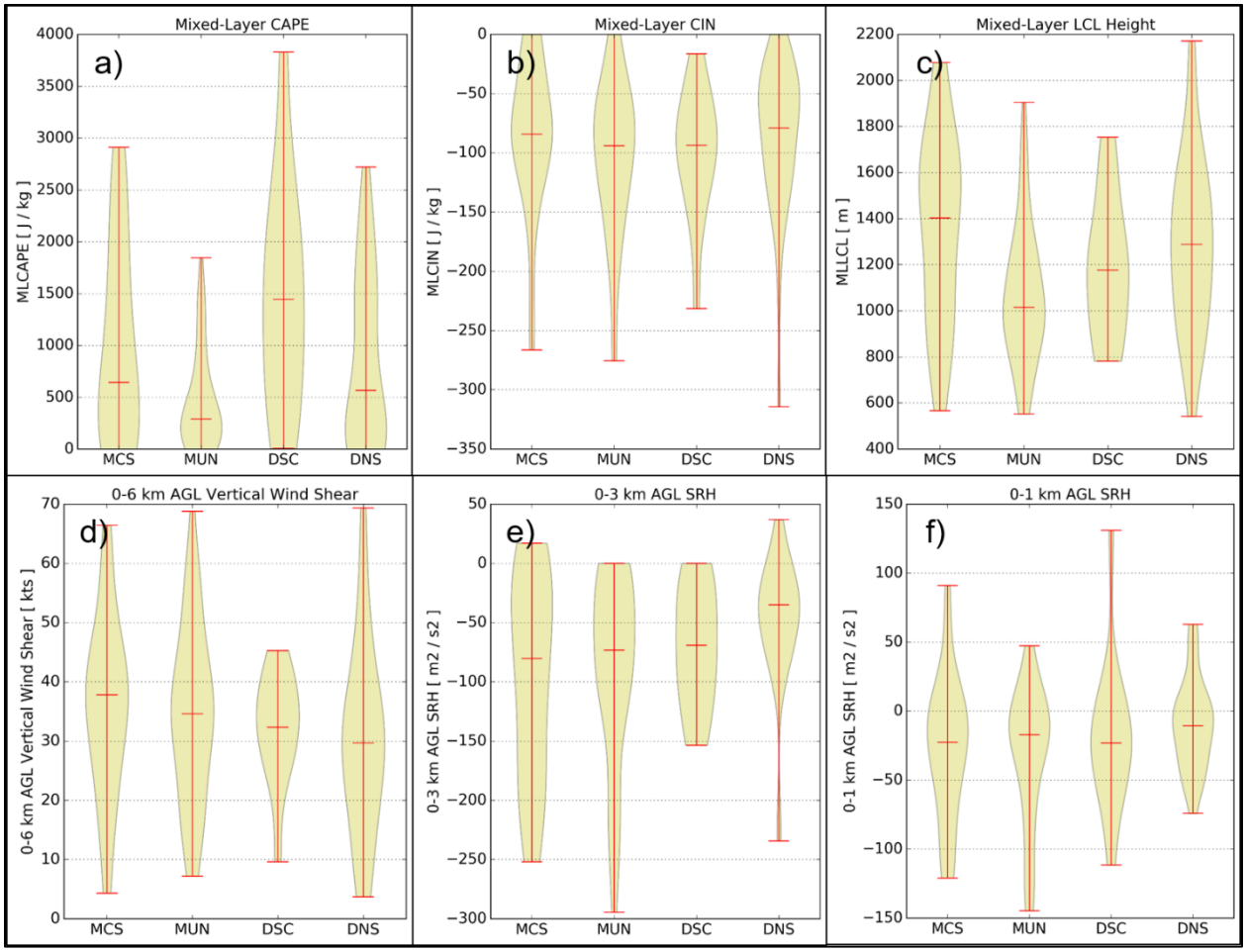

Figure 3.12: ERA-Interim composite mean violin box plots averaged over a 3˚ x 3.5˚ (30˚ to 33˚S and 62.5˚ to 66˚W) domain for: a) mixed-layer convective available potential energy (CAPE; J kg^{-1}), b) mixed-layer convective inhibition (CIN; J kg^{-1}), c) mixed-layer lifting condensation level height (LCL; m), d) 0–6 km AGL wind shear (kt), e) 0–3 km AGL storm relative helicity (SRH; m^2 s^{-2}), and f) 0–1 km AGL storm relative helicity (SRH; m^2 s^{-2}).

CHAPTER 4: UPSCALE CONVECTIVE GROWTH CASE STUDY: 29 NOVEMBER 2017

4.1 Overview of the 29 November 2017 Event

4.1.1 Synoptic and Convective-Environment Overview

The 1200 UTC 250 hPa 12 h forecast from the 3 km CTRL-0 simulation (which closely matched observations) depicted a >50 m s^{-1} cyclonically-curved jet streak with a terminus across the northern SDC (Fig. 4.1a). This jet streak was accompanied by an amplified upstream shortwave trough (Fig. 4.1a). Large-scale height falls to the east of the upper-level trough induced low-level lee troughing across the SDC region, resulting in a northerly LLJ (commonly called the South American LLJ; SALLJ; e.g., Vera et al. 2006) with horizontal wind speeds of ≥10 m s^{-1} (Fig. 4.1b). As a result of the SALLJ, abundant horizontal moisture advection, with specific humidity values of ≥10 g kg^{-1}, was commonplace across and east of the SDC (Fig. 4.1b). A northwest-to-southeast oriented convergence boundary was located south of the SDC (thick black dashed line in Fig. 4.1b) which corresponded to a surface cold front (not shown). Visible satellite imagery revealed that an MCS was ongoing along the cold front at 1530 UTC south of the region with mountain waves across the southern SDC near the CI location (not shown).

The local convective environment owing to this synoptic pattern was well represented by the 1200 UTC Córdoba sounding, which showed a near-surface air temperature and dewpoint temperature of 22°C and 15°C, respectively (which closely matched the model sounding from the 1 km CTRL-0 simulation; Fig. 4.2). A relatively deep moist layer extended vertically to ~650 hPa, where a temperature inversion and hydrolapse were located associated with the base of an elevated mixed layer, a common feature east of the Andes Mountains (e.g., Ribeiro and Bosart 2018); the most-unstable CIN, however, was minimal (> -50 J kg^{-1}; Fig. 4.3a). This elevated mixed layer was

characterized by steep midlevel lapse rates (600–450 hPa lapse rates of ~8.2°C km^{-1}), which contributed to most-unstable CAPE of ~800–1200 J kg^{-1} (Fig. 4.3a). The LLJ was also apparent in the sounding, evidenced by 10–15 m s^{-1} horizontal wind speeds between 925–700 hPa (Fig. 4.2). This contributed to deep-layer wind shear of ~20–25 m s^{-1} over the 0–6 km AGL layer (Fig. 4.3a) and counterclockwise-curving low-level hodographs, with 0-2 km SRH between -200 to -300 m^2 s^{-2} (Fig. 4.3b).

4.1.2 Convective Mode Evolution

As shown by the RMA1 radar data, isolated DMC initiated across, and just east of, the southern SDC at ~1742 UTC (Fig. 4.4a). Given a favorable environment (Fig. 4.3), these initial cells quickly developed into a left moving supercell by ~1914 UTC just southwest of Córdoba (Fig. 4.4c). Shortly thereafter, the supercell began to grow upscale into an MCS and by ~2136 UTC the system began to bow outward (to the north) as the frontal MCS to the south began to overtake the initial MCS (Fig. 4.4f). Given the relatively deep (~2 km) well mixed boundary layer extending from the surface-to-700 hPa ("inverted-V" profile; Fig. 4.3b), the potential for strong downdrafts was apparent. The observed time from CI to UCG according to the RMA1 radar was ~4 h. This event was associated with social media (Twitter) reports of "orange-sized" hail, straight-line wind gusts of ~20 m s^{-1} and flooding near Córdoba.

4.2 Results

4.2.1 333 m CTRL-0 Simulation

Analyses of simulated radar reflectivity at the lowest model level from the 333 m CTRL-0 experiment revealed that CI, owing to convergent anabatic upslope flows, occurred in nearly the same location and slightly earlier (~1700 UTC) compared to the observed radar reflectivity (Figs. 4.4a and 4.5a). A storm split was depicted in the simulation starting ~1914 UTC (Fig. 4.5c) and

continued through ~1956 UTC (Fig. 4.5d; not seen in radar observations) before a dominant left moving simulated supercell became established by ~2027 UTC. By 2100 UTC, surging outflow along the rear-flank gust front region of the supercell began to undercut the mesocyclone (not shown) and the storm transitioned into a bowing MCS (Fig. 4.5f). This storm evolution was similar to that shown in the observed radar data; however, the simulation was too slow in depicting the trailing frontal MCS overtaking the initial supercell (Figs. 4.4f and 4.5f). While the simulation was slightly delayed compared to the observations, the overall salient features of convective morphology were remarkably comparable between the simulation and observations, allowing for further examination of the model output.

The mesoscale environment during the UCG phase was characterized by increasing MUCAPE (1200–1600 J kg^{-1}) with negligible MUCIN (> -50 J kg^{-1}) along the western flanks of the simulated supercell (Fig. 4.6, top row). Furthermore, the low-level SRH within the inflow and rear-flank gust front regions of the simulated supercell rapidly increased along a narrow corridor to the east of the SDC, with magnitudes < -500 m^2 s^{-2} (Fig. 4.6, bottom row). The combination of increasing low-level wind shear, increasing MUCAPE, and decreasing MUCIN created an environment favorable for the rapid UCG of this orographic supercell.

An analysis of the low-level cold pool during this period revealed that following the storm split ~1914 UTC, the magnitude and areal extent of the cold pool increased markedly, especially for the left moving supercell (Fig. 4.7). This cold pool growth and intensification was located mainly along the rear-flank gust front region of the simulated supercell, similar to the supercell-to-MCS transition case study presented by Finley et al. (2001). North-to-south vertical cross-sections through the coldest portion of the cold pool revealed an increase in the depth and strength of the cold pool from CI time through the UCG stage (Fig. 4.7; top row). Favorable orientation of

the mean lower-tropospheric winds (Fig. 4.7, bottom row) directed nearly opposite to that of the cold pool (and storm) motion resulted in robust lifting (≥5 m s^{-1}; Fig. 4.7, top row) along the surging outflow boundary, triggering additional convective development and shortly thereafter, rapid UCG (e.g., Wilson et al. 1988). The surging outflow caused the lower portions of the mesocyclone to be cut-off from the warm and modestly moist (e.g., lowest 100 hPa mixing ratios ~10–12 g kg^{-1}; Fig. 4.1b) inflowing boundary layer air from the north and east, with new updraft growth that became increasingly tilted and displaced rearward, farther behind the surface outflow boundary (e.g., Fig. 4.7e).

4.2.2 Terrain Modification Experiments

To understand the effects that the complex terrain of the SDC had on the UCG process of this supercell-to-MCS transition, an extra set of four terrain experiments were conducted, in addition to the CTRL-0 experiment. As described in section 2.7, the maximum terrain height of the SDC varied from ~3495 m in the HIGH-40 experiment to ~1000 m in the LOW-40 experiment. A direct effect that the increased terrain height of the SDC had on the convective morphology was an earlier CI time and slightly different CI locations along the SDC (Fig. 4.8; top row). In the HIGH-40 experiment, CI was ~1535 UTC, whereas in the LOW-40 experiment CI was ~1755 UTC with the CTRL-0 experiment in the middle (~1635 UTC). One explanation for the earlier CI time in the higher terrain experiments is that the increased terrain height of the SDC acted as an enhanced elevated heat source (relative to the cooler surrounding ambient air), which resulted in lower hydrostatic pressure compared to surrounding lower elevations. This lead to an enhanced horizontal pressure gradient force directed toward the higher terrain (not shown; see Geerts et al. 2008), with an increase in low-level upslope flow. Furthermore, a standing mountain wave was evident in higher terrain experiments (Fig. 2.6). This mountain wave, with an upward branch

located near the CI location (slightly east of the SDC) in the higher terrain experiments, had upward vertical velocities ~1–4 m s^{-1}. The higher terrain experiments had a lower LFC for parcels lifted from the surface (not shown), which, when combined with the enhanced vertical motions from the standing mountain wave and convergent upslope low-level flow, help explain the earlier CI in the diurnal cycle for these experiments (Figs. 2.6i, j). In the lower terrain experiments, this mountain wave was non-existent (Figs. 2.6f, g) and the LFC for parcels lifted from the surface was much higher in altitude (not shown). In terms of CI location, the higher terrain experiments had CI which occurred farther north, closer to the highest elevations in the SDC (near -31.75˚S, -64.75˚W).

Peak supercell stages (as defined previously in section 2.8) occurred at different times and different locations for the five terrain experiments (Fig. 4.8; middle row). All supercells had similar column peak upward vertical velocities (34–37 m s^{-1}); however, the higher terrain experiment supercells had slightly stronger column-peak downdrafts (-17.7 m s^{-1} in LOW-40 experiment and -23.2 m s^{-1} in HIGH-40 experiment; not shown). The average time from CI until peak supercell stage for each terrain experiment was generally similar (~3–4 h after CI; Table 4.1). The duration from peak supercell time until the beginning stages of UCG (as defined above), however, was quite different and was smallest for the CTRL-0 (40 min) and HIGH-25 (1 h 10 min) experiments as compared with the other terrain experiments (Table 4.1). In fact, the LOW-40 and LOW-25 terrain experiment supercells never underwent UCG as per the quantitative definition outlined in section 2.8. Instead, the trailing frontal MCS in these experiments was stronger and overtook the initial isolated supercell.

The indirect influences on storm morphology by changing the terrain height were associated with the environmental conditions near and surrounding the SDC. During CI stage,

higher terrain experiments displayed lower magnitudes of MUCAPE (Fig. 4.9). Magnitudes of MUCAPE at CI stage varied from ~1200–1600 J kg^{-1} in the LOW-40 experiment to ~600–1000 J kg^{-1} in the HIGH-40 experiment (Fig. 4.9; top row). This trend in MUCAPE was a result of a decrease in low-level mixing ratio in higher terrain experiments (not shown). During peak supercell stage, MUCAPE was generally similar across all experiments within the inflow regions of the supercells (Fig. 4.9; bottom row). MUCIN, however, was generally greater within the inflow region of LOW-40 and LOW-25 supercells with negligible MUCIN within the inflow regions of CTRL-0, HIGH-25, and HIGH-40 supercells (Fig. 4.9; bottom row). MUCIN increased in all terrain height experiments to the east, over the lower elevations.

The terrain alterations also resulted in changes to the low-level wind shear profile. In higher terrain experiments, 0–2 km SRH magnitudes tended to be greater within the inflow region of the developing supercells owing, at least in part, to the enhanced upslope flow component (Fig. 4.10; bottom row). The magnitudes of environmental (far field) SRH varied from -200 to -300 m^2 s^{-2} in the LOW-40 experiment to -350 to -450 m^2 s^{-2} in the HIGH-40 experiment. These results qualitatively resemble the idealized modeling studies conducted by Markowski and Dotzek (2011) and Soderholm et al. (2014) with respect to showing increased low-level wind shear downwind of high terrain. Furthermore, all terrain height experiments revealed a narrow ribbon of enhanced SRH along the eastern slopes of the SDC, owing presumably to horizontal vorticity associated with the thermally-forced upslope flow (e.g., Geerts et al. 2008). This supported supercell formation in all experiments; however, once the simulated storms moved eastward off the terrain, the low-level environments became increasingly less favorable for supercell sustenance (i.e., less favorable inflow SRH, higher inflow MUCIN). In summary, by increasing the terrain height of the SDC, a variety of environmental factors, both thermodynamic and dynamic, changed. MUCAPE

generally decreased and low-level SRH generally increased for higher terrain experiments (and vice versa for lower terrain experiments). This was mainly true within the nearest 25–50 km east of the altered terrain. Distances greater than 50 km from the altered terrain displayed generally similar environmental parameters across all five experiments.

During the peak supercell stage, the low-level cold pool was the strongest in the CTRL-0 and HIGH-25 experiments and weakest in the LOW-40, LOW-25, and HIGH-40 experiments (Fig. 4.11; Table 4.2). North-to-south vertical cross-sections through the coldest portion of the cold pools also revealed that the CTRL-0 and HIGH-25 experiments had the deepest cold pools compared with the other terrain experiments, with average cold pool depths of 2002 and 2129 m, respectively (Fig. 4.11, top row; Table 4.2). The trend for weaker and shallower cold pools in the HIGH-40 experiment likely owed to lower LCLs over the increased terrain height, which reduced the potential for subcloud evaporative cooling with incipient CI (e.g., Markowski and Dotzek 2011). The trend for weaker cold pools in LOW-25 and LOW-40 experiments likely owed to a greater number of moist air parcels that did not dry and warm following descent down the eastern slopes of the SDC, due to the lowered terrain height (see section 4c). This reduced the potential for any additional evaporative cooling. Droegemeier and Wilhelmson (1987) showed that cold pool depth was the most important cold pool property related to deep/intense gust front lifting and a corresponding higher potential for CI. Furthermore, the mean lower-tropospheric winds were directed nearly opposite to that of the cold pool (and storm) motion, which has been shown to support robust low-level lifting (Fig. 4.11, bottom row; e.g., Wilson et al. 1988). Indeed, in the CTRL-0 and HIGH-25 experiments, lower-tropospheric upward vertical velocities of 4–8 m s^{-1} were located along the outflow boundary, which were much greater than in the other terrain experiments (Fig. 4.11, top row). The stronger ascent along the outflow boundaries in these two

experiments coincided with negligible MUCIN, which allowed CI to occur more efficiently (see Figs. 4.9h, i). These two experiments also displayed the strongest downdrafts (-2 to -6 m s^{-1}) located behind the outflow boundary compared with the other simulations (Fig. 4.11, top row).

The initial deeper and stronger cold pools, and corresponding stronger upward/downward motions in the CTRL-0 and HIGH-25 experiments likely help, at least in part, explain the tendency for the quickest transition of this orographic supercell into an MCS relative to the other terrain experiments. Strong negative buoyancy was found within the rear-flank downdraft regions of the simulated supercells in these experiments. The subsequent surging outflow aided in additional CI along the gust front boundary, fostering more rapid UCG.

In the higher terrain experiments, the low-level cold pools tended to move northward with less penetration westward owing to terrain blocking of the negatively-buoyant air (Figs. 4.11i, j). In the lower terrain experiments, the low-level cold pools spread outward more efficiently with little terrain blocking of the negatively-buoyant air (Figs. 4.11f, g). In other terms, the low-level cold pool area during peak supercell stage was smallest in the HIGH-40 experiment and increased in areal extent through the LOW-25 experiment.

4.2.3 Trajectory Analyses

To further elucidate the thermodynamic cold pool properties of this supercell-to-MCS transition, parcel trajectories were computed within and outside the cold pools of the simulated storms at peak supercell stage. Offline trajectories were computed via second-order semi-implicit discretization in space and time using 1 min output from the 1 km domains (Miltenberger et al. 2013; Gowan and Steenburgh 2018). The initial locations of the parcels were defined in a *y*-*z* plane (8 columns, 60 rows for total number of parcels = 480 located at every model grid point) intersecting the coldest portion of the cold pool region of the simulated supercells. Various

thermodynamic quantities (e.g., RH, equivalent potential temperature) were computed along the parcel trajectory paths.

A comparison of the horizontal paths for parcels ending within the bottom (blue lines) and top (red lines) of the coldest portion of the cold pools (based on -0.1 m s^{-2} isoline) revealed that most of the air within the cold pools came from the inflow (eastern) side (Fig. 4.12). For the CTRL-0 and HIGH-25 experiments, however, some of the parcels that entered the top portion of the cold pool (red lines) originated over the higher terrain to the west (Figs. 4.12c, d). The strongest and deepest cold pool was associated with the HIGH-25 simulated supercell, which correspondingly had the greatest number of parcels originating over the higher terrain to the west and displayed the largest vertical displacements of parcels that entered the bottom of the cold pool (Fig. 4.13d). Parcels in the HIGH-25 experiment that originated from the higher terrain to the west experienced maximum downward vertical displacements of ~2500–3000 m with decreases in θ_e of 3–5 K. Given that θ_e is conserved for adiabatic and pseudoadiabatic processes, the decrease in θ_e toward the bottom of the cold pool indicates that diabatic processes were responsible (e.g., evaporation, melting). This is supported by the increase in rain and graupel mixing ratios along the parcel paths with relative humidity (RH) values <100%. The LOW-25, CTRL-0, and HIGH-40 experiment parcels all experienced similar θ_e decreases of 3–7 K as parcels approached the bottom of the cold pools with similar increases in both rain and hail mixing ratios with RH values <100% (Figs. 4.13b, c, e). CTRL-0 and HIGH-25 bottom of cold pool parcels had the lowest initial RH values (45–80%), which highlighted the potential for stronger evaporative cooling in these experiments (Figs. 4.13c, d). This potential was realized for these two experiments by virtue of displaying the strongest cold pools compared with the other terrain experiments. The LOW-40 experiment had the smallest vertical displacements (<500 m), smallest rain and hail mixing ratios (<2 g kg^{-1}), and

corresponding smallest changes in θ_e (<1 K) and RH (~30%) for parcels that approached the bottom of the cold pool, which helps explain why this simulated supercell had the weakest cold pool. The spread in θ_e, RH, and height for parcels entering the tops of the cold pools was greater compared with parcels entering the bottom of the cold pools, however, similar trends as described above were apparent (Fig. 4.14).

4.3 Summary and Conclusions

This chapter of the dissertation examined the role of terrain in the upscale growth process of an orographic supercell-to-MCS transition event. High-resolution WRF simulations were conducted in which the terrain height of the SDC was systematically raised or lowered. The terrain height experiments revealed direct and indirect influences on the convective evolution of this orographic supercell-to-MCS transition. Direct influences included terrain-related processes, such as terrain blocking of cold pools (e.g., in higher terrain experiments). Indirect influences included changes in the ambient environment owing to terrain alterations, such as, wind shear and CAPE variations, which then affected storm morphology. Higher terrain height experiments were characterized by stronger low-level wind shear and lower magnitudes of MUCAPE. CI was generally earlier in the higher terrain experiments and later in the lower terrain experiments relative to the control simulation. Even when the underlying terrain was effectively reduced to a plateau (e.g., LOW-40 experiment), a supercell formed. This supports the notion that the ambient environment was conducive for the formation of supercells, regardless of terrain heterogeneity. UCG into an MCS, however, only occurred when there was more substantial terrain height heterogeneity, with the “real” terrain configuration of the CTRL-0 experiment displaying the fastest UCG.

Parcel trajectories launched within the cold pools of the simulated supercells revealed that for the experiments with the strongest and deepest cold pools (CTRL-0 and HIGH-25 experiments), more air originated over the higher terrain to the west. The parcels that originated over the higher terrain were characterized by lower initial RH values, supportive of more enhanced potential diabatic microphysical cooling compared with parcels that originated over the lower terrain to the east. The complicated 3-D airflows in and around complex terrain revealed by the parcel trajectories need more investigation across many more events and supported by additional numerical modeling simulations.

While this study identified some important influences of terrain on the UCG process for this particular event, many more UCG events near complex terrain need to be examined. Questions remain that motivate Chapter's 5 contents on this subject, such as: (1) Does DMC initiated over terrain grow upscale faster or more readily than DMC initiated over flatter, more homogenous surfaces?, (2) What are the relative roles of direct (e.g., terrain blocking of cold pools) and indirect (e.g., terrain-induced variations in wind shear/CAPE) effects on UCG?, and (3) Is there an "optimal" terrain height that leads to the most rapid UCG by virtue of altering effectiveness of terrain blocking and/or relevant environmental parameters (e.g., depth of sheared layer, mixed-layer depth)? The copious observational data collected during both the *Remote sensing of Electrification, Lightning, and Mesoscale/microscale Processes with Adaptive Ground Observations* (RELAMPAGO; 2018) and *Cloud, Aerosol, and Complex Terrain Interactions* (CACTI; 2018-19) field experiments in north central Argentina, South America, will be leveraged in the future to help answer these outstanding questions. High-resolution idealized numerical modeling experiments shown in Chapter 5 are conducted to address these outstanding questions

by systematically varying terrain in a more controlled setting to analyze and further understand their effects on the UCG process.

4.4 Tables and Figures

	LOW-40	LOW-25	CTRL-0	HIGH-25	HIGH-40
Convection Initiation	17:55 UTC	17:35 UTC	16:35 UTC	15:15 UTC	15:35 UTC
Peak Supercell	21:30 UTC	22:30 UTC	20:35 UTC	19:50 UTC	19:30 UTC
Initial Upscale Convective Growth (UCG)	None	None	21:15 UTC	21:00 UTC	21:25 UTC
Δt (Supercell → UCG)	N/A	N/A	0 h 40 min	1 h 10 min	1 h 55 min

Table 4.1: Summary of the different stages of convective morphology by terrain experiment.

Terrain Experiment	Peak Magnitude of Cold Pool	Average Depth of -0.1 m s^{-2} Isoline
LOW-40	-0.124 m s^{-2}	826 m
LOW-25	-0.229 m s^{-2}	1091 m
CTRL-0	-0.301 m s^{-2}	2002 m
HIGH-25	-0.339 m s^{-2}	2129 m
HIGH-40	-0.265 m s^{-2}	1272 m

Table 4.2: Peak magnitude and average depth of cold pool (based upon -0.1 m s^{-2} isoline) during peak supercell stage.

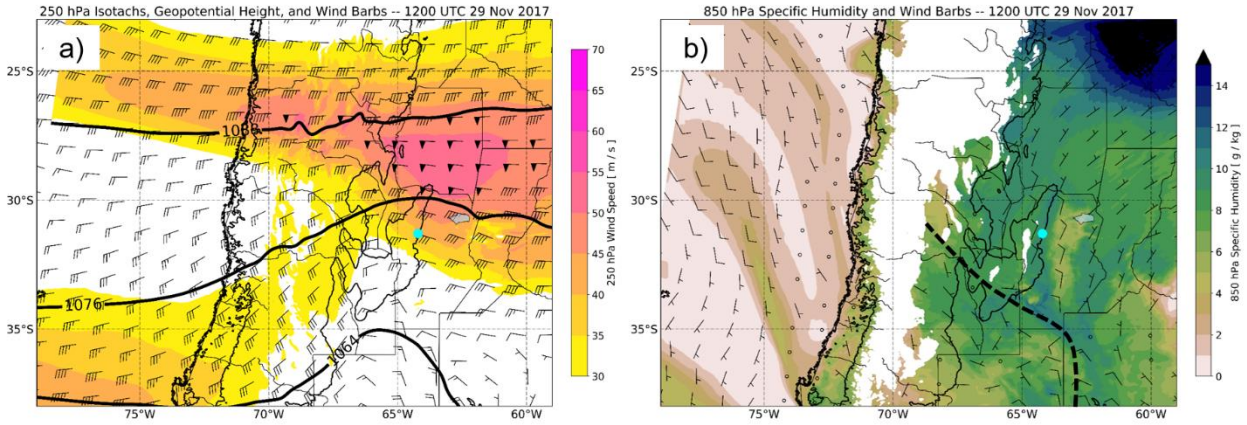

Figure 4.1: 3 km WRF output valid at 1200 UTC 29 November 2017 depicting: (a) 250 hPa isotachs (shaded; m s^{-1}), geopotential height (contoured in thick black lines every 12 dam), horizontal winds (half barb = 5 m s^{-1}, full barb = 10 m s^{-1}, pennant = 50 m s^{-1}), 500 m terrain height contour (thin black lines), Córdoba (cyan dot) and (b) 850 hPa specific humidity (shaded; g kg^{-1}), horizontal winds (half barb = 5 m s^{-1}, full barb = 10 m s^{-1}, pennant = 50 m s^{-1}), 500 m terrain height contour (thin black lines), and Córdoba (cyan dot). The thick dashed black line in (b) is the approximate location of a convergence boundary as discussed in the text.

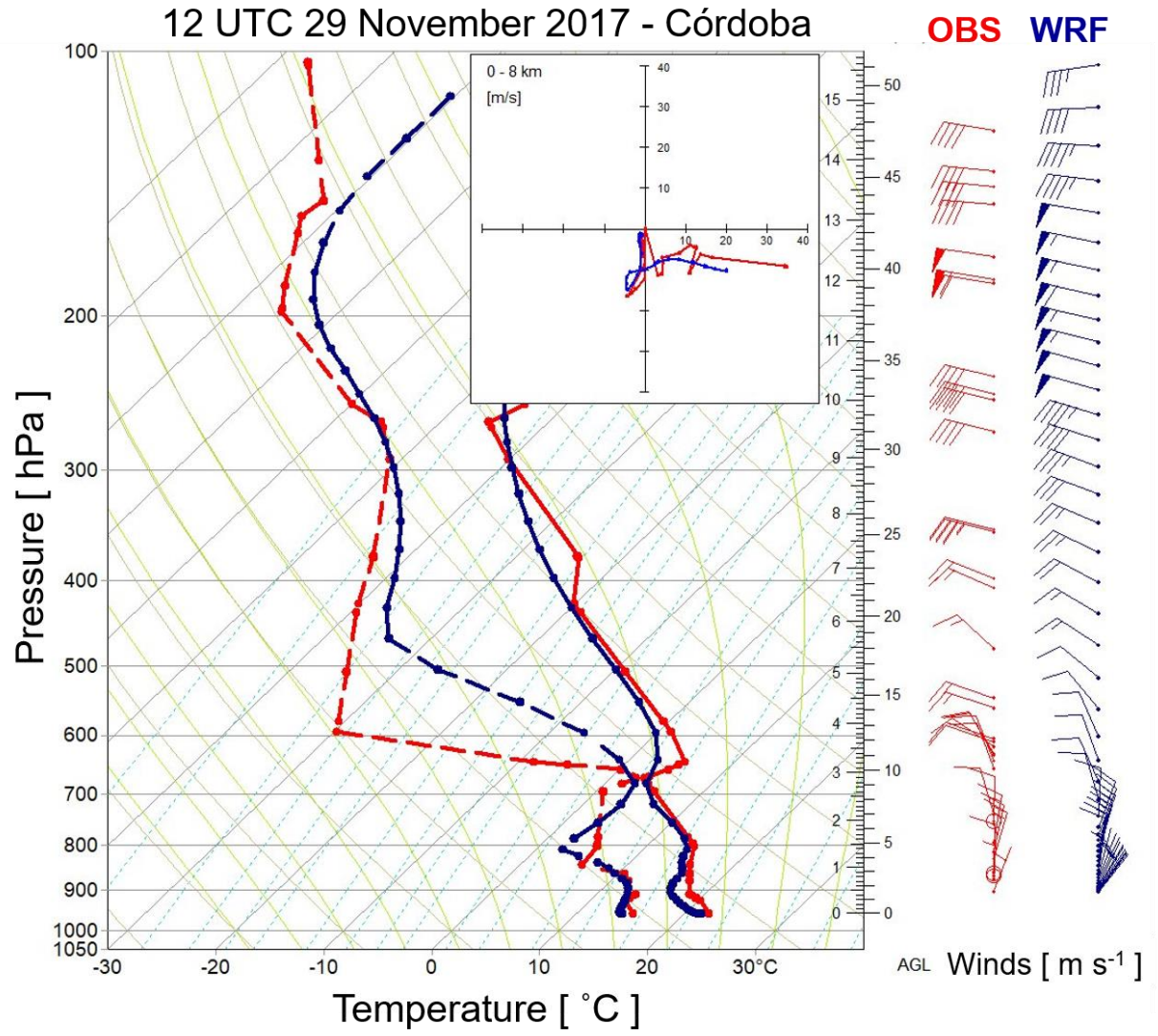

Figure 4.2: 1200 UTC 29 November 2017 Córdoba observed (red) and 1 km WRF-simulated (blue) upper-air sounding. The rightmost solid lines are temperature (˚C) and the leftmost dashed lines are dewpoint temperature (˚C). The inset figure is the wind hodograph trace from the surface through 8 km (m s^{-1}). Horizontal winds are plotted on the right (half barb = 5 m s^{-1}, full barb = 10 m s^{-1}, pennant = 50 m s^{-1}).

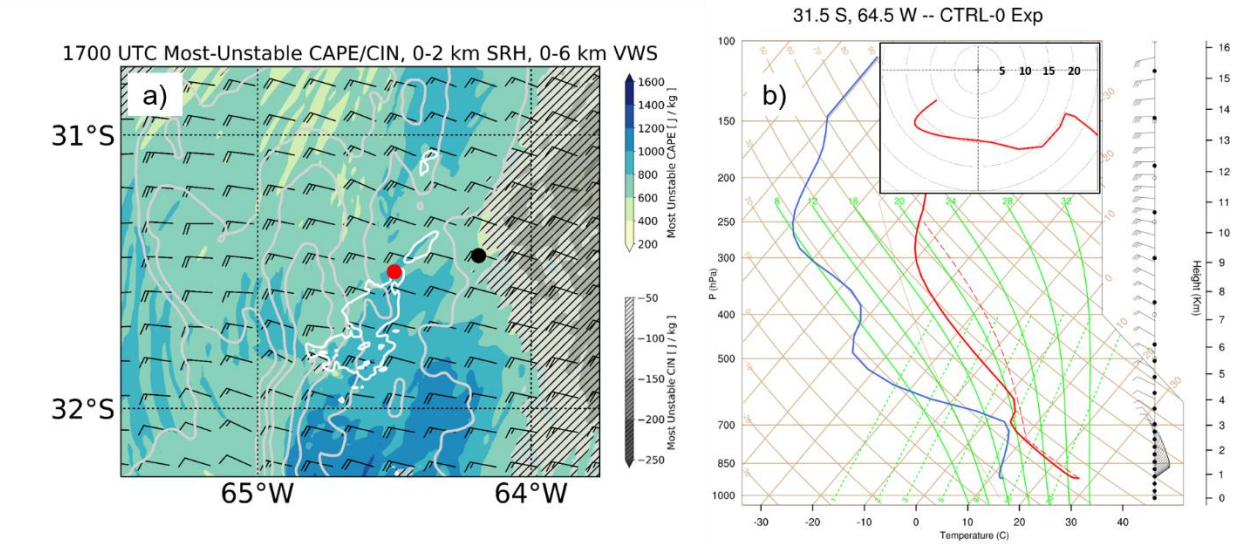

Figure 4.3: 1 km WRF output valid at 1700 UTC 29 November 2017 depicting: (a) most-unstable CAPE (shaded; J kg^{-1}), most-unstable CIN (shaded in grey; J kg^{-1}), 0-6 km AGL vertical wind shear (half barb = 5 m s^{-1}, full barb = 10 m s^{-1}, pennant = 50 m s^{-1}), 0-2 km AGL SRH (-200 and -300 m^2 s^{-2} contours in white), terrain height (contoured in grey every 500 m), Córdoba (black dot) and the location of the model sounding (red dot). In (b) point model sounding at red dot in (a). The solid red line is temperature (˚C), the solid blue line is dewpoint temperature (˚C), the dashed red line is the parcel trace for a parcel lifted from the surface, and horizontal winds (half barb = 5 m s^{-1}, full barb = 10 m s^{-1}, pennant = 50 m s^{-1}) are plotted at the right. The inset figure is a wind hodograph trace (red line; m s^{-1}).

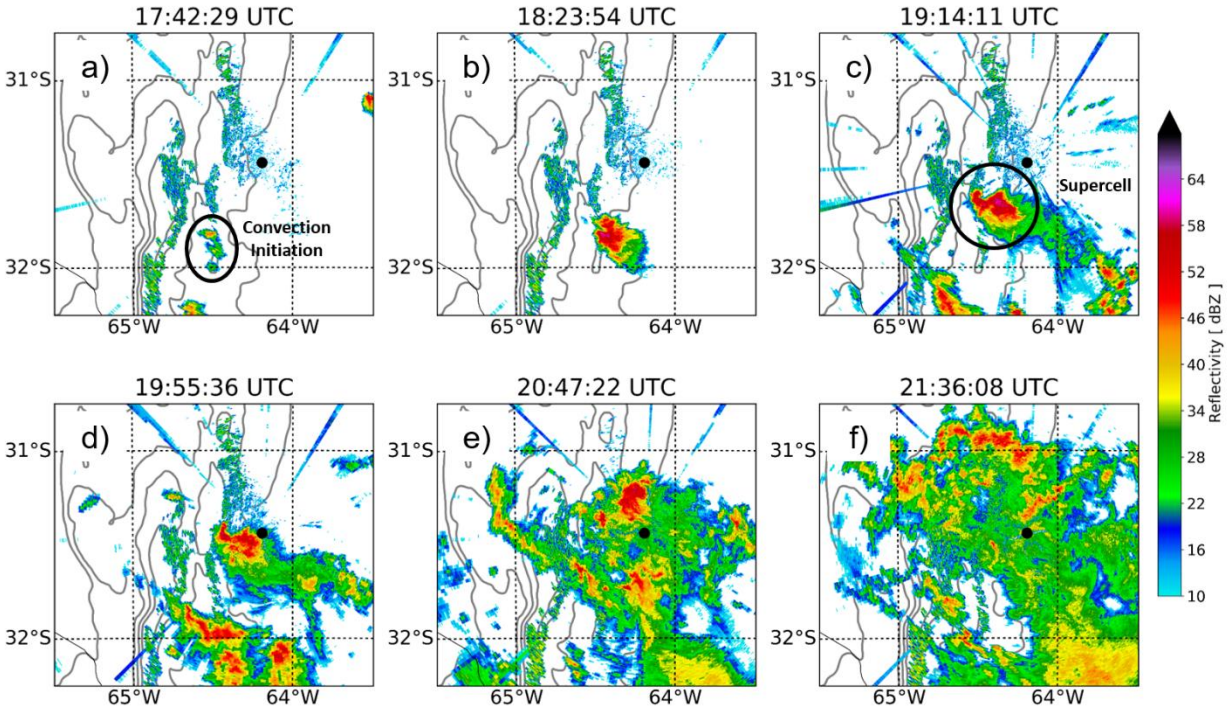

Figure 4.4: ~1˚ Córdoba C-band radar reflectivity (shaded; dBZ), terrain height (contoured in grey every 500 m), and Córdoba (black dot) valid at: (a) 17:42:29 UTC, (b) 18:23:54 UTC, (c) 19:14:11 UTC, (d) 19:55:36 UTC, (e) 20:47:22 UTC, and (f) 21:36:08 UTC.

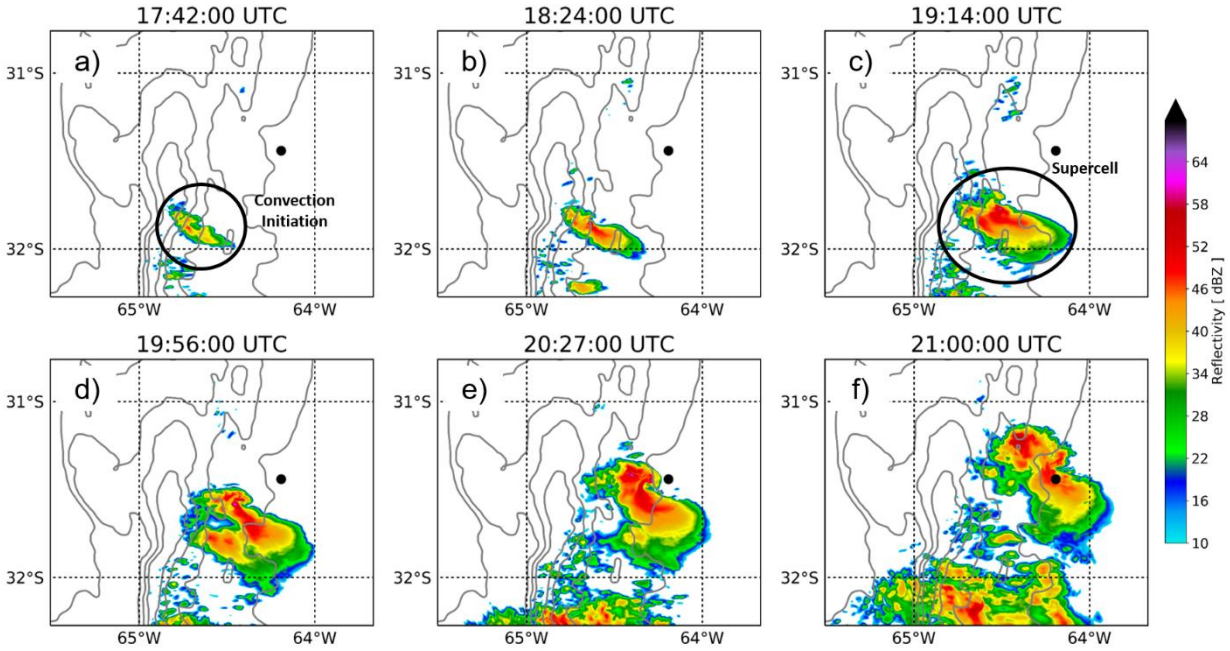

Figure 4.5: 333 m WRF-simulated lowest model-level radar reflectivity (shaded; dBZ), terrain height (contoured in grey every 500 m) and Córdoba (black dot) valid at: (a) 17:42:00 UTC, (b) 18:24:00 UTC, (c) 19:14:00 UTC, (d) 19:56:00 UTC, (e) 20:27:00 UTC, and (f) 21:00:00 UTC.

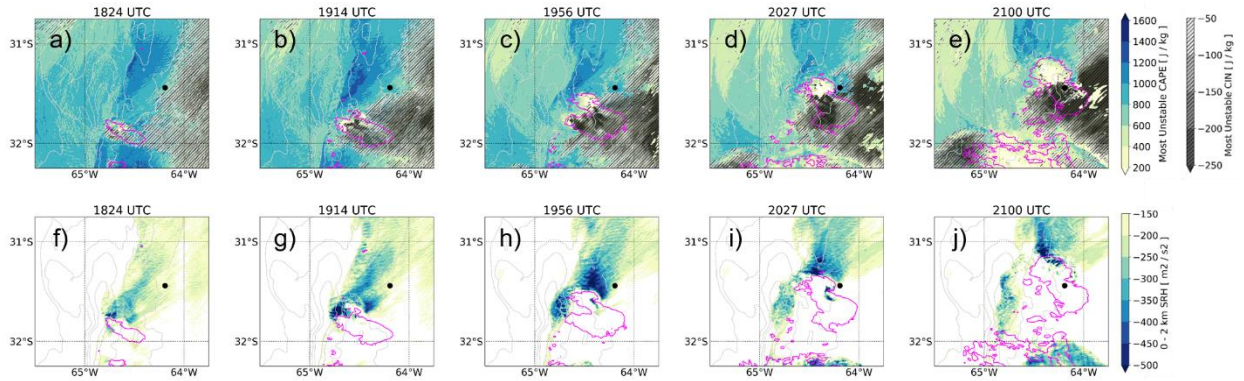

Figure 4.6: 333 m WRF output valid at: (a, f) 1824 UTC, (b, g) 1914 UTC, (c, h) 1956 UTC, (d, i) 2027 UTC, and (e, j) 2100 UTC. (top row) most-unstable CAPE (shaded; J kg^{-1}), most-unstable CIN (shaded in grey; J kg^{-1}), lowest model-level radar reflectivity (30 dBZ contour in magenta), terrain height (contoured in grey every 500 m), and Córdoba (black dot). (bottom row) 0-2 km AGL SRH (shaded below -150 m^2 s^{-2}), lowest model-level radar reflectivity (30 dBZ contour in magenta), terrain height (contoured in grey every 500 m), and Córdoba (black dot).

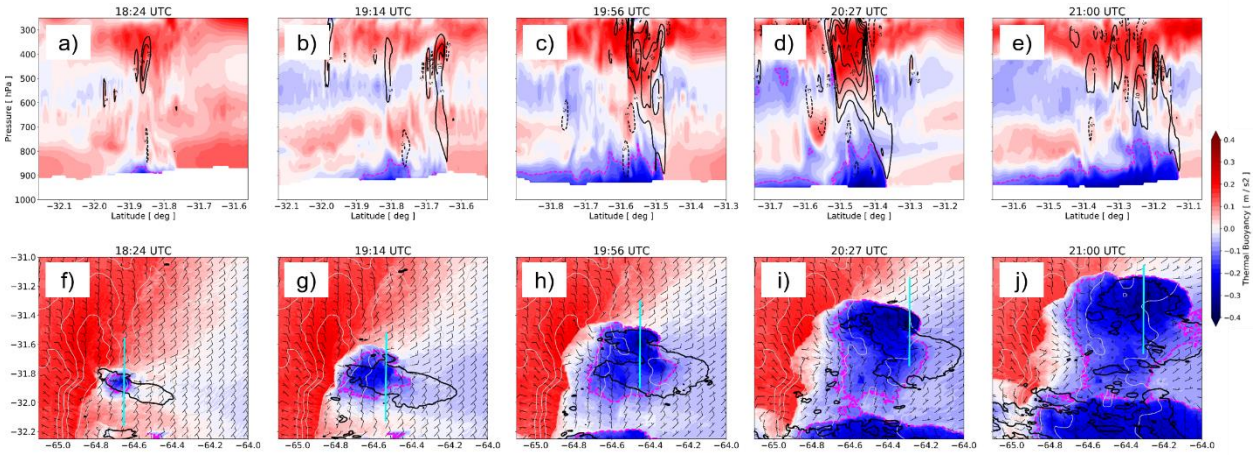

Figure 4.7: 333 m WRF output valid at: (a, f) 1824 UTC, (b, g) 1914 UTC, (c, h) 1956 UTC, (d, i) 2027 UTC, and (e, j) 2100 UTC. (top row) vertical cross sections (taken along cyan lines in bottom row) of thermal buoyancy (shaded; m s^{-2}), the -0.1 m s^{-2} isoline (dashed magenta contour), and vertical velocity (positive = solid black contours; negative = dashed black contours; m s^{-1}). (bottom row) plan views of thermal buoyancy (shaded; m s^{-2}), lowest model-level radar reflectivity (30 dBZ contour in black), the -0.1 m s^{-2} isoline (dashed magenta contour), terrain height (contoured in grey every 500 m), horizontal winds (averaged over σ = 0-10; half barb = 5 m s^{-1}, full barb = 10 m s^{-1}, pennant = 50 m s^{-1}), and the line along which the vertical cross sections in the top row were taken (cyan lines).

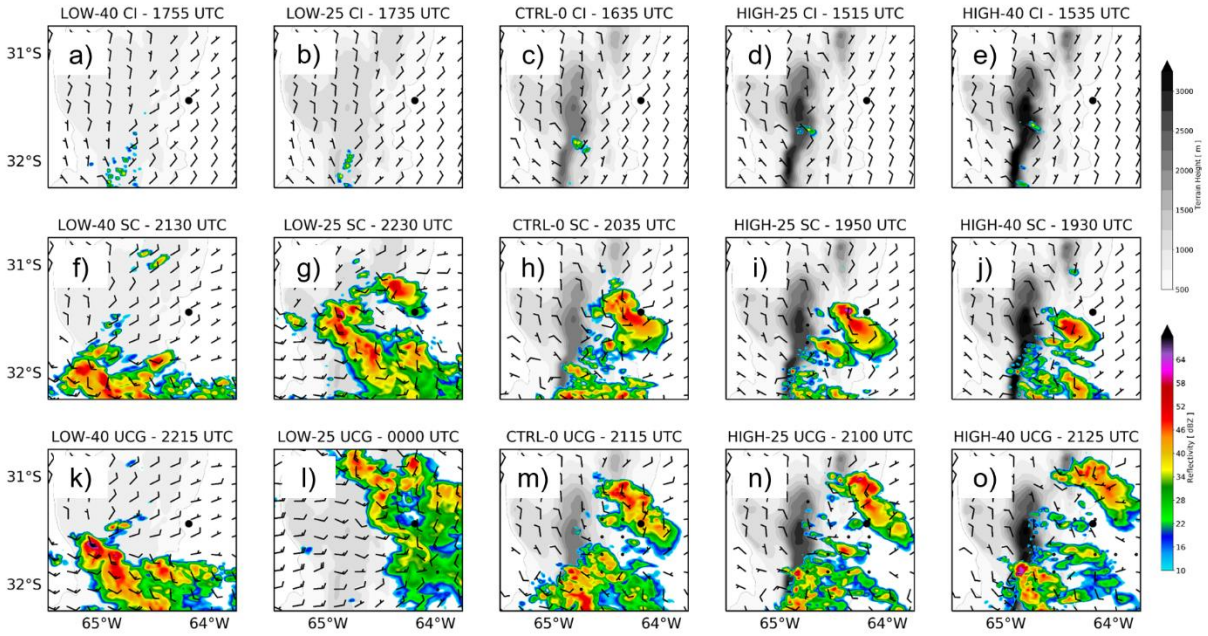

Figure 4.8: 1 km WRF terrain height experiment output. (top row) convection initiation stage, (middle row) peak supercell stage, and (bottom row) initial upscale convective growth stage depicting lowest model-level radar reflectivity (shaded; dBZ), terrain height (shaded in grey; m), horizontal winds (averaged over σ = 0-10; half barb = 5 m s^{-1}, full barb = 10 m s^{-1}, pennant = 50 m s^{-1}), and Córdoba (black dot). (a, f, k) LOW-40, (b, g, l) LOW-25, (c, h, m) CTRL-0, (d, i, n) HIGH-25, and (e, j, o) HIGH-40 experiments.

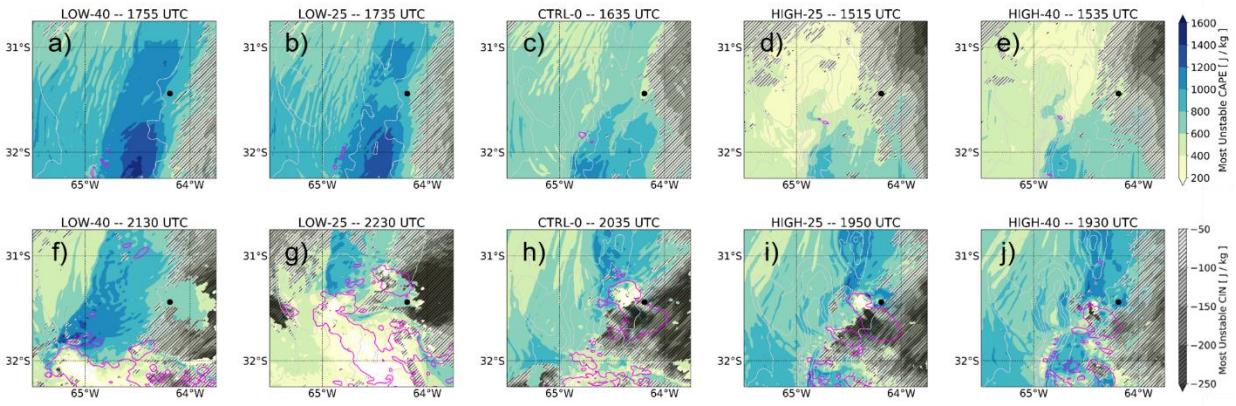

Figure 4.9: 1 km WRF terrain height experiment output. (top row) convection initiation stage and (bottom row) peak supercell stage depicting most-unstable CAPE (shaded; J kg^{-1}), most-unstable CIN (shaded in grey; J kg^{-1}), lowest model-level radar reflectivity (30 dBZ contour in magenta), terrain height (contoured in grey every 500 m), and Córdoba (black dot). (a, f) LOW-40, (b, g) LOW-25, (c, h) CTRL-0, (d, i) HIGH-25, and (e, j) HIGH-40 experiments.

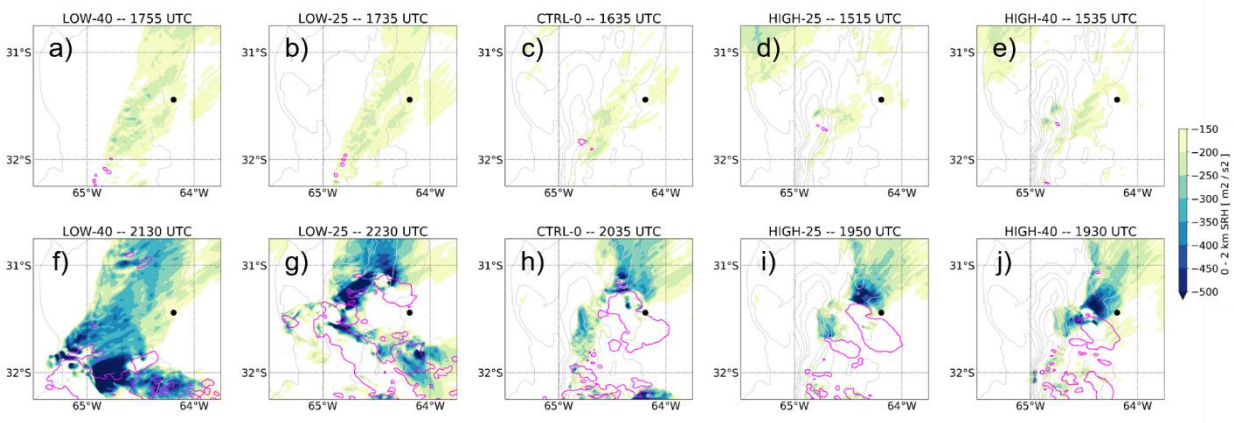

Figure 4.10: 1 km WRF terrain height experiment output. (top row) convection initiation stage and (bottom row) peak supercell stage depicting 0-2 km AGL SRH (shaded below -150 m^2 s^{-2}), lowest model-level radar reflectivity (30 dBZ contour in magenta), terrain height (contoured in grey every 500 m), and Córdoba (black dot). (a, f) LOW-40, (b, g) LOW-25, (c, h) CTRL-0, (d, i) HIGH-25, and (e, j) HIGH-40 experiments.

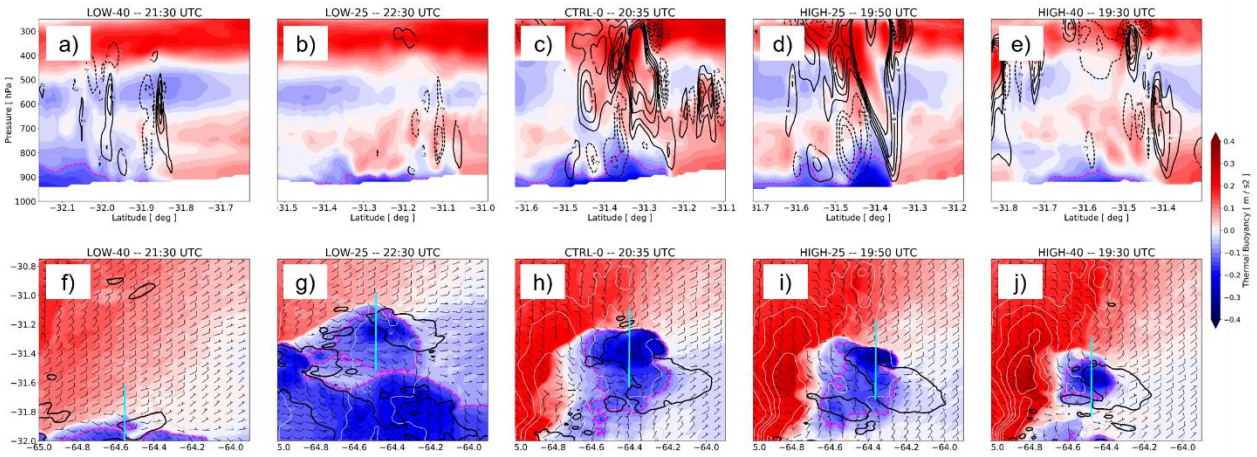

Figure 4.11: 1 km WRF terrain height experiment output at peak supercell stage. (top row) vertical cross sections (taken along cyan lines in bottom row) of thermal buoyancy (shaded; m s^{-2}), the -0.1 m s^{-2} isoline (dashed magenta contour), and vertical velocity (positive = solid black contours; negative = dashed black contours; m s^{-1}). (bottom row) plan views of thermal buoyancy (shaded; m s^{-2}), lowest model-level radar reflectivity (30 dBZ contour in black), the -0.1 m s^{-2} isoline (dashed magenta contour), terrain height (contoured in grey every 500 m), horizontal winds (averaged over σ = 0-10; half barb = 5 m s^{-1}, full barb = 10 m s^{-1}, pennant = 50 m s^{-1}), and the line along which the vertical cross sections in the top row were taken (cyan lines). (a, f) LOW-40, (b, g) LOW-25, (c, h) CTRL-0, (d, i) HIGH-25, and (e, j) HIGH-40 experiments.

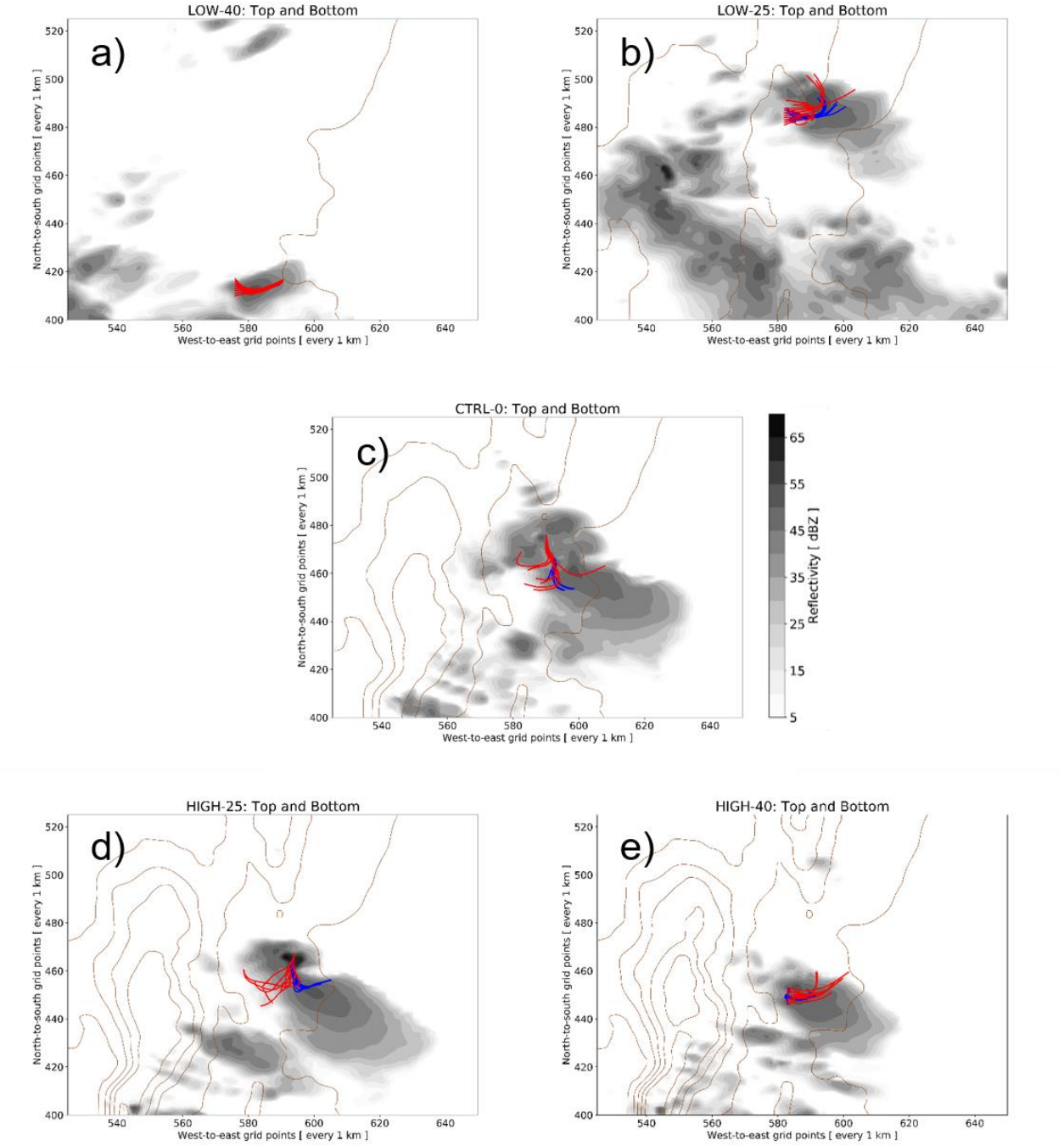

Figure 4.12: 1 km WRF terrain height experiment output at peak supercell stage depicting lowest model-level radar reflectivity (shaded; dBZ), terrain height (contoured in brown every 500 m), and backward parcel trajectory pathways for parcels ending at the bottom (blue lines) and top (red lines) of the simulated cold pools for: (a) LOW-40, (b) LOW-25, (c) CTRL-0, (d) HIGH-25, and (e) HIGH-40 experiments.

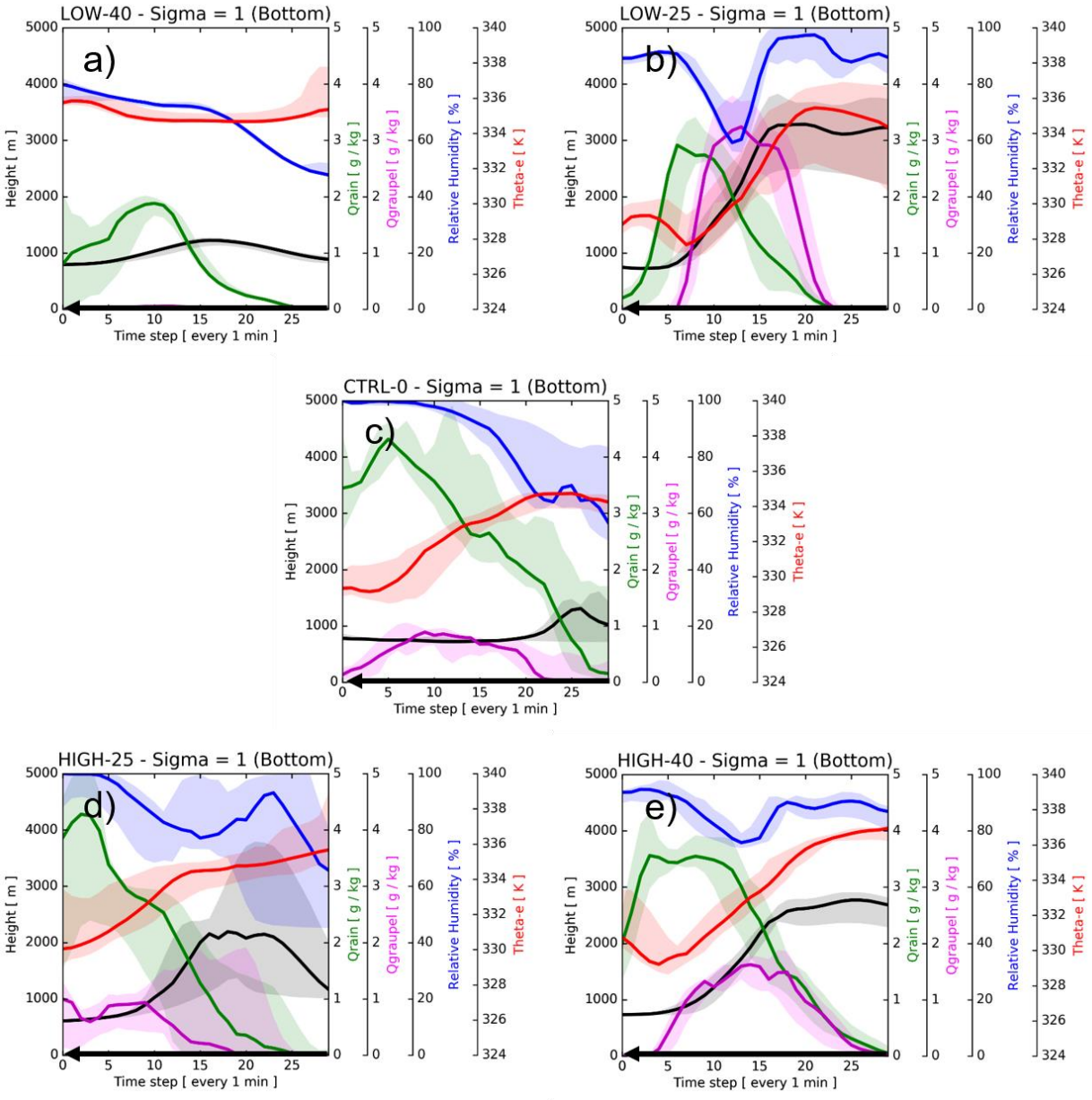

Figure 4.13: 1 km WRF terrain height experiment backward parcel trajectory time series for parcels ending within the bottom of the simulated cold pools at peak supercell stage. The black lines/shading denote height (m), green lines/shading denote rain water mixing ratio (g kg^{-1}), magenta lines/shading denote hail mixing ratio (g kg^{-1}), blue lines/shading denote relative humidity (%), and red lines/shading denote equivalent potential temperature (K) along the parcel pathways. Middle thick lines denote the median values and the shading represents the range between the max/min values of the quantities along parcel pathways. (a) LOW-40, (b) LOW-25, (c) CTRL-0, (d) HIGH-25, and (e) HIGH-40 experiments. Time increases from right-to-left in each panel.

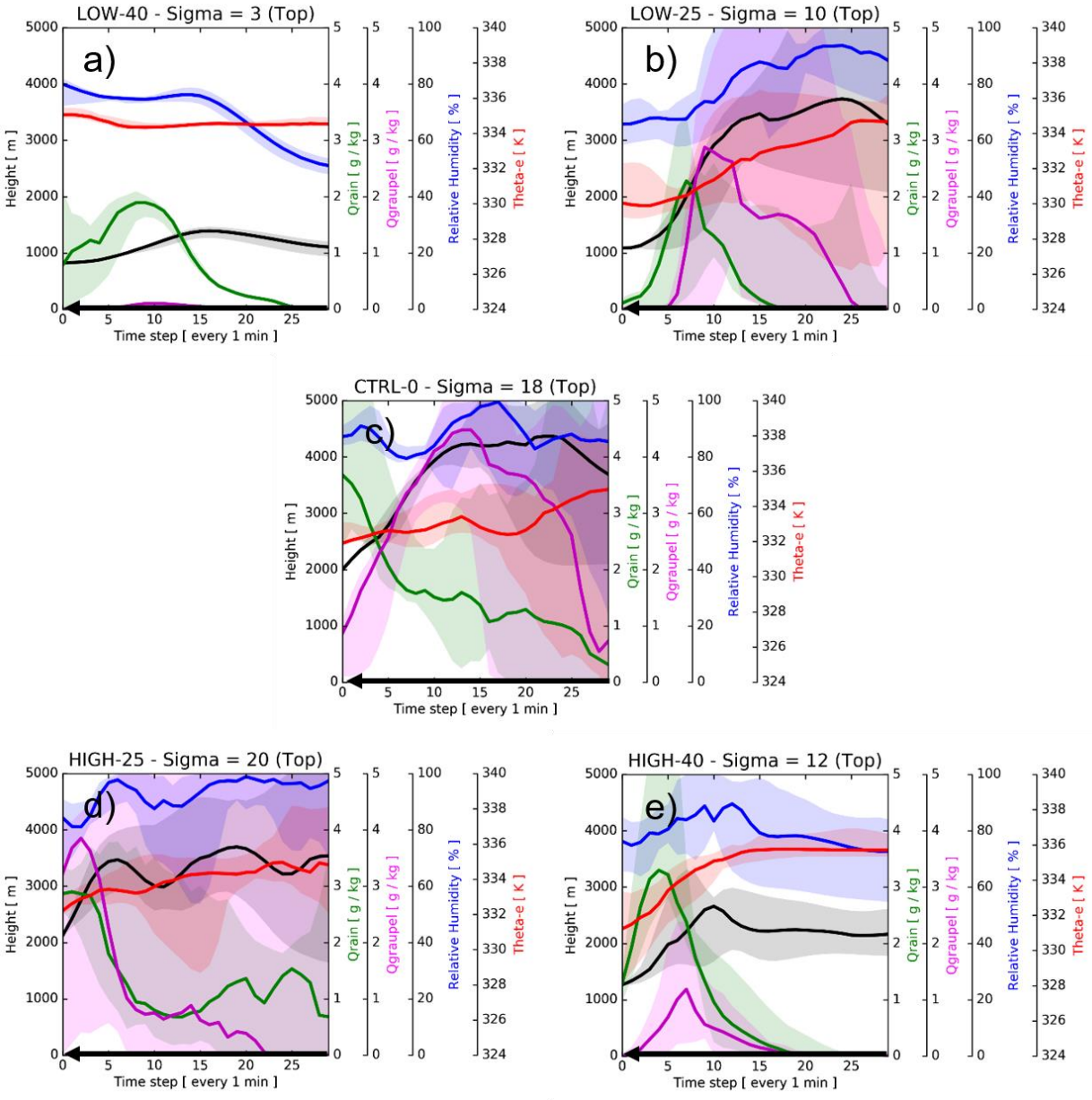

Figure 4.14: 1 km WRF terrain height experiment backward parcel trajectory time series for parcels ending within the top of the simulated cold pools at peak supercell stage. The black lines/shading denote height (m), green lines/shading denote rain water mixing ratio (g kg^{-1}), magenta lines/shading denote hail mixing ratio (g kg^{-1}), blue lines/shading denote relative humidity (%), and red lines/shading denote equivalent potential temperature (K) along the parcel pathways. Middle thick lines denote the median values and the shading represents the range between the max/min values of the quantities along parcel pathways. (a) LOW-40, (b) LOW-25, (c) CTRL-0, (d) HIGH-25, and (e) HIGH-40 experiments. Time increases from right-to-left in each panel.

CHAPTER 5: ON THE DIRECT AND INDIRECT INFLUENCES OF TERRAIN ON UPSCALE CONVECTIVE GROWTH OF OROGRAPHIC SUPERCELLS INTO MESOSCALE CONVECTIVE SYSTEMS

5.1 Results from Numerical Simulations

5.1.1 Convective Morphology

Peak supercell time for all terrain experiments occurred at nearly the same time, generally between 5–6 h into the simulations (except for the FLAT experiment; Table 5.1). Intriguingly, the higher-terrain experiments, which displayed generally earlier CI (Table 5.1), still reached peak supercell stage at nearly the same time as the lower-terrain experiments. Snapshots of lowest model-level reflectivity and 1–4 km AGL average vertical velocity at peak supercell time for each experiment revealed that the higher terrain supercells displayed a larger horizontal extent of reflectivity >35 dBZ, had wider updrafts, were more fixed to the higher terrain, were located farther south, and were more isolated in nature (Fig. 5.1). In the experiments with terrain lower than the control height of 2500 m, more widespread DMC was located near the main supercell, resulting in a mixed storm mode (Figs. 5.1a-d). Runtime accumulated 2–5 km AGL UH for each experiment revealed that the higher terrain supercells indeed had wider mesocyclones, displayed stronger and more coherent UH tracks, and had motions that deviated more to the right of the mean wind/shear than the lower terrain supercells (Fig. 5.2). Furthermore, the higher-terrain supercells traveled over a shorter eastward distance as compared with lower-terrain supercells and the FLAT supercell.

Time series of maximum 2–5 km AGL UH for each experiment showed a general monotonic increase in magnitude with increasing terrain height, further confirming that when terrain height was systematically raised, the simulated supercells were more intense (Fig. 5.3). Interestingly, the supercell mesocyclones in all experiments that grew into MCSs increased in

intensity leading up to just before UCG (Fig. 5.3 and Table 5.1). The rapid strengthening of a supercell's mesocyclone just prior to UCG has been noted before in a numerical modeling case study of a high-precipitation supercell that transitioned into a bowing MCS (Finley et al. 2001).

Leading up to UCG, the strongest and largest (time averaged) cold pool was associated with the 4500 m supercell, with generally weaker and smaller cold pools as the terrain was systematically lowered (Fig. 5.4). The total time from peak supercell stage to UCG stage was generally the smallest in the higher terrain experiments, with the 3500 m experiment displaying the most rapid transition (20 min; Table 5.1). The lower terrain experiments (2000 m and lower) depicted UCG via convective cell mergers and not by the single supercell growing upscale into an MCS. Thus, these experiments did not meet the specific UCG criteria outlined in section 2.10 and are not analyzed further. The exception was the FLAT experiment, which also did not undergo UCG as per the quantitative definition, but was compared with the higher terrain experiments in order to investigate the relative roles of direct versus indirect influences of terrain on UCG.

5.1.2 Updraft and Downdraft Characteristics

A trend toward stronger upward and downward supercell vertical velocities with increasing terrain was evident (Fig. 5.5). This trend was especially apparent for the extreme vertical velocity magnitudes (dot-dash lines in Fig. 5.5). The overall peak magnitude in both upward and downward vertical velocity was also found in the higher terrain supercells (Table 5.2). The intense vertical velocities in these simulations (frequently exceeding 80 m s^{-1}) were supported by ground-based C-band radar observations of the supercell on 25 January 2019 in north central Argentina, with recurrent instances of ≥40 dBZ radar reflectivity echoes extending above 17 km AGL in range-height indicator scans (e.g., Fig. 2.9b).

A quantification of updraft area, defined as contiguous grid points that exceeded a vertical velocity threshold of 10 m s^{-1} at various levels, revealed that higher-terrain supercell updrafts were wider than lower-terrain supercell updrafts (Fig. 5.6). The increase in supercell updraft width with increasing terrain height occurred over most of the troposphere, not just over one particular layer (Fig. 5.6). As a result of the stronger and wider supercell updrafts in the higher terrain experiments, larger magnitudes of upward vertical mass flux were manifest. Time-integrated upward vertical mass flux (regions where 2–5 km AGL UH ≥250 m^2 s^{-2}) leading up to the time of UCG at various levels revealed that higher terrain supercells displayed larger magnitudes with a monotonic increase with increasing terrain height (Fig. 5.7).

Owing to the wider/stronger updrafts and greater upward vertical mass flux in the higher terrain supercells, a greater horizontal extent of precipitation developed (Fig. 5.8). A further consequence of the stronger updrafts in the higher terrain supercells were stronger convective downdrafts (e.g., Fig. 5.5). The stronger updrafts were able to support larger hydrometeors, and thus, had a greater contribution to negative buoyancy via condensate loading (not shown). Time series of downdraft area, defined by the number of contiguous grid points where vertical velocity was ≤ -10 m s^{-1} at various levels, revealed that the higher terrain supercell downdrafts were also generally wider (Fig. 5.9). Overall, however, the downdraft area signal was less clear as compared to the updraft area with less of a monotonic increase in downdraft area with increasing terrain height.

The wider and stronger updrafts, along with the stronger and generally wider downdrafts in the higher terrain supercells, led to generally stronger cold pools (Table 5.3). Minimum near-surface potential temperature perturbations showed a general increase in (absolute) magnitude when terrain was raised from the 2500 m-CTRL experiment to the 4500 m experiment. The

(absolute) maximum in the near-surface potential temperature perturbation for each individual experiment (Table 5.3) matched well with the rate of UCG (Table 5.1). For example, the 3500 m experiment displayed the most negative near-surface potential temperature perturbation and a resultant fastest UCG rate of 20 min.

5.1.3 Indirect Influences of Terrain on UCG

Indirect influences of terrain included both kinematic and thermodynamic alterations to the mesoscale environment. Time series of spatially averaged surface-based CAPE, CIN, LFC height, and LCL height revealed only subtle changes between the experiments, with the FLAT experiment most deviant from the others (Fig. 5.10). As terrain height was raised, surface-based CAPE decreased slightly and surface-based CIN increased slightly, similar to the WRF modeling results presented in Mulholland et al. (2019). The FLAT experiment generally displayed larger CAPE and CIN with lower LFC and LCL heights compared with the experiments with terrain. The much lower LCL height in the FLAT experiment might be one reason for its lack of UCG, as subcloud evaporative cooling potential was reduced (Fig. 10d).

The increase in low-level upslope flow (not shown) in the higher terrain experiments increased wind shear immediately east of the terrain, similar to results presented in Scheffknecht et al. (2017). Time series of spatially averaged bulk wind difference over different tropospheric layers revealed a monotonic increase in wind shear with increasing terrain height (Fig. 5.11). Thus, in a relative sense, changes to the kinematic profiles owing to terrain appeared to be more significant than changes to the thermodynamic profiles owing to terrain. This result agrees with Soderholm et al. (2014) who stated that variations to the wind shear profile owing to terrain were more important to convective morphology than thermodynamic variations owing to terrain. The larger magnitudes of low-level wind shear in the FLAT experiment are another probable cause for

the lack of UCG with a predominant supercellular convective mode present throughout most of the simulation.

The alterations to the wind shear profile owing to terrain are a plausible explanation for the trends noted in the different terrain supercell updraft and downdraft widths and intensities, which ultimately affected UCG. The larger magnitudes of wind shear (e.g., Fig. 5.11) are a probable cause of the wider updrafts and more intense supercells in the higher terrain experiments. Supercell updraft width has been shown to scale with wind shear magnitude, with stronger wind shears leading to wider updrafts (e.g., Trapp et al. 2017; Warren et al. 2017; Dennis and Kumjian 2017; Marion and Trapp 2019). These aforementioned studies used a more highly-idealized modeling framework (i.e., warm bubble initiation, no friction/radiation/fluxes/terrain), so the results shown here from a more "realistic" approach further support the claim that stronger wind shear generally leads to wider updrafts. Wider updrafts are more resilient to the deleterious effects of entrainment-driven dilution, ultimately resulting in updrafts that are more efficient at realizing their maximum core buoyancies. Thus, it is consistent that the wider supercell updrafts in the higher terrain experiments were stronger as a result than their lower terrain supercell updraft counterparts.

5.1.4 Direct Influences of Terrain on UCG

A direct influence of the terrain included terrain blocking of supercell cold pools. Horizontal plan views of the cold pools at peak supercell time revealed that the cold pools were blocked by terrain on their western flanks in the terrain experiments (Fig. 5.12). West-to-east and north-to-south oriented vertical cross-sections through the strongest cold pool location (time averaged +/- 5 min around peak supercell time) affirms that the cold pools in the higher terrain experiments were indeed blocked by the higher terrain to the west, and were deeper as a result, similar to results presented in Xu et al. (2012) and Phadtare (2018) (Fig. 5.13). Time series of

average cold pool depth depicted a clear trend for deeper cold pools with increasing terrain height (Fig. 5.14). Cold pool depth has been shown to be the most important cold pool characteristic that determines the chances for secondary CI along an outflow boundary (e.g., Droegemeier and Wilhelmson 1987). Thus, it is consistent that as the terrain was raised and cold pools where blocked and became deeper, the rate of UCG generally increased. The UCG rate increase is related to the ability of the deeper cold pools to more easily lift air parcels to their LFCs, allow secondary CI, and result in an areal growth of precipitation.

An analysis of near-surface pressure perturbation during peak supercell stage revealed that the higher terrain supercells typically displayed stronger high pressure perturbations associated with convective cold pools (Fig. 5.15). This is also supported by a time series of the 90th percentile of near-surface pressure perturbation leading up to peak supercell stage (Fig. 5.16). The increase of near-surface high pressure perturbation within the deepening convective cold pools was likely influenced by the terrain blocking, but also the slower supercell motions with increasing terrain height, allowing for the accumulation of negatively buoyant air (e.g., Fig. 5.2). The greater near-surface high pressure perturbations associated with the convective cold pools resulted in a greater low-level horizontal pressure gradient between the supercell cold pools and their ambient environments. This was especially true not only along the western flanks of the higher terrain supercells where the cold pool was blocked along the high terrain, but also within the northeastern (forward-flank) region of the supercells (Fig. 5.15). The trend for a strengthening low-level horizontal pressure gradient force and resultant cold pool surge associated with a supercell's strengthening cold pool prior to UCG was also noted by Finley et al. (2001). Additionally, cold pool surges within an MCS owing to an enhanced low-level horizontal pressure gradient force between the cold pool's mesohigh and the ambient environment were also described by Peters and

Schumacher (2015) and references therein. This enhanced low-level horizontal pressure gradient along the terrain explains why the outflow in the higher terrain supercells accelerated southward more quickly away from the parent DMC. The accelerating outflow, which was deeper at its leading edge in the higher terrain experiments (e.g., Fig. 5.13), fostered additional secondary CI along the outflow boundary, resulting in relatively more rapid UCG.

5.2 Summary and Conclusions

This study addressed the direct and indirect influences of terrain on the UCG of orographic supercells. A series of idealized numerical modeling simulations were devised in order to elucidate the mechanisms that supported the growth of an orographic supercell into an MCS. A suite of simulations were conducted in which the initial terrain height was systematically varied between 0 m (FLAT) to 4500 m.

Similar to the WRF simulations of an orographic supercell-to-MCS case study presented by Mulholland et al. (2019), the higher terrain experiments conducted here showed earlier CI, a more intense supercell, and relatively faster UCG. The earlier CI in the higher terrain experiments was attributed to earlier and stronger upslope flows, along with dynamically enhanced upward vertical motions owing to a standing mountain wave (not shown). The stronger upslope flows in the higher terrain experiments also enhanced wind shear downwind of the terrain (indirect influence). This enhanced wind shear in the higher terrain experiments fostered wider supercell updrafts that obtained stronger upward and downward vertical velocities.

The wider supercell updrafts resulted in a greater horizontal extent over which precipitation formed. The wider and stronger updrafts also supported greater vertical mass flux, which in turn, led to stronger and generally wider downdrafts. The stronger and wider downdrafts were manifested by deeper and relatively stronger cold pools in the higher terrain supercells. As cold

pools were blocked by the higher terrain to the west (direct influence), an accumulation of negatively buoyant air led to an enhanced low-level horizontal pressure gradient, driving surging outflow that prompted the relatively faster UCG in higher terrain experiments. Interestingly, the outflow that initially drove the relatively faster UCG in the higher terrain supercells ultimately outpaced the parent convection, leading to a quicker demise of the nascent MCS (also noted by Klimowski et al. 2004). Future work should include how terrain influences the maintenance and eventual longevity of orographic MCSs by way of direct and indirect influences. Interestingly, lower terrain experiments still displayed UCG, however, by way of merging convective cells and not by a single dominant supercell growing into an MCS. Future work on how terrain affects the various pathways of UCG should be also conducted.

In summary, terrain appears to play a central role in the UCG of orographic supercells by way of both direct and indirect influences. Evidence was presented to support the idea of terrain blocking of cold pools, a direct influence. Of the possible indirect influences of terrain, enhancements to wind shear over different tropospheric layers appeared more crucial to DMC morphology than alterations to the thermodynamic environment, in line with conclusions drawn by Soderholm et al. (2014). The enhanced wind shear in the higher terrain experiments lead to wider and more intense supercells, supporting relatively faster UCG. The FLAT supercell lasted for a much longer duration than the 4500 m supercell even though both simulations were initialized with similar base state environments. Thus, having the terrain present for this particular environment was crucial for the rapid supercell-to-MCS transition.

While there was no evidence for an “optimal” terrain height for the most rapid UCG, there does appear to be some “tipping point” between the 2500 m-CTRL and 2000 m experiments. The DMC morphology between these two experiments was quite different with the 2500 m-CTRL

experiment depicting an isolated orographic supercell that grew into an MCS; whereas, the 2000 m experiment depicted merging of weaker convective cells away from the terrain to form an MCS. Thus, there might be some "optimal" terrain height for a specific pathway of UCG.

While this study addressed some of the direct and indirect influences of terrain on the UCG of orographic supercells, it certainly does not answer all questions related to terrain influences on UCG. For example, why was there not a monotonic increase in the rate of UCG for higher terrain experiments given the wider/stronger supercell updrafts/downdrafts and deeper/stronger cold pools that were more readily blocked? Furthermore, the modeling framework adopted here excludes the influences of baroclinic boundaries, low-level jets, upper-level troughs, among other synoptically-relevant features that more-than-certainly have an influence on UCG (e.g., Coniglio et al. 2010). Future work on this topic includes building a long-term climatology of UCG (any pathway, not just supercell-to-MCS transitions) events and 'null' events (where an MCS was forecast, but did not occur), both near terrain and over flatter, more homogeneous surfaces, to reveal any distinguishing environmental factors between the two. These environmental constraints will be used to drive a much larger suite of idealized numerical modeling experiments than shown here in which a larger parameter space (not just one particular environmental as was used here) is tested to report on the sensitivity of UCG to such environmental changes.

5.3 Tables and Figures

Experiment	Convection Initiation	Peak Supercell	Upscale Convective Growth
FLAT	25	230	N/A^{+}
500 m	165*	340	N/A^{+}
1500 m	110*	345	N/A^{+}
2000 m	110*	355	N/A^{+}
2500 m - CTRL	155	325	385
3000 m	130	325	395
3500 m	75	325	345
4500 m	65	320	370

Table 5.1: Summary table of the number of minutes into the simulations of convection initiation, peak supercell, and upscale convective growth stages.
* -- mechanism for convection initiation was a low-level convergence zone to the north of the terrain peak (i.e., not directly related to the terrain peak)
+ -- storms in these simulations grew upscale into an MCS owing to cell mergers, which by the definition outlined in the text, did not meet the upscale convective growth criteria (i.e., single supercell storm that transitions into an MCS)

Experiment	Peak Upward Vertical Velocity [m s^{-1}]	Peak Downward Vertical Velocity [m s^{-1}]
FLAT	89.6	-61.9
2500 m - CTRL	88.8	-63.5
3000 m	88.0	-65.5
3500 m	92.5	-66.2
4500 m	92.8	-69.7

Table 5.2: Summary table of runtime peak upward and downward vertical velocity magnitudes (m s^{-1}).

Experiment	Minimum Lowest Model-Level Potential Temperature Perturbation [K]
FLAT	-10.1
2500 m - CTRL	-13.9
3000 m	-13.4
3500 m	-14.5
4500 m	-13.7

Table 5.3: Summary table of the minimum lowest model-level potential temperature perturbation (K).

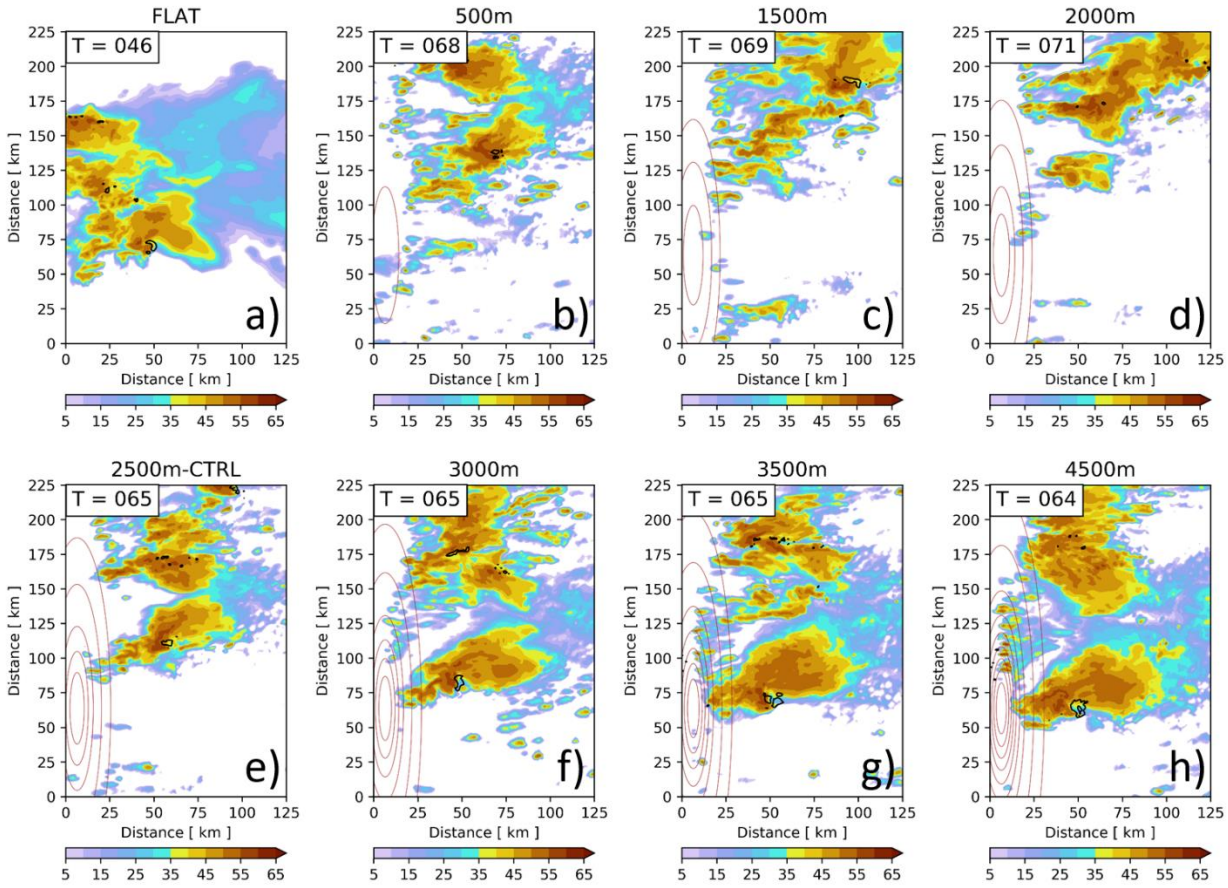

Figure 5.1: Horizontal plan views of near-surface radar reflectivity (shaded; dBZ), 1–4 km AGL average vertical velocity (black contour = 10 m s^{-1}), and terrain height (contoured in brown; m) at peak supercell time for the: (a) FLAT, (b) 500 m, (c), 1500 m, (d) 2000 m, (e) 2500 m-CTRL, (f) 3000 m, (g) 3500 m, and (h) 4500 m terrain height experiments. Note: T = time of output (output every 5 min).

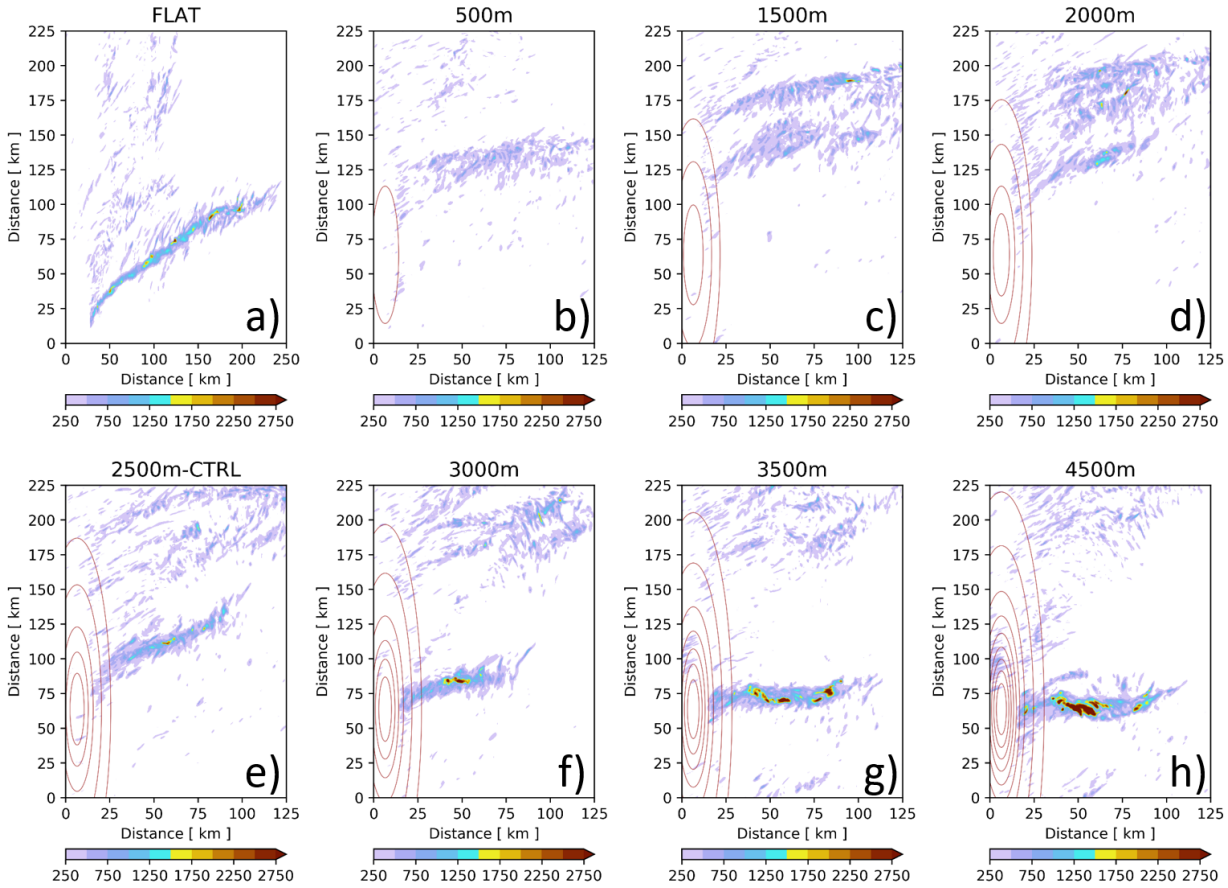

Figure 5.2: Horizontal plan views of runtime accumulated 2–5 km AGL updraft helicity (shaded; $m^2 s^{-2}$) and terrain height (contoured in brown; m) for the: (a) FLAT, (b) 500 m, (c), 1500 m, (d) 2000 m, (e) 2500 m-CTRL, (f) 3000 m, (g) 3500 m, and (h) 4500 m terrain height experiments. Note that the west-to-east distance in panel (a) (FLAT) is twice the distance as the other panels.

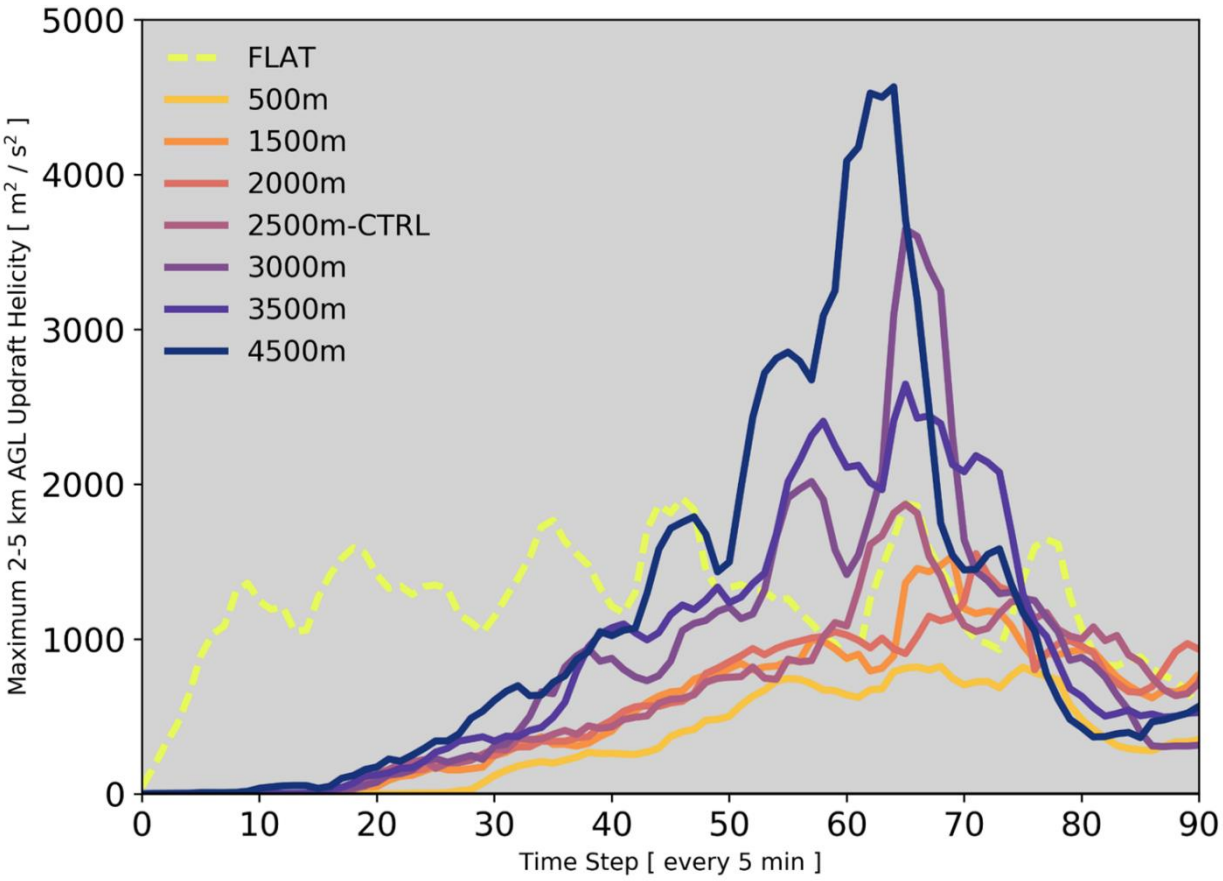

Figure 5.3: Time series of five-point running mean maximum 2–5 km AGL updraft helicity ($m^2 s^{-2}$).

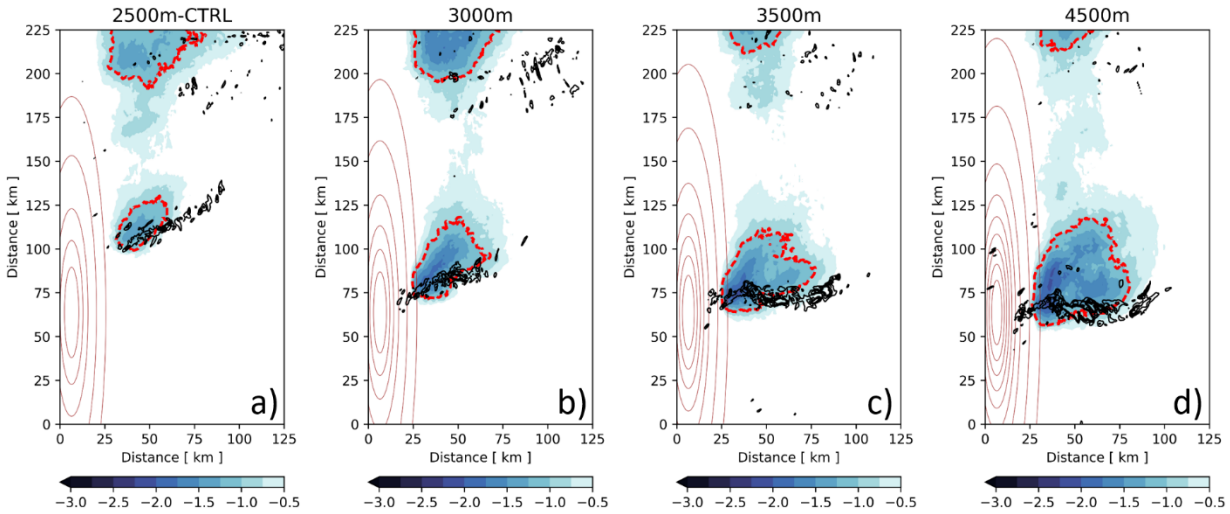

Figure 5.4: Time-averaged (over first 6 h of simulations) near-surface potential temperature perturbation (shaded; K), the -1 K near-surface potential temperature perturbation contour (dashed red line), runtime accumulated 2–5 km AGL updraft helicity (black contours every 500 m^2 s^{-2} starting at 750 m^2 s^{-2}), and terrain height (contoured in brown; m) for the: (a) 2500 m-CTRL, (b) 3000 m, (c) 3500 m, and (d) 4500 m terrain height experiments. Note that the FLAT experiment is omitted.

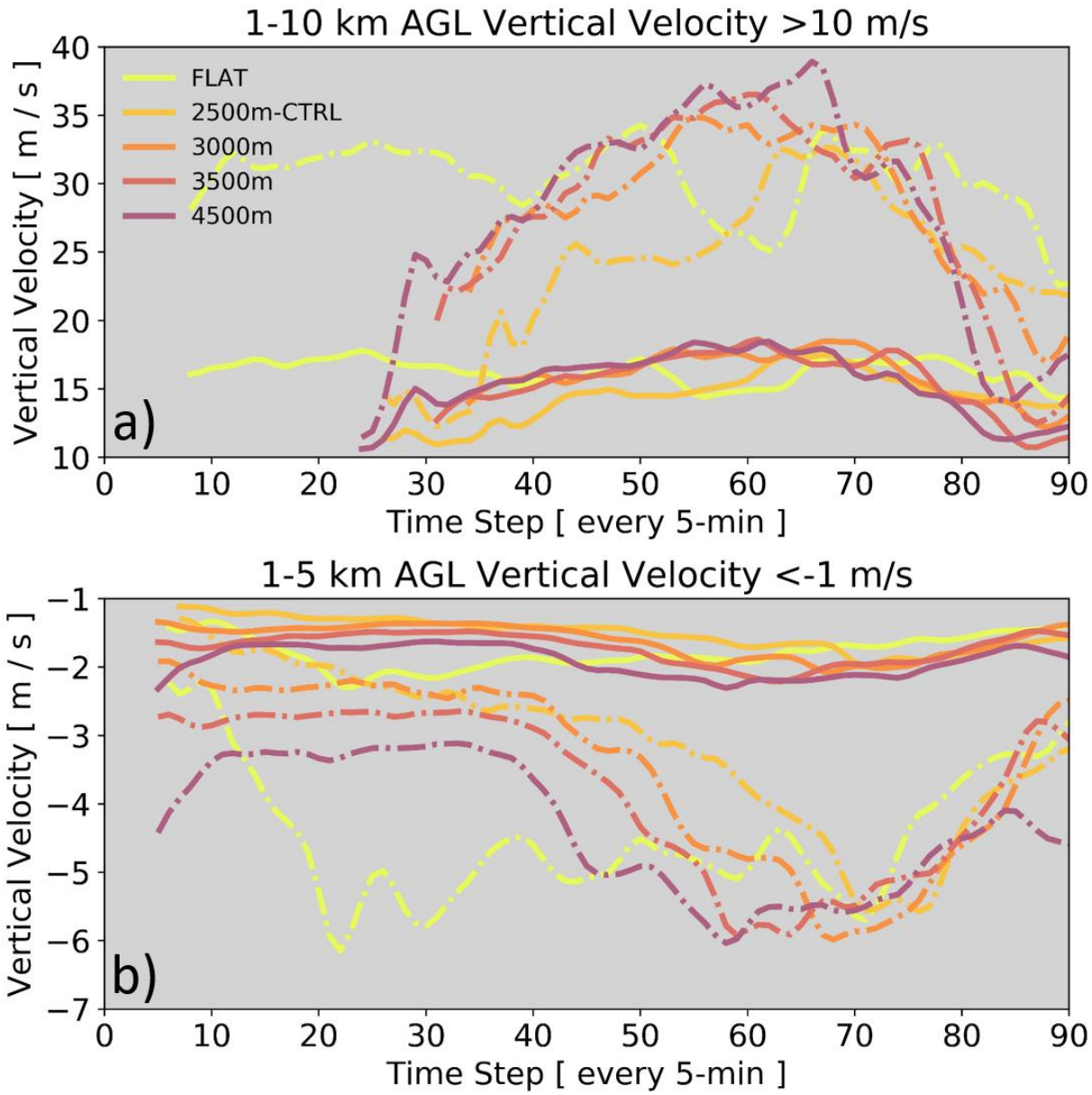

Figure 5.5: Time series of: (a) 1–10 km AGL vertical velocity >10 m s^{-1} and (b) 1–5 km AGL vertical velocity < -1 m s^{-1}. The solid lines represent the mean of each terrain experiment and the dot-dash lines represent the 90th percentile of each terrain experiment. Each distribution was smoothed using a 1-D Gaussian smoother with σ = 1.

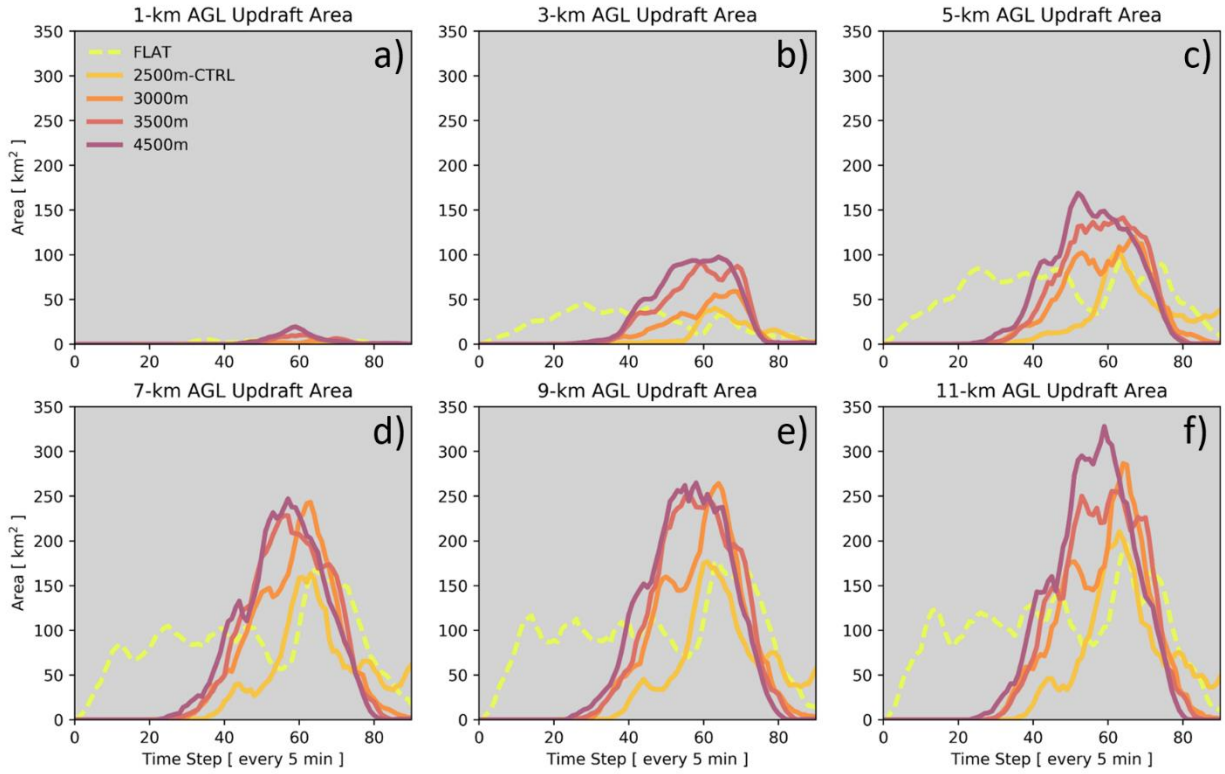

Figure 5.6: Time series of updraft area (km^2; *w* threshold ≥10 m s^{-1}) for the different terrain experiments at different heights of: (a) 1 km AGL, (b) 3 km AGL, (c) 5 km AGL, (d) 7 km AGL, (e) 9 km AGL, and (f) 11 km AGL.

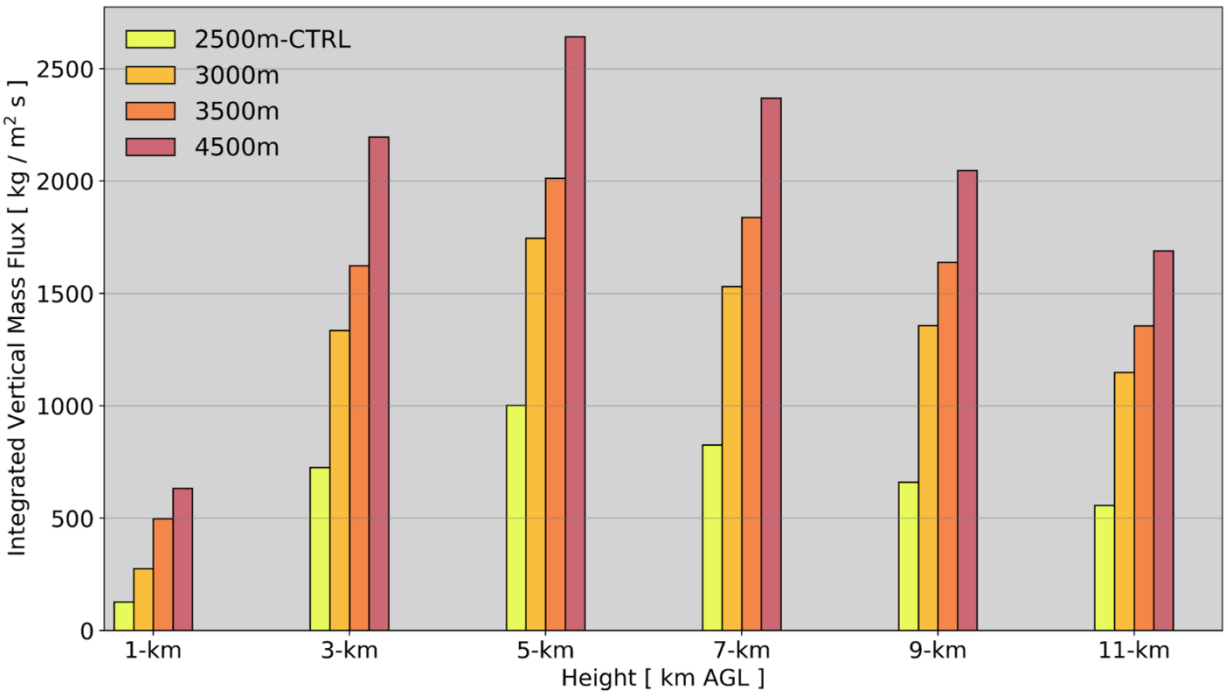

Figure 5.7: Time-integrated vertical mass flux (kg m^{-2} s^{-1}; 2–5 km AGL updraft helicity threshold ≥250 m^2 s^{-2}) up until the initial time step of upscale convective growth for the different terrain experiments at different heights of 1 km AGL, 3 km AGL, 5 km AGL, 7 km AGL, 9 km AGL, and 11 km AGL.

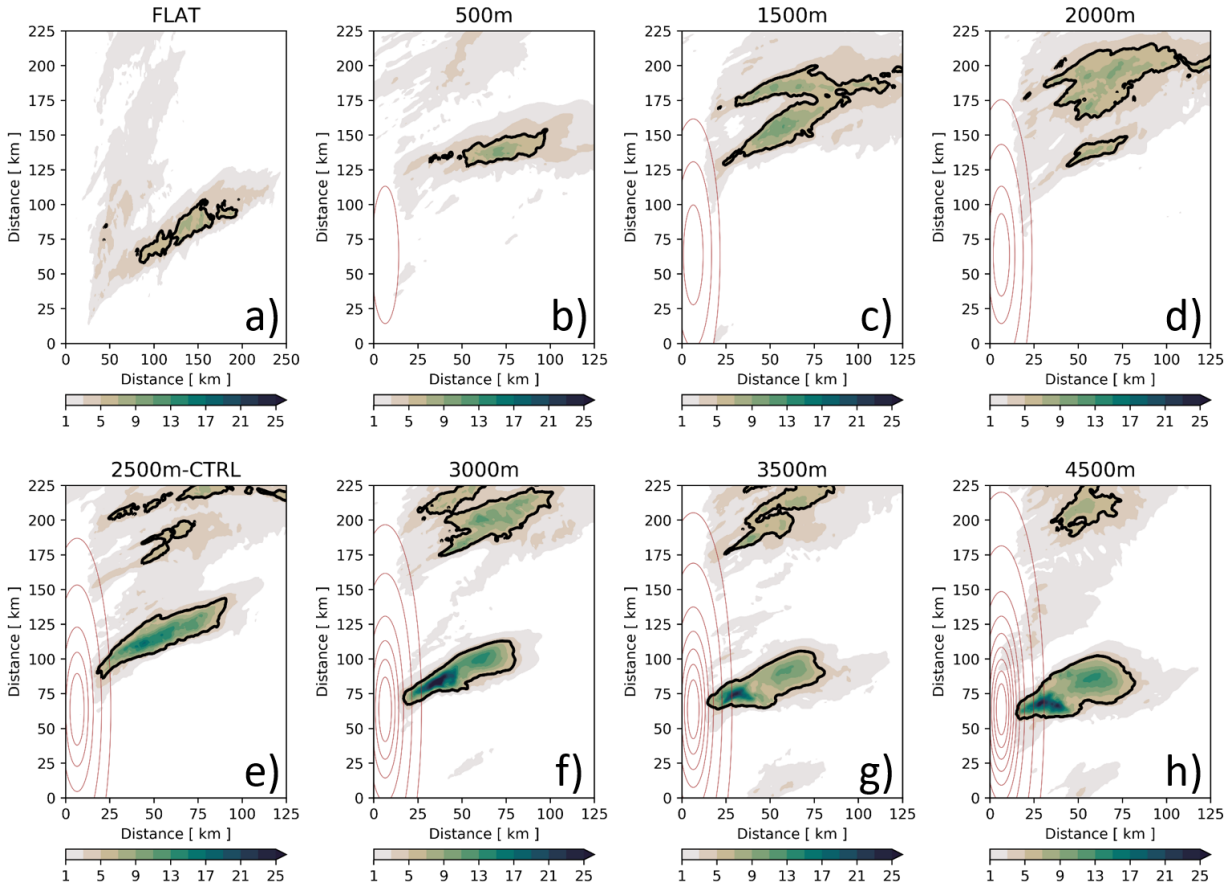

Figure 5.8: Same as in Fig. 5.2, but of runtime accumulated surface rainfall (shaded; cm) and the 5 cm surface rainfall accumulation contour (thick black line).

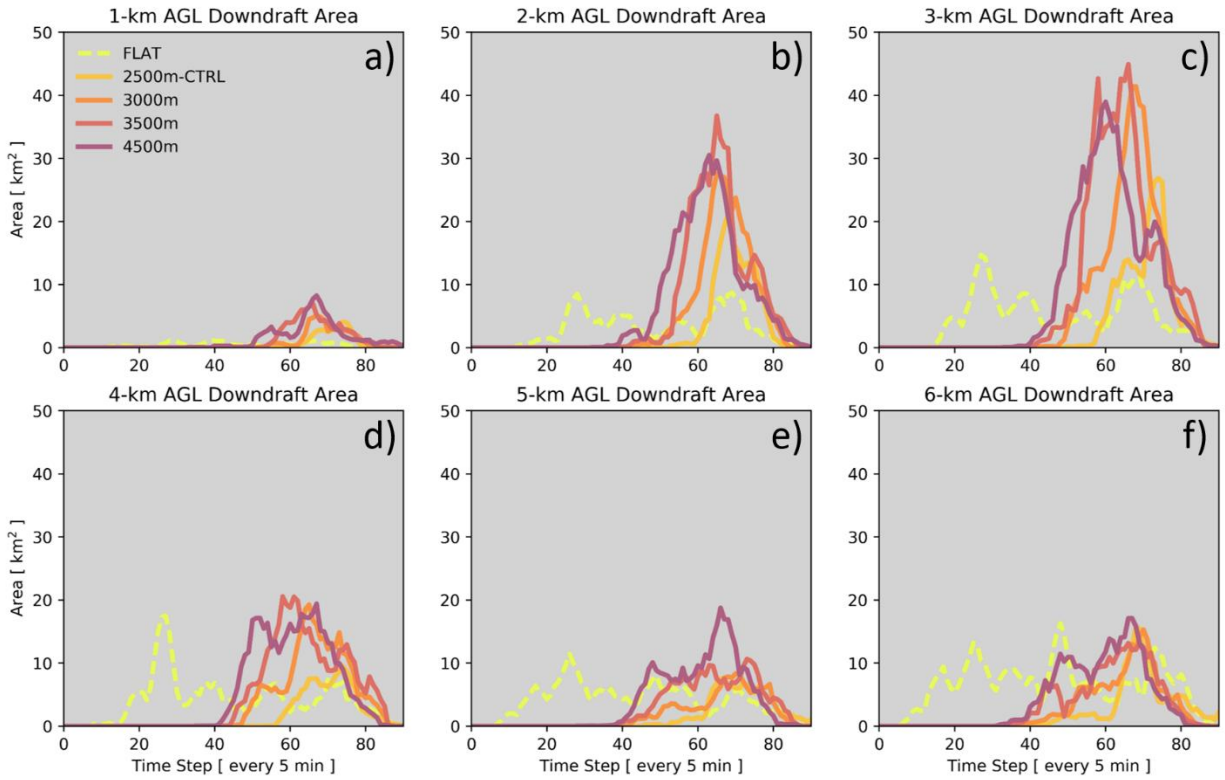

Figure 5.9: Time series of downdraft area (km^2; *w* threshold ≤ -10 m s^{-1}) for the different terrain experiments at different heights of: (a) 1 km AGL, (b) 2 km AGL, (c) 3 km AGL, (d) 4 km AGL, (e) 5 km AGL, and (f) 6 km AGL.

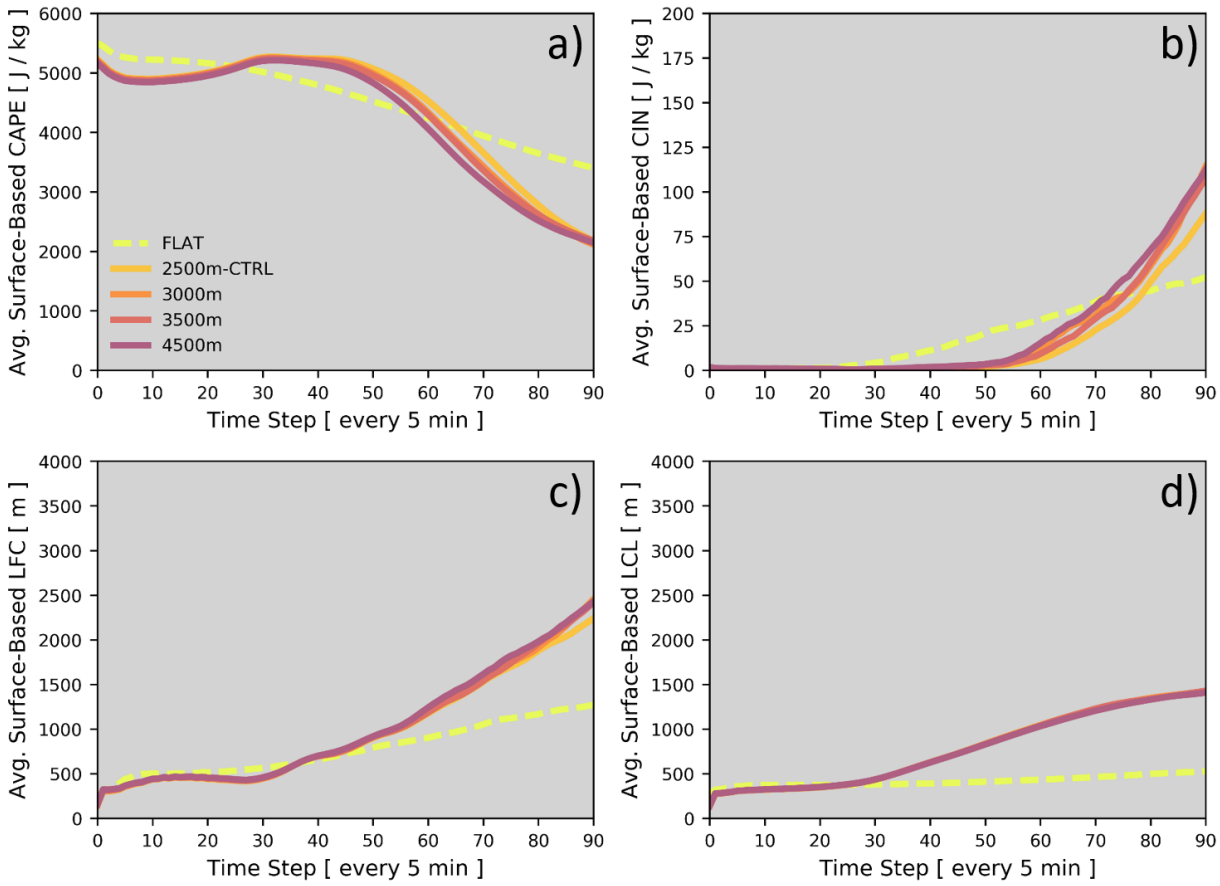

Figure 5.10: Time series of spatially averaged (over a 50 x 150 km box east of terrain peak at grid points where lowest model-level reflectivity <0 dBZ) surface-based: (a) convective available potential energy (CAPE; J kg^{-1}), (b) convective inhibition (CIN; J kg^{-1}), (c) level of free convection (LFC; m) and (d) lifting condensation level (LCL; m).

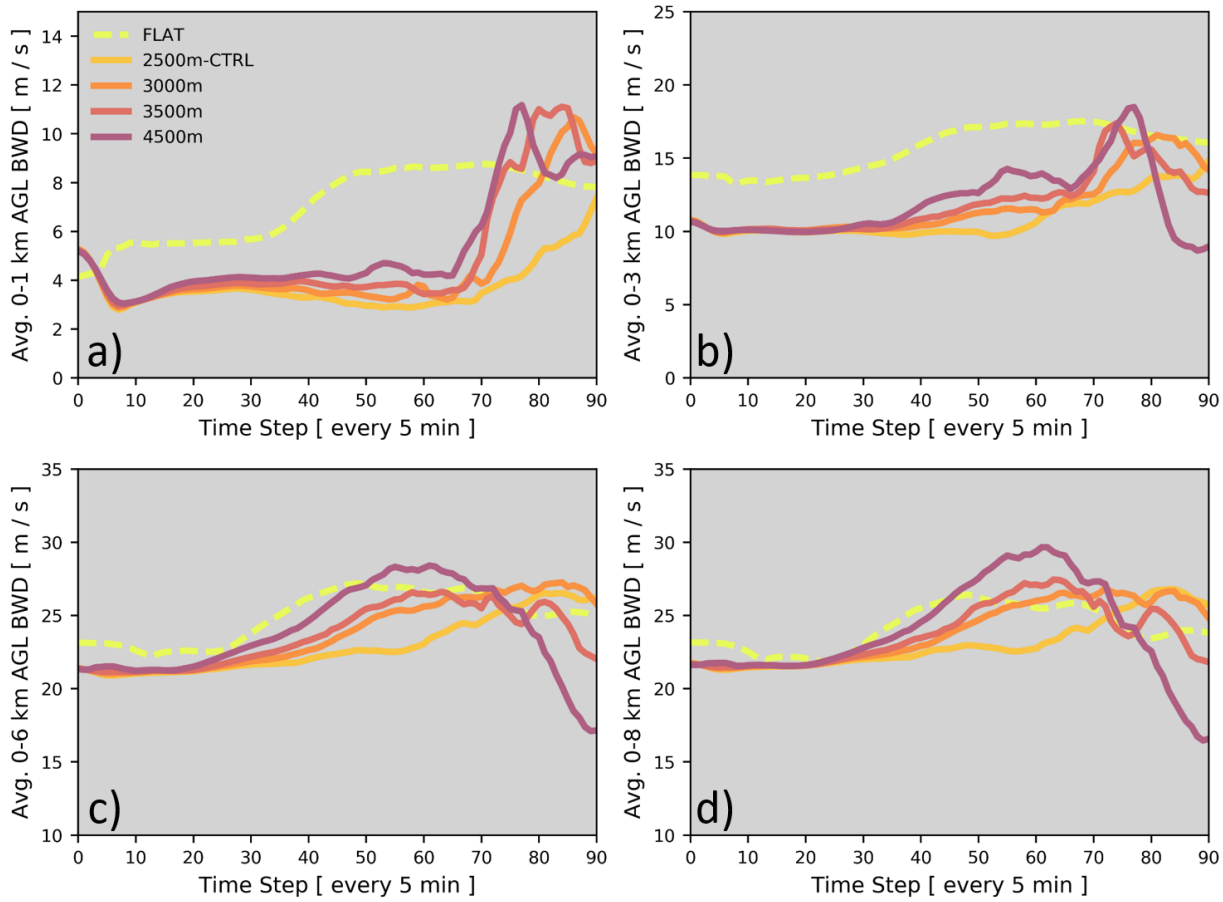

Figure 5.11: Time series of spatially averaged (over a 50 x 150 km box east of terrain peak at grid points where lowest model-level reflectivity <0 dBZ) (a) 0–1 km AGL bulk wind difference (BWD; m s^{-1}), (b) 0–3 km AGL BWD (m s^{-1}), (c) 0–6 km AGL BWD (m s^{-1}), and (d) 0–8 km AGL BWD (m s^{-1}) for the different terrain experiments.

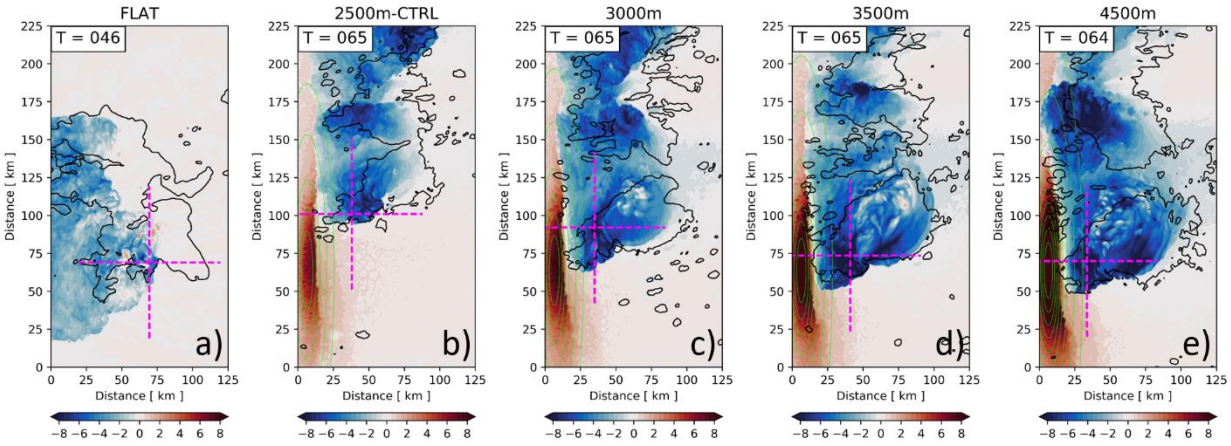

Figure 5.12: Same as in Fig. 5.1, but near-surface reflectivity (black contour = 30 dBZ), near-surface potential temperature perturbation (shaded; K), and terrain height (contoured in green; m). The horizontal and vertical dashed magenta lines show the paths along which the vertical cross-sections depicted in Fig. 5.13 are taken.

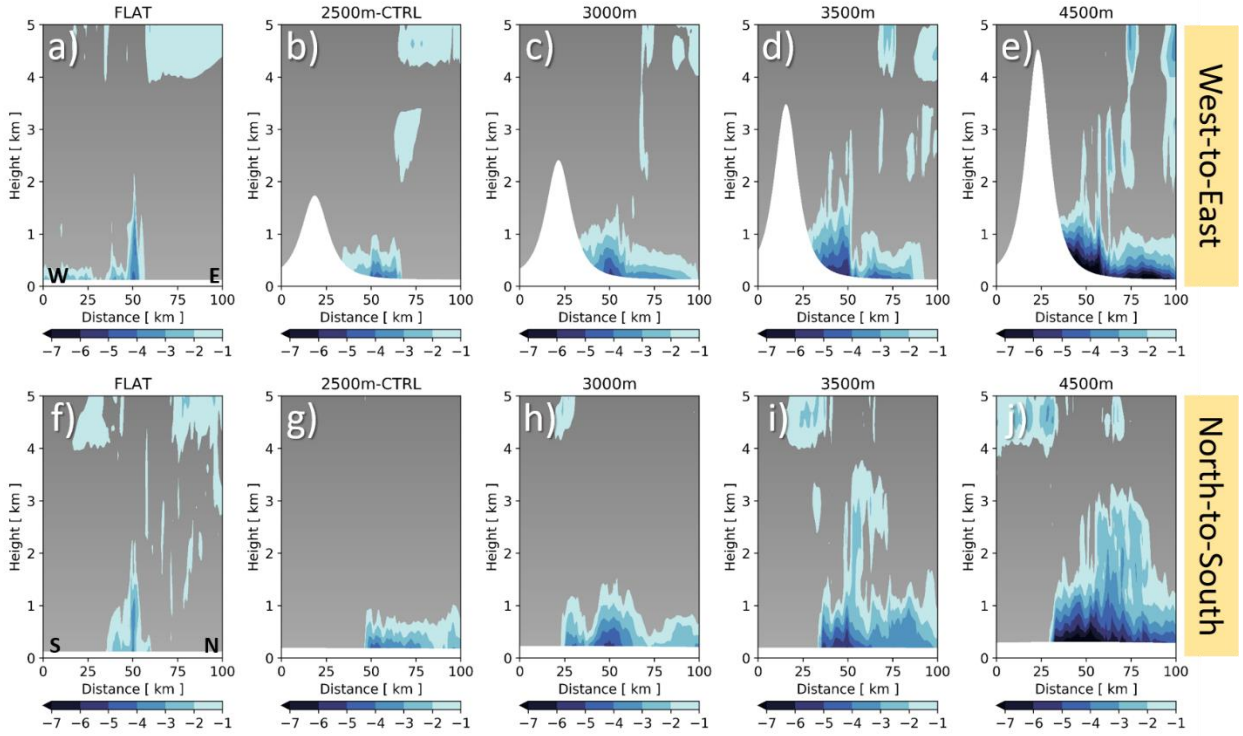

Figure 5.13: West-to-east (top) and north-to-south (bottom) oriented vertical cross-sections through the strongest portion of the peak supercell cold pools (time averaged +/- 5 min around peak supercell time) of potential temperature perturbation (shaded; K) and terrain (white regions) for the: (a, f) FLAT, (b, g) 2500m-CTRL, (c, h) 3000m, (d, i) 3500 m, and (e, j) 4500 m terrain experiments. See Fig. 5.12 for the horizontal pathways along which these vertical cross sections were taken.

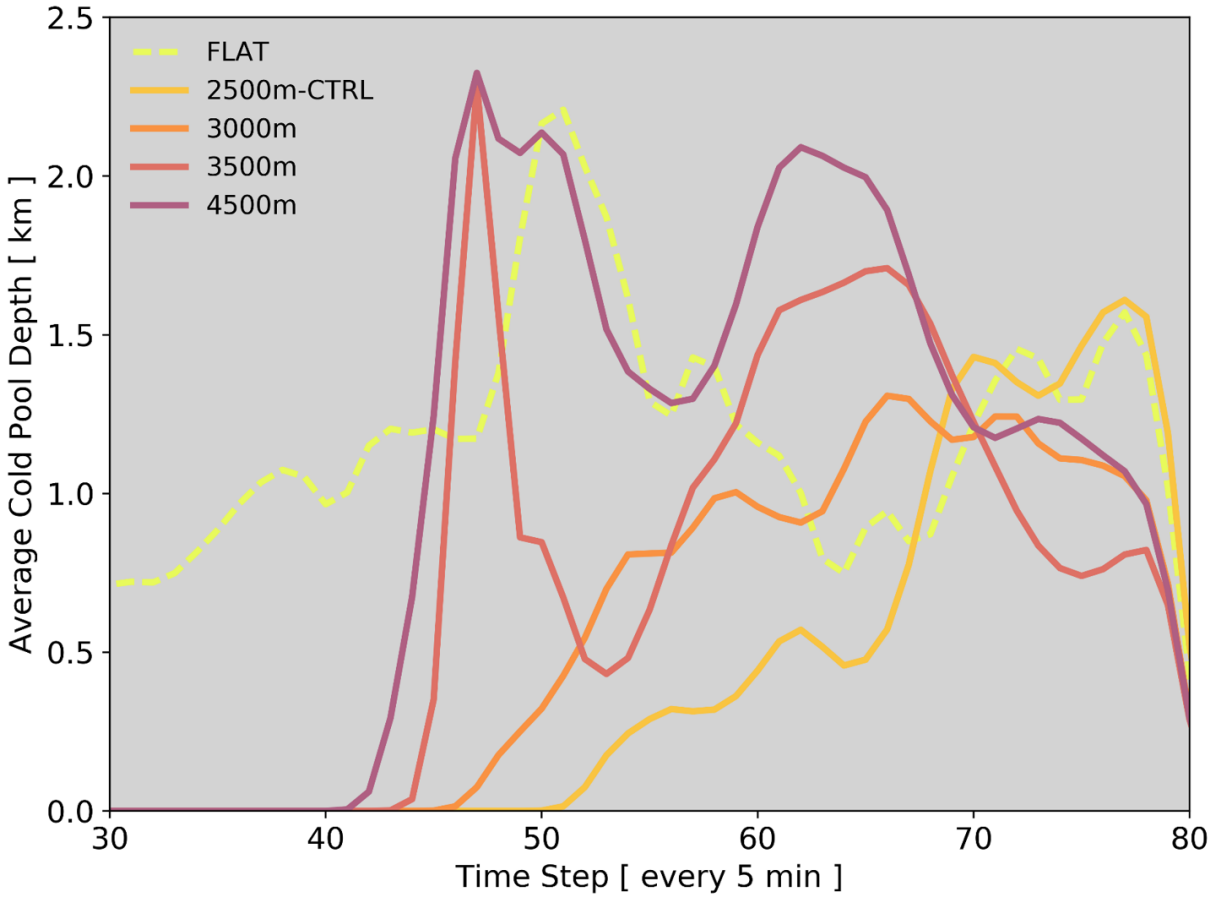

Figure 5.14: Time series of average cold pool depth based on the potential temperature perturbation -3 K contour (km). The averages were associated with the supercell cold pools within the near-surface potential temperature perturbation -3 K contour.

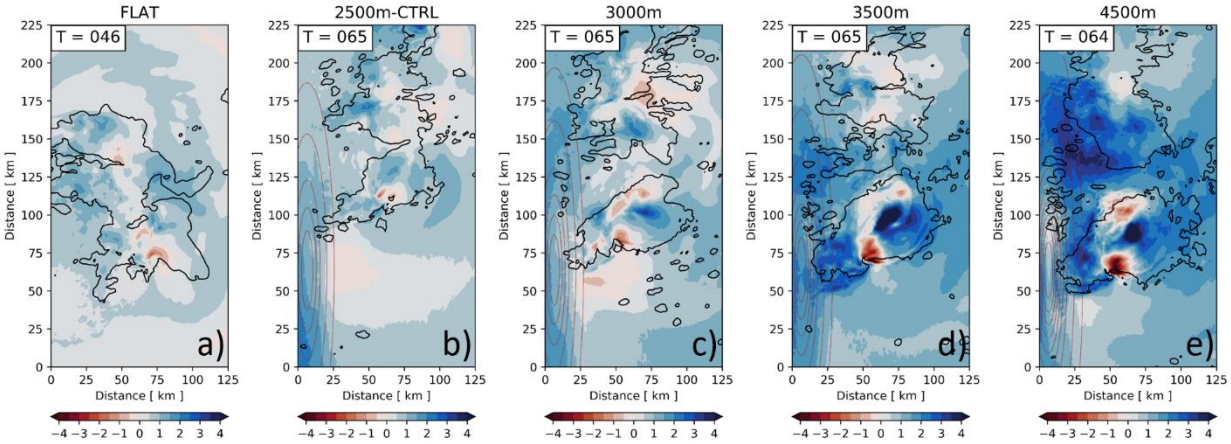

Figure 5.15: Same as in Fig. 5.1, but near-surface reflectivity (black contour = 30 dBZ), near-surface pressure perturbation (shaded; hPa), and terrain height (contoured in brown; m).

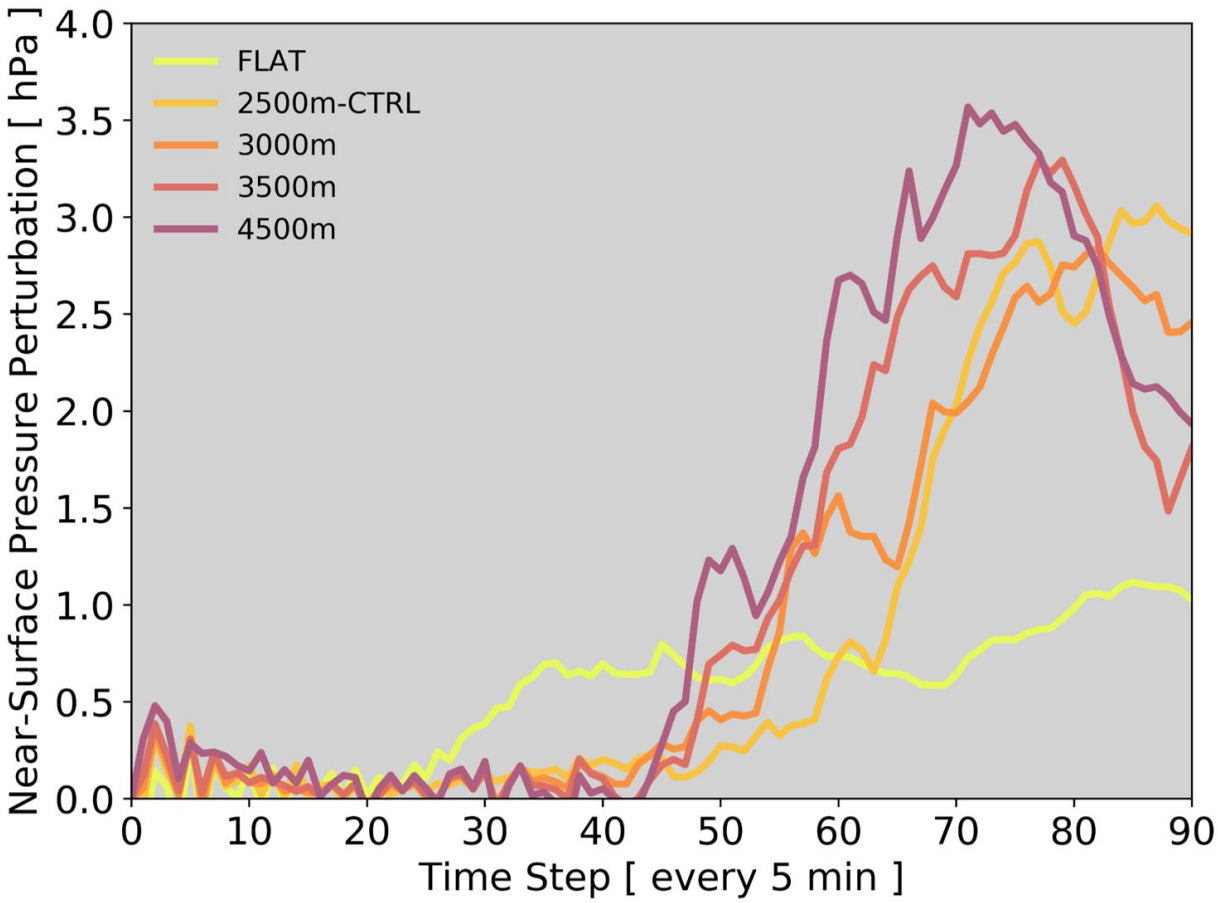

Figure 5.16: Time series of the 90th percentile of near-surface pressure perturbation (hPa).

REFERENCES

Bluestein, H. B., and M. H. Jain, 1985: Formation of mesoscale lines of precipitation: Severe squall lines in Oklahoma during the spring. *J. Atmos. Sci.*, **42**, 1711–1732.

—, and M. L. Weisman, 2000: The interaction of numerically simulated supercells initiated along lines. *Mon. Wea. Rev.*, **128**, 3128–3149.

Blumberg, W. G., and Coauthors, 2017: SHARPpy: An open-source sounding analysis toolkit for the Atmospheric Sciences. *Bull. Amer. Meteor. Soc.*, **98**, 1625-1636.

Bonner, W. D., 1968: Climatology of the low level jet. *Mon. Wea. Rev.*, **96**, 833–850.

Brooks, H., C. A. Doswell III, and M. P. Kay, 2003: Climatological estimates of local daily tornado probability for the United States. *Wea. Forecasting*, **18**, 626–640.

Bryan, G. H., and M. J. Fritsch, 2002: A benchmark simulation for moist nonhydrostatic numerical models. *Mon. Wea. Rev.*, **130**, 2917–2928.

—, J. C. Wyngaard, and J. M. Fritsch, 2003: Resolution requirements for the simulation of deep moist convection. *Mon. Wea. Rev.*, **131**, 2394–2416.

Cecil, D. J., and C. B. Blankenship, 2012: Toward a global climatology of severe hailstorms as estimated by satellite passive microwave imagers. *J. Climate*, **25**, 687–703.

Coniglio, M. C., D. J. Stensrud, and L. J. Wicker, 2006: Effects of upper-level shear on the structure and maintenance of strong quasi-linear mesoscale convective systems. *J. Atmos. Sci.*, **63**, 1231–1252.

—, J. Y. Hwang, and D. J. Stensrud, 2010: Environmental factors in the upscale growth and longevity of MCSs derived from Rapid Update Cycle analyses. *Mon. Wea. Rev.*, **138**, 3514–3539.

Davies-Jones, R., 1984: Streamwise vorticity: The origin of updraft rotation in supercell storms. *J. Atmos. Sci.*, **41**, 2991–3006.

Dee, D. P., and Coauthors, 2011: The ERA-Interim reanalysis: Configuration and performance of the data assimilation system. *Quart. J. Roy. Meteor. Soc.*, **137**, 553–597.

Dennis, E. J., and M. R. Kumjian, 2017: The impact of vertical wind shear on hail growth in simulated supercells. *J. Atmos. Sci.*, **74**, 641–663.

Dial, G. L., J. P. Racy, and R. L. Thompson, 2010: Short-term convective mode evolution along synoptic boundaries. *Wea. Forecasting*, **25**, 1430–1446.

Done, J., C. A. Davis, and M. Weisman, 2004: The next generation of NWP: explicit forecasts of convection using the weather research and forecasting (WRF) model. Atmos. Sci. Let., 5, 110–117.

Donelan, M. A., B. K. Haus, N. Reul, W. J. Plant, M. Stiassnie, H. C. Graber, O. B. Brown, and E. S. Saltzman, 2004: On the limiting aerodynamic roughness of the ocean in very strong winds. *Geophys. Res. Lett.*, **31**, L18306.

Dörnbrack, A., J. D. Doyle, T. P. Lane, R. D. Sharman, and P. K. Smolarkiewicz, 2005: On physical realizability and uncertainty of numerical solutions. *Atmos. Sci. Lett.*, **6**, 118–122.

Doswell, C. A., III, H. E. Brooks, and R. A. Maddox, 1996: Flash flood forecasting: An ingredients-based methodology. *Wea. Forecasting*, **11**, 560–581.

Droegemeier, K. K., and R. B. Wilhelmson, 1987: Numerical simulation of thunderstorm outflow dynamics. Part I: Outflow sensitivity experiments and turbulence dynamics. *J. Atmos. Sci.*, **44**, 1180–1210.

Dudhia, Jimy, 1996: A multi-layer soil temperature model for MM5. the Sixth PSU/NCAR Mesoscale Model Users' Workshop.

Fabry, F., 2015: *Radar Meteorology: Principles and Practice*. Cambridge University Press, 256 pp.

Fairall, C. W., E. F. Bradley, J. E. Hare, A. A. Grachev, and J. B. Edson, 2003: Bulk parameterization of air–sea fluxes: Updates and verification for the COARE algorithm. *J. Climate*, **16**, 571–591.

Finley, C. A., W. R. Cotton, and R. A. Pielke Sr., 2001: Numerical simulation of tornadogenesis in a high-precipitation supercell. Part I: Storm evolution and transition into a bow echo. *J. Atmos. Sci.*, **58**, 1597–1629.

Frame, J., and P. Markowski, 2006: The interaction of simulated squall lines with idealized mountain ridges. *Mon. Wea. Rev.*, **134**, 1919–1941.

Fritsch, J. M., and R. A. Maddox, 1981: Convectively driven mesoscale weather systems aloft. Part II: Numerical simulations. *J. Appl. Meteor.*, **20**, 20–26.

Fu, D., and X. Guo, 2012: A cloud-resolving simulation study on the merging processes and effects of topography and environmental winds. *J. Atmos. Sci.*, 69, 1232–1249.

Gallus, W. A., N. A. Snook, and E. V. Johnson, 2008: Spring and summer severe weather reports over the Midwest as a function of convective mode: A preliminary study. *Wea. Forecasting*, **23**, 101–113.

Geerts, B., Q. Miao, and J. C. Demko, 2008: Pressure perturbations and upslope flow over a heated, isolated mountain. *Mon. Wea. Rev.*, **136**, 4272–4288.

Gowan, T. M. and J. W. Steenburgh, 2018: Using idealized large-eddy simulations to understand the impact of downstream terrain on lake-effect snowfall. Preprints, 18th *Conf. on Mountain Meteorology* in Santa Fe, NM, Amer. Meteor. Soc.

Grell, G. A., J. Dudhia, and D. R. Stauffer, 1994: A description of the fifth-generation Penn State/NCAR Mesoscale Model (MM5). NCAR Tech. Note NCAR/TN-3981STR, 121 pp.

Hawblitzel, D. P., F. Zhang, Z. Meng, and C. A. Davis, 2007: Probabilistic evaluation of the dynamics and predictability of a mesoscale convective vortex of 10–13 June 2003. *Mon. Wea. Rev.*, **135**, 1544–1563.

Helmus, J.J. & Collis, S.M., (2016). The Python ARM Radar Toolkit (Py-ART), a Library for Working with Weather Radar Data in the Python Programming Language. Journal of Open Research Software. 4(1), p.e25. DOI: http://doi.org/10.5334/jors.119.

Heymsfield, G. M., B. Geerts, and L. Tian, 2000: TRMM precipitation radar reflectivity profiles as compared with high resolution airborne and ground-based radar measurements. *J. Appl. Meteor.*, **39**, 2080–2102.

Hong, S. Y., Y. Noh, and J. Dudhia, 2006: A new vertical diffusion package with an explicit treatment of entrainment processes. *Mon. Wea. Rev.*, **134**, 2318–2341.

Houze, R. A., Jr., B. F. Smull, and P. Dodge, 1990: Mesoscale organization of springtime rainstorms in Oklahoma. *Mon. Wea. Rev.*, **118**, 613–654.

—, 1993: *Cloud Dynamics*. Academic Press, San Diego, 573 pp.

—, D. C. Wilton, and B. F. Smull, 2007: Monsoon convection in the Himalayan region as seen by the TRMM Precipitation Radar, *Quart. J. Roy. Meteor. Soc.*, **133**, 1389-1411.

—, M. D. Zuluaga, and S. R. Brodzik, 2015: The variable nature of convection in the tropics and subtropics: A legacy of 16 years of the Tropical Rainfall Measuring Mission satellite. *Rev. Geophys.*, **53**, 994–1021.

Iacono, M. J., J. S. Delamere, E. J. Mlawer, M. W. Shephard, S. A. Clough, and W. D. Collins, 2008: Radiative forcing by long-lived greenhouse gases: Calculations with the AER radiative transfer models. *J. Geophys. Res.*, **113**, D13103.

James, R. P., J. M. Fritsch, and P. M. Markowski, 2005: Environmental distinctions between cellular and slabular convective lines. *Mon. Wea. Rev.*, **133**, 2669–2691.

Johns, R. H., and C. A. Doswell, 1992: Severe local storms forecasting. *Wea. Forecasting*, **7**, 588–612.

Johnson, R.H. and B.E. Mapes, 2001: Mesoscale Processes and Severe Convective Weather. *Meteorological Monographs,* **50**, 71–122.

Kain, J. S., and Coauthors, 2008: Some practical considerations regarding horizontal resolution in the first generation of operational convection-allowing NWP. *Wea. Forecasting*, **5**, 931– 952.

Keyser, D. A., and D. R. Johnson, 1984: Effects of diabatic heating on the ageostrophic circulation of an upper tropospheric jet streak. *Mon. Wea. Rev.*, **112**, 1709–1724.

Kirkpatrick, C., E. W. McCaul Jr., and C. Cohen, 2009: Variability of updraft and downdraft characteristics in a large parameter study of convective storms. *Mon. Wea. Rev.*, **137**, 1550–1561.

Kirshbaum, D. J., and C.-C. Wang, 2014: Boundary-layer updrafts driven by airflow over heated terrain. *J. Atmos. Sci.*, **71**, 1425–1442.

Klimowski, B. A., M. R. Hjelmfelt, and M. J. Bunkers, 2004: Radar observations of the early evolution of bow echoes. *Wea. Forecasting*, **19**, 727–734.

Kummerow, C., W. Barnes, T. Kozu, J. Shiue, and J. Simpson, 1998: The Tropical Rainfall Measuring Mission (TRMM) sensor package. *J. Atmos. Oceanic Technol.*, **15**, 809–817.

Laing, A. G., and J. M. Fritsch, 1997: The global population of mesoscale convective complexes. *Quart. J. Roy. Meteor. Soc.*, **123**, 389–405.

Lichtenstein, E. R., 1980: La Depresion del Noroeste Argentino (The Northwestern Argentina Low). Ph.D. dissertation, 223 pp. [Available from Departamento de Ciencias de la Atmosfera, Ciudad Universitaria, 1428, Buenos Aires, Argentina.]

Lilly, D. K., 1979. The dynamical structure and evolution of thunderstorms and squall lines. *Ann. Rev. Earth Planet. Sci.*, **7**, 117–171.

Loftus, A. M., D. B. Weber, and C. A. Doswell, 2008: Parameterized mesoscale forcing mechanisms for initiating numerically simulated isolated multicellular convection. *Mon. Wea. Rev.*, **136**, 2408–2421.

Marion, G. R., and Trapp, R. J., 2019: The dynamical coupling of convective updrafts, downdrafts, and cold pools in simulated supercell thunderstorms. *J. Geophys. Res.*, **124**, 1–20.

Markowski, P. M., J. M. Straka, and E. N. Rasmussen, 2002: Direct surface thermodynamic observations within the rear-flank downdrafts of nontornadic and tornadic supercells. *Mon. Wea. Rev.*, **130**, 1692–1721.

—, and N. Dotzek, 2011: A numerical study of the effects of orography on supercells. *Atmos. Res.*, **100**, 457–478.

—, and Y. P. Richardson, 2014: The influence of environmental low-level shear and cold pools on tornadogenesis: Insights from idealized simulations. *J. Atmos. Sci.,* **71**, 243–275.

Miltenberger, A. K., S. Pfahl, and H. Wernli, 2013: An online trajectory module (version 1.0) for the nonhydrostatic numerical weather prediction model COSMO. *Geosci. Model Dev.,* **6**, 1989–2004.

Moller, A. R., C. A. Doswell III, and R. W. Przybylinski, 1990: High precipitation supercells: A conceptual model and documentation. Preprints, *16th Conf. on Severe Local Storms*, Kananaskis Park, AB, Canada, Amer. Meteor. Soc., 52–57.

Morrison, H., G. Thompson, and V. Tatarskii, 2009: Impact of cloud microphysics on the development of trailing stratiform precipitation in a simulated squall line: Comparison of one- and two moment schemes. *Mon. Wea. Rev.*, **137**, 991–1007.

Mulholland, J. P., S. W. Nesbitt, R. J. Trapp, K. L. Rasmussen, and P. V. Salio, 2018: Convective storm life cycle and environments near the Sierras de Cordoba, Argentina. *Mon. Wea. Rev.,* **146**, 2541–2557.

—, S. W. Nesbitt, R. J. Trapp, 2019: How does terrain influence upscale convective growth of orographic deep moist convection? *Mon. Wea. Rev.*, **Accepted pending minor revisions**.

—, S. W. Nesbitt, and R. J. Trapp, 2019: Quantifying the influences of terrain on upscale convective growth., **In prep**.

Nesbitt, S. W., R. Cifelli, and S. A. Rutledge, 2006: Storm morphology and rainfall characteristics of TRMM precipitation features. *Mon. Wea. Rev.*, **134**, 2702–2721.

Nielsen, E. R., G. R. Herman, R. C. Tournay, J. M. Peters, and R. S. Schumacher, 2015: Double impact: When both tornadoes and flash floods threaten the same place at the same time. *Wea. Forecasting*, **30**, 1673–1693.

Nowotarski, C. J., P. M. Markowski, Y. P. Richardson, and G. H. Bryan, 2014: Properties of a simulated convective boundary layer in an idealized supercell thunderstorm environment. *Mon. Wea. Rev.*, **142**, 3955–3976.

Parker, D. J., 2002: The response of CAPE and CIN to tropospheric thermal variations. *Quart. J. Roy. Meteor. Soc.*, **128**, 119–130.

Perkey, D. J., and R. A. Maddox, 1985: A numerical investigation of a mesoscale convective system. *Mon. Wea. Rev.*, **113**, 553–566.

Peters, J. M., and R. S. Schumacher, 2015: Mechanisms for organization and echo training in a flash-flood-producing mesoscale convective system. *Mon. Wea. Rev.*, **143**, 1058–1085.

—, K. C. Eure, and R. S. Schumacher 2017: Factors that drive MCS growth from supercells. Preprints, *17h Conf. on Mesoscale Processes* in San Diego, CA, Amer. Meteor. Soc.

—, W. Hannah, and H. Morrison, 2019a: The influence of vertical wind shear on moist thermals. *J. Atmos. Sci.,* **76**, 1645–1659.

—, C. J. Nowotarski, and H. Morrison, 2019b: The role of vertical wind shear in modulating maximum supercell updraft velocities. *J. Atmos. Sci.*, **Accepted pending major revisions**.

Phadtare, J., 2018: Role of Eastern Ghats orography and cold pool in an extreme rainfall event over Chennai on 1 December 2015. *Mon. Wea. Rev.,* **146**, 943–965.

Rasmussen, K. L., and R. A. Houze Jr., 2011: Orogenic convection in South America as seen by the TRMM satellite. *Mon. Wea. Rev.,* **139**, 2399–2420.

—, M. D. Zuluaga, and R. A. Houze, 2014: Severe convection and lighting in subtropical South America. *Geophys Res Lett.,* **41**, 7359-7366.

—, and R. A. Houze Jr., 2016: Convective initiation near the Andes in subtropical South America. *Mon. Wea. Rev.*, **144**, 2351–2374.

Rauber, R. M., and S. W. Nesbitt, 2018: *Radar meteororology, an introduction*. Wiley Blackwell, 461 pp.

Repinaldo, H. F. B., M. Nicolini, and Y. G. Skabar, 2015: Characterizing the diurnal cycle of low-level circulation and convergence using CFSR data in southeastern South America. *J. Appl. Meteor. Climatol.*, **54**, 671–690.

Ribeiro, B. Z., and L. F. Bosart, 2018: Elevated mixed layers and associated severe thunderstorm environments in South and North America. *Mon. Wea. Rev.*, **146**, 3-28.

Romatschke, U., and R. A. Houze, Jr., 2010: Extreme summer convection in South America. *J. Climate*, **23**, 3761-3791.

Rotunno, R., J. B. Klemp, and M. L. Weisman, 1988: A theory for strong, long-lived squall lines. *J. Atmos. Sci.*, **45**, 463–485.

Salio, P., M. Nicolini, and E. J. Zipser, 2007: Mesoscale convective systems over southeastern South America and their relationship with the South American low-level jet. *Mon. Wea. Rev.*, **135**, 1290–1309.

Saulo, A. C., M. E. Seluchi, and M. Nicolini, 2004: A case study of a chaco low-level jet event. *Mon. Wea. Rev.*, **132**, 2669–2683.

—, J. Ruiz, and Y. G. Skabar, 2007: Synergism between the low-level jet and organized convection at its exit region. *Mon. Wea. Rev.*, **135**, 1310–1326.

Scheffknecht, P., S. Serafin, and V. Grubisic, 2017: A long-lived supercell over mountainous terrain. *Quart. J. Roy. Meteor. Soc.*, **143**, 2973–2986.

Schmid, B., and Coauthors, 2014: The DOE ARM Aerial Facility. *Bull. Amer. Meteor. Soc.*, **95**, 723–742.

Schumacher, R. S., A. J. Clark, M. Xue, and F. Kong, 2013: Factors influencing the development and maintenance of nocturnal heavy-rain-producing convective systems in a storm-scale ensemble. *Mon. Wea. Rev.*, **141**, 2778–2801.

Schumann, M. R., and P. J. Roebber, 2010: The influence of upper-tropospheric potential vorticity on convective morphology. *Mon. Wea. Rev.*, **138**, 463–474.

Scott, D.W., 1992: *Multivariate Density Estimation: Theory, Practice, and Visualization*. John Wiley & Sons, 336 pp.

Seluchi, M. E., A. C. Saulo, M. Nicolini, and P. Satyamurty, 2003: The northwestern Argentinean low: A study of two typical events. *Mon. Wea. Rev.*, **131**, 2361–2378.

Skamarock, W. C., and Coauthors, 2008: A description of the Advanced Research WRF version 3. NCAR Tech. Note NCAR/TN-475+STR, 113 pp.

Soderholm, B., B. Ronalds, and D. J. Kirshbaum, 2014: The evolution of convective storms initiated by an isolated mountain ridge. *Mon. Wea. Rev.*, **142**, 1430–1451.

Smith, B. T., R. L. Thompson, J. S. Grams, and C. Broyles, 2012: Convective modes for significant severe thunderstorms in the contiguous United States. Part I: Storm classification and climatology. *Wea. Forecasting*, **27**, 1114–1135.

Stechman, D.M., R.M. Rauber, G.M. McFarquhar, B.F. Jewett, and D.P. Jorgensen, 2016: Interaction of an Upper-Tropospheric Jet with a Squall Line Originating along a Cold Frontal Boundary. *Mon. Wea. Rev.,* **144**, 4197–4219.

Stensrud, D. J., 1996: Effects of persistent, midlatitude mesoscale regions of convection on the large-scale environment during the warm season. *J. Atmos. Sci.*, **53**, 3503–3527.

Thompson, R. L., R. Edwards, J. A. Hart, K. L. Elmore, and P. Markowski, 2003: Close proximity soundings within supercell environments obtained from the Rapid Update Cycle. *Wea. Forecasting*, **18**, 1243–1261.

—, B. T. Smith, J. S. Grams, A. R. Dean, and C. Broyles, 2012: Convective modes for significant severe thunderstorms in the contiguous United States. Part II: Supercell and QLCS tornado environments. *Wea. Forecasting*, **27**.

Thompson, G., P. R. Field, R. M. Rasmussen, and W. D. Hall, 2008: Explicit forecasts of winter precipitation using an improved bulk microphysics scheme. Part II: Implementation of a new snow parameterization. *Mon. Wea. Rev.*, **136**, 5095– 5115.

Trapp, R. J., S. A. Tessendorf, E. S. Godfrey, and H. E. Brooks, 2005: Tornadoes from squall lines and bow echoes. Part I: Climatological distribution. *Wea. Forecasting*, **20**, 23–34.

—, 2013: *Mesoscale-Convective Processes in the Atmosphere*. Cambridge University Press, 346 pp.

—, G. R. Marion, and S. W. Nesbitt, 2017: The regulation of tornado intensity by updraft width. *J. Atmos. Sci.*, **74**, 4199– 4211.

Tripoli, G. J., and W. R. Cotton, 1989a: Numerical study of an observed orogenic mesoscale convective system. Part I: Simulated genesis and comparison with observations. *Mon. Wea. Rev.*, **117**, 273–304.

—, and —, 1989b: Numerical study of an observed orogenic mesoscale convective system. Part 2: Analysis of governing dynamics. *Mon. Wea. Rev.*, **117**, 305–328.

Uccellini, L. W., 1980: On the role of upper tropospheric jet streaks and leeside cyclogenesis in the development of low-level jets in the Great Plains. *Mon. Wea. Rev.*, **108**, 1689–1696.

Vera, C., and Coauthors, 2006: The South American Low-Level Jet Experiment. *Bull. Amer. Meteor. Soc.*, **87**, 63–77.

Warren, R. A., H. Richter, H. A. Ramsay, S. T. Siems, and M. J. Manton, 2017: Impact of variations in upper-level shear on simulated supercells. *Mon. Wea. Rev.*, **145**, 2659–2681.

Weisman, M. L., and J. B. Klemp, 1982: The dependence of numerically simulated convective storms on vertical wind shear and buoyancy. *Mon. Wea. Rev.*, **110**, 504–520.

—, C. Evans, and L. Bosart, 2013: The 8 May 2009 Superderecho: Analysis of a real-time explicit convective forecast. *Wea. Forecasting*, **28**, 863–892.

Wilson, J. W., N. A. Crook, C. K. Mueller, J. Sun, and M. Dixon, 1998: Nowcasting thunderstorms: A status report. *Bull. Amer. Meteor. Soc.*, **79**, 2079–2099.

Wolf, B. J., and D. R. Johnson, 1995a: The mesoscale forcing of a midlatitude upper-tropospheric jet streak by a simulated convective system. Part I: Mass circulation and ageostrophic processes. *Mon. Wea. Rev.*, **123**, 1059–1087.

—, and —, 1995b: The mesoscale forcing of a midlatitude upper-tropospheric jet streak by a simulated convective system. Part II: Kinetic energy and resolution analysis. *Mon. Wea. Rev.*, **123**, 1088–1111.

Wurman, J., J. Straka, E. Rasmussen, M. Randall, and A. Zahrai, 1997: Design and deployment of a portable, pencil-beam, pulsed, 3-cm Doppler radar. *J. Atmos. Oceanic Technol.*, **14**, 1502–1512.

Xu, W., E. J. Zipser, Y.-L. Chen, C. Liu, Y.-C. Liou, W.-C. H. Lee, and B. J.-D. Jou, 2012: An orography-associated extreme rainfall event during TiMREX: Initiation, storm evolution, and maintenance. *Mon. Wea. Rev.*, **140**, 2555–2574.

Zipser, E. J., 1977: Mesoscale and convective-scale downdrafts as distinct components of squall-line circulation. *Mon. Wea. Rev.*, **105**, 1568–1589.

—, D. J. Cecil, C. Liu, S. W. Nesbitt, and D. P. Yorty, 2006: Where are the most intense thunderstorms on Earth? *Bull. Amer. Meteor. Soc.*, **87**, 1057–1071.

APPENDIX A: ACRONYMS

AGL - above ground level
B - buoyancy
BSR - broad stratiform
BWD - bulk wind difference
CAPE - convective available potential energy
CI - convection initiation
CIN - convective inhibition
CM1 - Cloud Model 1
DCC - deep convective core
DJF - December, January, February
DMC - deep moist convection
DNS - discrete-non-supercell
DSC - discrete-supercell
EML - elevated mixed layer
LCL - lifting condensation level
LFC - level of free convection
MCS - mesoscale convective system
ML - mixed layer
MUN - multicell-unorganized
PR - TRMM Precipitation Radar
Q-G - quasi-geostrophic
RH - relative humidity
RMA1 - Córdoba C-band radar
SALLJ - South America low-level jet
SDC - Sierras de Córdoba
SON - September, October, November
SRH - storm-relative helicity
TRMM - Tropical Rainfall Measuring Mission
T - time
w - vertical velocity
WCC - wide convective core
WRF - Weather Research and Forecasting model
UCG - upscale convective growth
UH - updraft helicity
USA - United States of America